2013

Simulation of Melt Penetration and Fluid Flow Behavior during Laser Welding

Bon Seung Koo
Lehigh University

Simulation of Melt Penetration and Fluid Flow Behavior during Laser Welding

By

Bon Seung Koo

Presented to the Graduate and Research Committee

of Lehigh University

in Candidacy for the Degree of

Doctor of Philosophy

in

Mechanical Engineering

Lehigh University

January 2013

Approved and recommended for acceptance as a dissertation in partial fulfillment of the requirements for the degree of Doctor of Philosophy.

_____
Date

_____
Prof. Herman F. Nied:
Committee Chairman and Dissertation Advisor
Department of Mechanical Engineering and Mechanics

_____
Accepted Date

Committee Members

_____
Prof. Sudhakar Neti:
Department of Mechanical Engineering and Mechanics

_____
Prof. Alparslan Oztekin:
Department of Mechanical Engineering and Mechanics

_____
Prof. John N. DuPont:
Department of Material Science and Engineering

Acknowledgments

I would like to express my sincere gratitude to my advisor, Dr. Herman F. Nied for his support and guidance during the course of this research. The progress of this dissertation would not be achieved without his encouragement and patience. I deeply appreciate that he gave me opportunities to work on challenging projects during the period of my studies. I would also like to thank Dr. Oztekin, Dr. Neti, and Dr. DuPont for being on my committee. Their knowledge provided help throughout my studies, and their critical reviews improved the quality of my research with great details. I particularly want to thank Dr. Delph. His knowledge was precious advices in preparing this dissertation. I owe special thanks to Pornsak Thasanaraphan for sharing his experimental studies about the research. His experiences were valuable supports for the verification of my simulation.

I also would like to thank my parents for their help, support, and patience, and their endless love encouraged me to complete this work on time. My special thanks to Ga Young Paik for her patience and understanding throughout the development of this Dissertation. I would not have been able to complete this work without her support. Thanks are also extended to the Department of Mechanical Engineering for offering teaching assistantships and fellowships. I would not have been able to attend the university and continue my education without the financial aids. I would also like to sincerely thank Dr. Macpherson for providing opportunity to have great teaching experiences, and his recommendation and accepting me as a teaching assistant at the Department of Mechanical Engineering continued my study with sufficient financial supports.

Table of Contents

List of Tables		**vi**
List of Figures		**vii**
Abstract		1
Chapter 1	**Introduction**	**3**
1.1	Introduction	3
1.2	Melt penetration mode	5
1.3	Laser welding researches	8
1.4	Current issues and research goals	12
Chapter 2	**Nonlinear material properties**	**14**
2.1	Thermo-physical properties for laser welding study	14
2.2	Density and thermal expansion	17
2.3	Specific heat and enthalpy	23
2.4	Viscosity and shear stress	32
2.5	Conduction, radiation, and thermal conductivity	37
2.6	Coefficient of thermal expansion and ideal gas law	45
2.7	Young's modulus	50
Chapter 3	**Fundamental study on modeling of laser welding**	**53**
3.1	Two dimensional cross-section system modeling	53
3.2	Heat source modeling	57
3.3	Theoretical approach for thermo-fluid analysis	60
3.4	Surface tension and Marangoni convection	64
3.5	Recoil pressure and melt penetration	67

3.6	Welding and dimensionless parameters	71
3.7	Thermal expansion induced Mechanical analysis	74
Chapter 4	**Differential equations used in thermo-fluid analysis**	**77**
4.1	Conservation of thermal energy	77
4.2	Conservation of mass and linear momentum in fluid	79
4.3	Viscous dissipation and viscous work in Newtonian	81
4.4	System governing equations influenced by fluid flow	85
Chapter 5	**Effect of melt dynamics**	**88**
5.1	Laser welding process modeling	88
5.2	Hourglass mode welding	91
5.3	Keyhole mode welding	94
5.4	Evolution of keyhole mode in melt penetration	96
5.5	Effect of surface tension on melt pool formation	99
5.6	Effect of recoil pressure on melt pool formation	102
5.7	Effect of welding parameters on melt size and residual stresses	105
5.8	Dimensionless parameters and width of melt pool	108
5.9	Melt radiation and thermal conductivity	110
5.10	Elevation of residual stresses	114
5.11	Final weld shape	116
Chapter 6	**Conclusion**	**117**
References		**120**
Appendix A		**123**
Vita		**128**

List of Tables

Chapter 2

Table 2.1 Available experimental thermo-physical properties of iron 14

Table 2.2 Modified specific heat of iron versus temperature degrees in Kelvin 30

Table 2.3 Thermo-physical properties used for Nusselt, Reynolds, and Prandtl numbers 43

Chapter 3

Table 3.1 Heat source models – geometrical time dependent heat distribution 59

Table 3.2 Governing equations – conservation of energy balance 63

Table 3.3 Vapor pressure of iron as a function of temperature degrees in Kelvin 68

Table 3.4 Thermo-physical properties of iron used in the Clausius-Clapeyron equation 68

Table 3.5 Welding parameters 72

Chapter 5

Table 5.1 List of simulation set for welding velocity variation at constant heat intensity 105

Table 5.2 List of simulation set for laser intensity variation at constant welding velocity 106

Table 5.3 Welding parameters used in commercial codes ANSYS and SYSWELD 115

List of Figures

Chapter 1

Figure 1.1 Conical Gaussian distribution of heat source 3

Figure 1.2 Schematic presentation of laser welding process 5

Figure 1.3 Estimation of melt front during laser welding 6

Figure 1.4 Schematic diagram of cross-sectional shape of keyhole mode laser welding bead 6

Figure 1.5 Laser butt weld cross sections made in 1.2 mm JAC270F galvanized steel with 0.64 mm JAC270F galvanized steel [4] 7

Figure 1.6 Keyhole formations during the laser welding process with the increment of laser heat intensity 10

Figure 1.7 Gaussian heat distribution of laser beam – surface heat flux 11

Figure 1.8 Gaussian heat distribution of laser beam – volume heat density 11

Chapter 2

Figure 2.1 Ideal heating and cooling (vice versa) curves for pure iron [25] 15

Figure 2.2 Density primary data for liquid iron as a function of temperature [27] 18

Figure 2.3 Variation of density as a function of enthalpy for iron [28] 19

Figure 2.4 Density as a function of temperature and at room temperature 20

Figure 2.5 Density of iron vapor using ideal gas law at constant atmospheric pressure 21

Figure 2.6 Logarithmic density profiles of iron as a function of temperature degrees in Celsius 22

Figure 2.7 Specific heat and enthalpy change of iron 25

Figure 2.8 Specific enthalpy versus temperature for iron [30] 26

Figure 2.9 Variation of enthalpy as a function of temperature for iron [28] 27

Figure 2.10 Specific enthalpy versus temperature of liquid iron [31] 27

Figure 2.11 Enthalpy of iron from the available experimental data 28

Figure 2.12 Enthalpies of iron from Wilthan B. *et al*. and the differential equation (2.11) 28

Figure 2.13 Modified specific heat and enthalpy of iron as a function of temperature degrees in Kelvin 31
Figure 2.14 Density primary data for liquid iron as a function of temperature [27] 34
Figure 2.15 Effect of temperature on viscosity of fluids [34] 35
Figure 2.16 Logarithmic modified viscosities as a function of temperature degree in Celsius 36
Figure 2.17 Influence of temperature and alloying elements on the thermal conductivity of steels [35] 38
Figure 2.18 Thermal conductivity of iron as a function of temperature [37] 38
Figure 2.19 18Cr-8Ni wt% stainless steel (Left) and 1C wt% steel (Right) [38] 39
Figure 2.20 1.5C wt% steel (Left) and 0.5C wt% steel (Right) [38] 39
Figure 2.21 Laser spot welding of 304 stainless steel: laser power of 1300W, pulse duration of 4ms, and spot diameter of 0.42 mm [44] 42
Figure 2.22 Thermal conductivity of iron influenced by radiation above the boiling point 43
Figure 2.23 Modified effective thermal conductivity of iron as a function of temperature degrees in Kelvin 44
Figure 2.24 True coefficient of thermal expansion vs. temperature for iron: The dots are experimentally derived coefficients, and the solid curve is the Grüneisen plot 46
Figure 2.25 Thermal expansion coefficient of iron as a function of temperature [49] 47
Figure 2.26 Coefficient of thermal linear expansion of iron 47
Figure 2.27 Modified coefficient of linear thermal expansion as a function of temperature degrees in Kelvin 49
Figure 2.28 Variation of Young's moduli with temperature [50] 51
Figure 2.29 Modulus of elasticity decreases with increasing temperature 52

Chapter 3

Figure 3.1 Disk laser heat source model on a thin sheet metal structure 53
Figure 3.2 Time dependent laser heat source on a 2D cross section area 54

Figure 3.3 laser welded A131 structural steel: 10 mm thickness, 1.9 kW laser power 54

Figure 3.4 2D symmetric cross-section model for thermo-fluid-structure analysis 55

Figure 3.5 2D cross-section geometries 56

Figure 3.6 2D system boundary conditions 56

Figure 3.7 Gaussian and hypothetical uniform heat density functions with arbitrarily selected $q_0 = 1$ W/mm, $r_0 = 5$ mm, and $v_z = 10$ mm/s: solid line at $t = 0$ sec, dashed line at $t = 0.4$ sec, and dotted line at $t = 0.5$ sec while heat source is moving along the weld line normal to the proposed 2D cross section 59

Figure 3.8 Gaussian and hypothetical uniform heat density functions with arbitrarily selected $q_0 = 1$ W/mm, $r_0 = 5$ mm, and $v_z = 10$ mm/s: solid line at $m = 0.5$, dashed line at $m = 1$, and dotted line at $m = 2$ while varying heat distribution factors 59

Figure 3.9 Boundary conditions for thermo-fluid analysis 63

Figure 3.10 Schematic diagram of temperature dependent surface tension on the melt top layer 65

Figure 3.11 Surface tension of pure iron [56] 66

Figure 3.12 Schematic diagram of recoil pressure effect in deep laser welding 67

Figure 3.13 Vapor pressure of iron from Hultgren R. *et al*. and from the Clausius-Clapeyron Equation 70

Figure 3.14 Predictions of weld pool shapes due to changes in welding parameters 72

Figure 3.15 Boundary constraints for structure analysis 74

Chapter 4

Figure 4.1 Boundary condition of the thermal system 78

Figure 4.2 Control volume in Cartesian coordinates 80

Figure 4.3 Schematic diagram of normal stress components applied to control volume 82

Figure 4.4 Schematic diagram of shear stress components applied to control volume 84

Chapter 5

Figure 5.1 Finite element mesh for 2D cross-section model 89

Figure 5.2 Application of fine meshing around the area where melt penetration was expected 89

Figure 5.3 Moving heat source along the weld line 90

Figure 5.4 Temperature distribution of hourglass: intensity of 3.58×10^{10} W/m^2 and velocity of 100 mm/s 91

Figure 5.5 Velocity profile of hourglass mode with laser intensity of 3.58×10^{10} W/m^2 and welding velocity of 100 mm/s 92

Figure 5.6 Temperature distribution and velocity profile of melt penetration with laser intensity of 3.58×10^{10} W/m^2 and welding velocity of 100 mm/s 93

Figure 5.7 Temperature distribution and velocity profile of melt penetration with laser intensity of 2.387×10^{10} W/m^{2}and welding velocity of 100 mm/s 94

Figure 5.8 Temperature distribution and velocity profile of melt penetration with laser intensity of 5.968×10^{10} W/m^{2}and welding velocity of 100 mm/s 95

Figure 5.9 Initial stage of melt formation measured at different time steps: 0.5, 1, 1.5, and 2 ms 96

Figure 5.11 Effect of recoil pressure during melt penetration at different time steps: 5 and 15 ms 97

Figure 5.12 Effect of surface tension after melt penetration at different time steps: 20, 25, 30, and 35 ms 98

Figure 5.13 Differences in melt pool width due to surface tension with laser intensity of 3.58×10^{10} W/m^2 and welding velocity of 100 mm/s 99

Figure 5.14 Differences in melt pool width due to surface tension with laser intensity of 3.58×10^{10} W/m^2 and welding velocity of 100 mm/s 101

Figure 5.15 Differences in melt pool width due to recoil pressure with laser intensity of 3.58×10^{10} W/m^2 and welding velocity of 100 mm/s 102

Figure 5.16 Differences in melt pool width due to recoil pressure with laser intensity of 3.58×10^{10} W/m^2 and welding velocity of 100 mm/s 104

Figure 5.17 Differences in melt pool width due to recoil pressure with laser intensity of 3.58×10^{10} W/m^2 and welding velocity of 100 mm/s 107

Figure 5.18 Differences in distribution of residual stresses with variable laser intensities at constant welding velocity of 100 mm/s 107

Figure 5.19 Reynolds' number vs. dimensionless width of melt pool with plate thickness of: 1) left: 1.2 mm, and 2) right: 2.0 mm 108

Figure 5.20 Péclet number vs. dimensionless width of melt pool with plate thickness of: 1) left: 1.2 mm, and 2) right: 2.0 mm 108

Figure 5.21 Marangoni number vs. dimensionless width of melt pool with plate thickness of: 1) left: 1.2 mm, and 2) right: 2.0 mm 108

Figure 5.22 Fictitious increments in thermal conductivity as a function of temperature 110

Figure 5.23 Temperature distribution comparisons between two different thermal conductivity sets: measured after melt penetration with intensity of 3.58×10^{10} W/m^2 and velocity of 100 mm/s 111

Figure 5.24 Thermal conductivity of low carbon steel as a function of temperature 113

Figure 5.25 Thermal conductivity of low carbon steel with no modification for radiation internal reflections measured at 30 ms with intensity of 3.58×10^{10} W/m^2 and velocity of 100 mm/s 113

Figure 5.26 Stress elevations in cooling with welding velocity of 100 mm/s and laser intensity of 1.79×10^{10} W/m^2 on 1.2 mm thickness iron 114

Figure 5.27 Stress elevations during solidification with welding velocity of 133mm/s and laser power of 2700 W on 0.64/1.2 mm thickness low carbon steel [4] 114

Figure 5.28 Results of numerical simulation compared with experiments [4] 116

Appendix A

Figure A.1 Effect of heat dissipation on the melt dynamics with laser intensity of 5.968×10^{10} W/m^2 and welding velocity of 100 mm/s 123

Figure A.2 Distribution of residual stresses on a plate thickness of 1.2 mm with laser intensity of 1.79×10^{10} W/m^2 and welding velocity of 100 mm/s 124

Figure A.3 Distribution of residual stresses on a plate thickness of 1.2 mm with laser intensity of 2.38×10^{10} W/m^2 and welding velocity of 100 mm/s 124

Figure A.4 Distribution of residual stresses on a plate thickness of 1.2 mm with laser intensity of 2.98×10^{10} W/m^2 and welding velocity of 100 mm/s 125

Figure A.5 Distribution of residual stresses on a plate thickness of 1.2 mm with laser intensity of 3.58×10^{10} W/m^2 and welding velocity of 100 mm/s 125

Figure A.6 Distribution of residual stresses on a plate thickness of 2.0 mm with laser intensity of 5.96×10^{10} W/m^2 and welding velocity of 100 mm/s 126

Figure A.7 Temperature distribution comparisons between two different thermal conductivity sets: measured during melt penetration with intensity of 3.58×10^{10} W/m^2 and velocity of 100 mm/s 127

Abstract

The purpose of this study is to understand deep penetration laser welding and the effect of laser welding parameters on the hourglass melt pool formation. A transient thermo-fluid-structural laser welding process is numerically computed using finite element techniques, and an evolution of the melt pool is continuously monitored for the measure of the weld shape and size with increasing a time step.

Deep penetration of melt is conducted by the use of high density laser heat energy; rapid evaporation, i.e., prompt phase change from solid to gas, is expected to generate a recoil pressure in the melt pool due to the enormous heat input source. The recoil pressure is considered as an important determinant to form a deep and narrow melt pool. Assuming that atmospheric and vaporized material pressures are balanced at the front of the laser beam, the evaporation of the melt leads to significant pressure work that drills down the melt to the opposite side of a base material when the material is heated over the boiling point.

Besides the recoil pressure, the surface tension of the molten material is also highly responsible for developing and widening the melt pool. The melt surface layer is often influenced by contractive forces of the molten material to minimize its surface free energy [1]. Consequently, minimization of the energy has a substantial effect on the melt surface to stretch out its extent towards the not-yet-melted solid region. As a liquid droplet is often pulled into a spherical shape by the contractive force, the outer layer of the melt pool decreases the melt surface area for physical stability. As a result of minimizing the surface area and the surface free energy, the melt surface tends to have a flat layered shape. A contact angle at the liquid-solid interface therefore is assumed to be negligible in the laser welding study. Marangoni convection, the rate of heat loss from the melt to the ambient air, is induced by the temperature gradient of the melt surface layer;

temperature dependent surface tension is conditionally applied on the layer when temperature rises over the melting point.

In the computation of melt dynamics, energy conservation and momentum equations are used to compute the effects of melt flow and the consequent thermo-fluid heat energy transfer. 2-dimensional governing equations from the Navier-Stokes, i.e., conservation of mass, linear momentum, and energy balance in fluid, are prepared to estimate how melt flow influences the rate of heat transfer and the distribution of temperature in a 2D domain. A mechanical analysis is followed by the thermo-fluid computation using a mechanism relevant to thermal expansion, and the stress distributions are investigated by the use of Von-Mises criterion.

The simulation results are compared with a set of experimental research which laser welds are made of low carbon steel. Assuming that melt flow has dominant influence on the formation of melt pool, a use of a different material and the properties is subject to yield similar results. The shape comparison of the welds describe that parameters relevant to any changes in the melt dynamics are of great importance on the formation of hourglass shaped melt pool during laser welding.

Chapter 1 Introduction

1.1 Introduction

A conical heat source modeling in Figure 1.1 has been used for the prediction of a final weld shape in the finite element based numerical laser welding process [2]. However, the predetermined conical shape is obviously not compatible to explain the laser welding phenomena, e.g., keyhole and full penetration modes. Therefore, the incompletion motivates a study on an appropriate modeling of laser heat source; this will be introduced in this research for better prediction of the final melt pool shape especially for narrow laser welding on a thin sheet of metal.

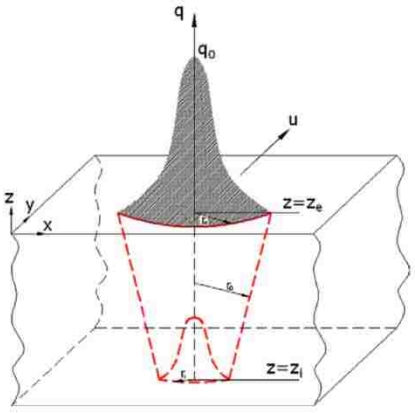

Figure 1.1 Conical Gaussian distribution of heat source [2]

Numerical study is an advanced approach to investigate a laser welding process and considered as an effective method to estimate melt behaviors. Many laser welding studies have introduced two- and three-dimensional numerical techniques in order to determine the shape of melt pool, and the most practical approach was simulation of steady-state liquid metal flow using computational fluid dynamics. Since a theoretical approach of quasi steady-state approximation enabled welding on an infinitely long plate, a 2D cross-section domain perpendicular to the weld

line has high priority to the construction of melt pool. By the assumption of the steady heat flux on the welding axis, the transient laser welding process could be reduced to a 2D heat transfer problem with the cross-sectional weld geometries.

In this study, a finite element based 2D plane is modeled in ANSYS, and material properties of a low alloy steel are chosen for a nonlinear numerical computation. High density laser heat source is assumed to travel along the direction which is normal to a 2D cross-section plane; the maximum laser heat is located at the center of a target surface, and the intensity varies along the radial direction of the laser beam. Assuming that the modifications of the melt properties have no great effect on the melt pool formation, metallurgical complexities, i.e., local microstructure changes due to the existence of alloying components and unpredictable mass fraction in the solid-liquid coexisting zones, is properly removed for full concentration on the study of the melt pool dynamics.

The melt pool formation is assumed to be apparently under the effect of various welding parameters, e.g., welding velocity, laser intensity, temperature dependent material properties, and the final weld shape, but melt surface tension and recoil pressure are considered as primary characteristics to develop the melt pool. A coupled thermal-fluid-structure analysis will be given for a better understanding of how the welding parameters influence the stress elevation during the laser welding process. A result from the 2D thermo-fluid simulation will provide that the change in welding parameters yields various formations of the melt pool. The influence of melt dynamics will be introduced for a deep penetration laser welding process, e.g., keyhole and hourglass modes.

1.2 Melt penetration mode

Laser welding is a fusion joining technique used in modern industrial manufacturing processes. The laser welding process has been involved in many manufacturing applications due to an increasing demand of its use in industries. A remarkable aspect of laser welding is an application of high intensive heat density [W/m^2] which can fabricate a narrow joint weld. In the laser welding process, however, deep penetration modes, e.g., a keyhole and an hour glass, have been found through the change in heat intensity and the welding velocity of a laser beam.

A keyhole mode is a specific type of deep penetration laser welding. The key-hole is one of the deep and narrow shaped melt pools which are often observed when the high intensity laser beam focuses onto a material surface. The laser heat supplies sufficient thermal energy for surface melting while its beam is traveling on the surface of a base metal as shown in Figure 1.2. The formation of the keyhole is because the high thermal energy initiates vaporization of the melt replacing it with the vaporized gas; moreover, excessive laser heat resulting in sudden pressure increase at a liquid-gas or solid-gas interface.

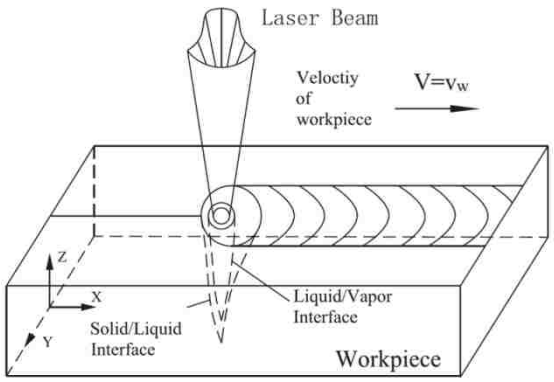

Figure 1.2 Schematic presentation of laser welding process [18]

Vapor pressure at the interface, as shown in Figure 1.3, is assumed to be a critical factor causing the deep melt penetration. An estimation yields the melt initially forms a wide pool at a target surface and a long and narrow area grows along the path of penetration with rapid evaporation of liquid metal as described in Figure 1.4.

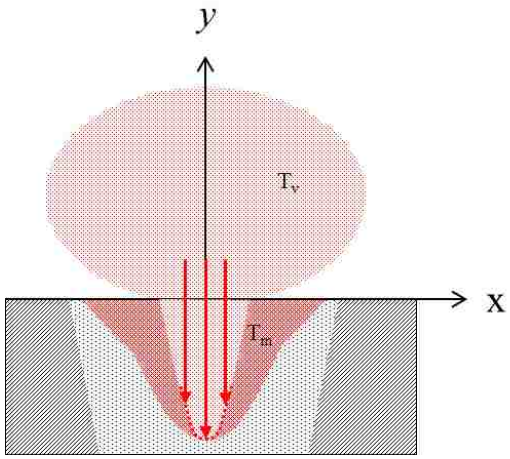

Figure 1.3 Estimation of melt front during laser welding

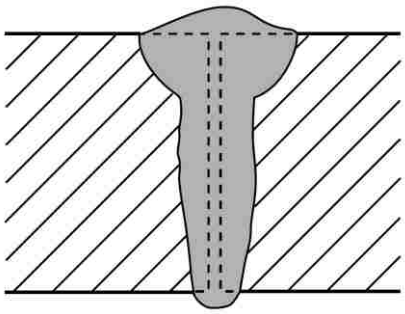

Figure 1.4 Schematic diagram of cross-sectional shape of keyhole mode laser welding bead [3]

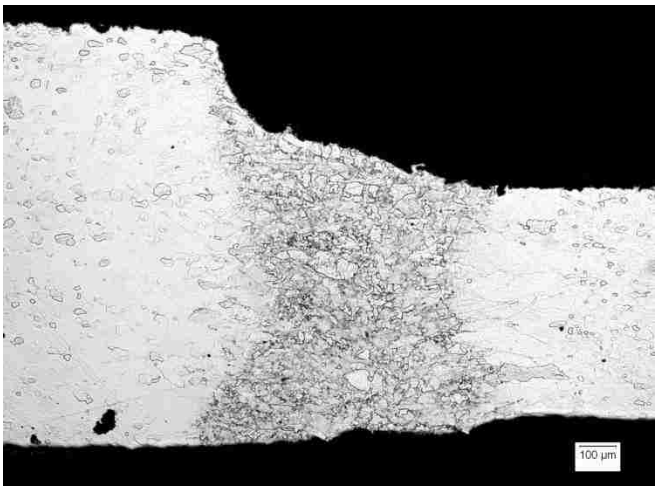

Figure 1.5 Laser butt weld cross sections made in 1.2 mm JAC270F galvanized steel with 0.64 mm JAC270F galvanized steel [4]

On the other hand, an occasional melt expansion has been also investigated when a laser beam penetrates a thin plate. A deep drilling process is the first predictable welding phenomenon because high intensity laser enables full penetration of a base metal by rapid heat transfer which melts the base much faster than energy loss to the neighboring solid region. However, excessive laser heat and rapid energy transfer often make the overall shape of the melt pool influence by surface tension of the melt. Instead of a conical or a key-hole mode, the high intensity laser heat often results in an hourglass shape, i.e., top and bottom wide shaped weld, as shown in Figure 1.5. The hourglass mode is the results only predictable after the melt has full penetration, and the final melt configuration verifies the effect of surface tension which pulls the pool toward a direction heading to a not-yet melted solid area.

1.3 Laser welding researches

Improved welding techniques for innovative laser welding processes are of considerable interest in numerous industrial applications. Interest in laser welding applications has continued to increase and laser welding is now considered to be the preferred joining process in sheet metal manufacturing processes. The advantages of the laser welding process are associated with the generation of a dense high intensity heat source that can provide deep penetration into a desired spot with precise control. The laser welding process seems to be particularly well suited for precision joining of thin and small structures, e.g., micro-electro-mechanical systems [5-9]. The key features of laser welding are that laser welded products exhibit less distortion and higher thermal and electrical conductions [10]. Laser welding moreover provides opportunities for using advanced parametric controls, which are not suitable for other types of welding, to investigate the overall post-weld shapes and welding quality [11, 12].

Improvement of laser welding processes requires a more complete understanding of the laser welding process. Application of a laser heat source, under certain circumstances, can cause an irregular shaped melt pool due to perturbation in the laser heat intensity, variation in the base metal thickness, weld size, and laser moving velocity. Careful observations and experimental measurements have resulted in an improved understanding of melt pool formation [13, 14]. Experimental observations of laser welding have provided useful descriptions of the welding parameters that could cause dramatic physical changes in the melt, e.g., keyhole formation. A molten material formed a cavity as shown in Figure 1.6 and this cavity was called a laser keyhole. A recoil pressure of vaporization and the surface tension gradient from the molten material were assumed to lead to complex liquid circulation in the melt pool. The circulation resulted in a long-narrow region of the melt propagation along the path of concentrated fluid pressure associated with the rapid evaporation of the molten material [10]. The keyhole formation was only one of

the unusual flow related disturbances that could result in deep penetration. The interrelation between surface melting and evolution of melt pool might have substantially influenced the formation of the melt pool. However, the experiment-based evaluations currently provide insufficient insight into the critical welding characteristics that can cause the irregularly long and narrow shaped melt pool formation in the laser welding process.

Finite element techniques for numerical simulation of laser welding have long been employed to study the thermal, fluid, and residual stress effects. Du H. *et al*. conducted a thermo-fluid analysis applying Gaussian heat distribution into their model [15], and Ye X. *et al*. [16] introduced dimensionless numbers, e.g., Marangoni and Péclet numbers, in their study to find the effect of changes in welding parameters on the formation of the melt pool. Cho W. *et al*. studied the effect of melt motion on the melt pool using numerical simulation [17], and Moraitis G. A. *et al*. [18] investigated residual stresses and distortions of laser beam welding for aluminum lab joints. Wang R. *et al*. [19] developed a 3D computational procedure to measure the real-time melt pool shape and to obtain the distribution of temperature in laser keyhole welding.

In general the welding simulation techniques require the user to define the heat source model by inspecting experimental measurements, e.g., the size and shape of the solidified weld. As the limitations of existing theoretical perspectives, a laser welding experiment is required for the predetermination of the heat source model when defining the laser heat source shape for accurate welding simulations.

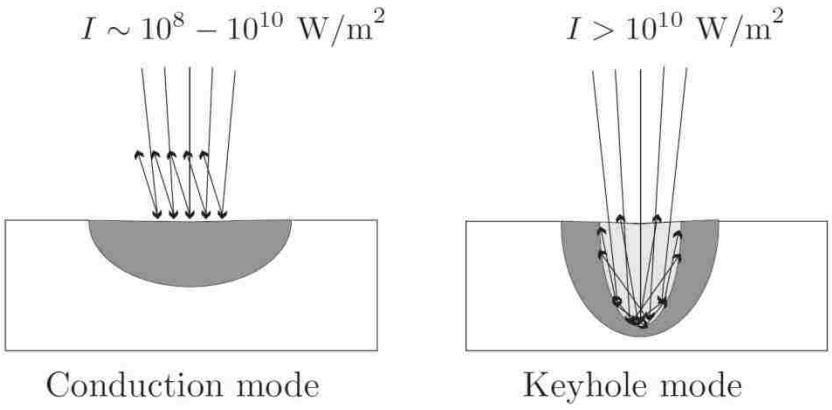

Figure 1.6 Diagram of the laser material interaction phenomena of two typical welding modes [20]

An initial heat source model, e.g., Gaussian heat distribution, has been applied to the F.E. based laser welding simulation by taking measurements of the final weld shape. A schematic description of Gaussian heat distributions is provided in Figures 1.7 and 1.8. Application of a simple Gaussian heat flux onto a thin substrate, as shown in Figure 1.7, was one of the first heat source models for a 2D numerical laser welding process [21]. This heat flux model has been used for sheet metal welding processes since temperature gradient was assumed constant in the direction of thickness. Later, the search for the effect of heat flow through the weld thickness introduced a volumetric cone model with Gaussian heat variation in radial and vertical directions [22, 23]. This volumetric heat distribution is often used for many 3D simulations in deep penetration laser welding. Figure 1.8 shows a heat source model which has been used for 3D deep and shallow conduction mode laser welding. The upper and lower radii and the height of the truncated cone are user-defined geometric parameters. These arbitrary geometric parameters make the cone artificially similar to the actual weld shape since the heat source parameter estimation is mostly dependent on experimental measurements. The conical heat source model is therefore directly obtained from the measurement of the final weld shapes; the *appearance* of *the melt* pool is of importance when simulating the distribution of the welding heat source.

However, there is still a lack of scientific evidence to explain the physical connection between the initial heat source parameters and the final weld shape and size. Moreover, it has not been fully investigated that there were other welding parameters influencing the formation of the final weld shape. As a result, the initial heat source patterned on the final weld is probably limited to apply to certain types of laser welding processes when accurate welding parameters replace the estimation of the weld shape.

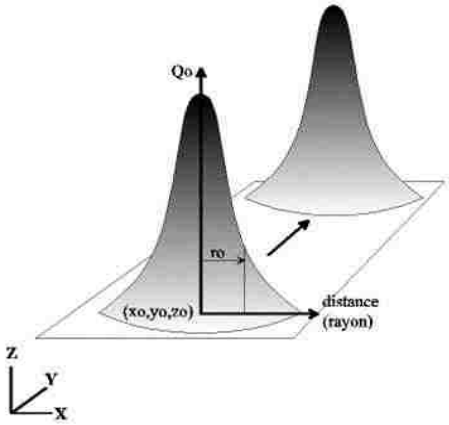

Figure 1.7 Gaussian heat distribution of laser beam – surface heat flux

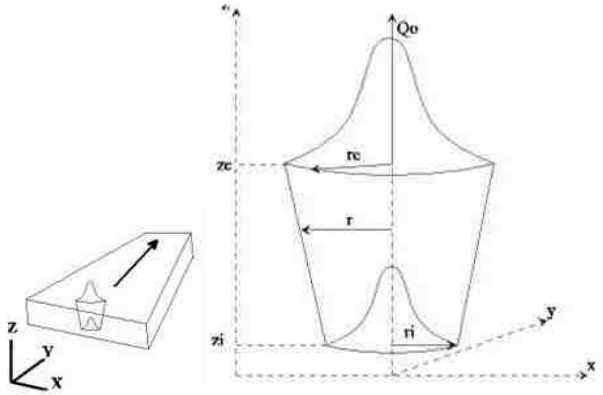

Figure 1.8 Gaussian heat distribution of laser beam – volume heat density

1.4 Current issues and research goals

Unlike heat conduction in solids, heat transfer in welding introduces more complex solid, liquid, and gas heat energy exchanges. The complex welding heat transfer, moreover, needs to incorporate molten material flow for better prediction of the final weld shape and mechanical analysis results [10]. Most numerical laser welding processes have very limited simulation capability based on predetermined geometries and actual welding experiments for the heat source modeling. Improved welding simulation models therefore now include the enhanced heat transfer mechanism associated with fluid motion of the melt for better prediction of melt pool shapes [15-18]. However, these numerical models of laser welding mostly concentrate on the heat and fluid flow mechanisms, and their effects on the formation of the melt pool.

A primary interest in this research is the residual stresses from welding and the resulting thermal strains during heating and cooling cycles. Obviously, the final weld shape can have a large influence on the nature of the weld residual stresses. In a similar manner, the thermal distortion is strongly dependent on the distribution of the residual stresses in the laser heat affected region. The post-weld behaviors and stress states are of great interest in numerical welding simulations since it provides important information for practical engineering situations. However, as indicated by the laser welding literature, thermo-fluid computations are not generally performed in conjunction with solid mechanics calculations. Linking these two very different simulations requires a fully coupled thermo-fluid simulation, integrated with a thermo-mechanical analysis. Once the laser heat source has made its pass and the weld pool begins to cool, the residual stresses begin to evolve from the weld pool geometry and thermal boundary conditions determined by the thermo-fluid simulation. Thus, it is anticipated that a fully coupled thermo-fluid-mechanical simulation will result in predictive capabilities that are mostly dependent on empirical heat source models.

The most significant issues are listed as follows:

- Estimation of the heat source model is an empirical process that is currently dependent on experimental measurements. The initial heat source geometries are frequently determined by the final weld shapes.
- Current laser welding simulation is not at a high enough level for accurate predictions of both melt pool shapes and post-weld residual stresses.
- Most laser welding heat sources are simplistic conical heat density models which are inadequate for modeling certain types of laser welding processes, e.g., keyhole mode laser welding.
- Current welding simulation capabilities are poorly suited for describing correlations between the fundamental welding parameters and the final weld shape.
- Steady state welding simulation is mostly preferred rather than the transient simulation if thermo-fluid analysis is associated with thermo-mechanical analysis due to computational complexities.
- Thermo-fluid analysis has not been followed by structure analysis due to computational complexities.

Chapter 2 Nonlinear material properties

2.1 Thermo-physical properties for laser welding study

In this study, assuming that material properties of a low carbon steel and pure iron were similar one another, they were properly manipulated to determine the critical parameters resulting in the formation of irregular melt pools. The result of irregularity described the non-symmetric shapes of the weld isotherm with respect to the direction of melts penetration. Experimental data for the material properties have been selected referencing several material handbooks and journal articles. Available thermo-physical properties of pure iron were first used to establish standard reference data according to the ambient, melting, and boiling temperatures as given in Table 2.1.

Name	Symbol	Value
Melting point	T_m	1540 ℃
Boiling point	T_v	2860 ℃
Heat of fusion	H_f	13.81 kJ/mol
Heat of vaporization	H_v	340 kJ/mol
Molar mass	M	55.85 g/mol
Specific heat	c_p	449 J/kg ∙K
Density	ρ_s	7874 kg/m^3
	ρ_l	6980 kg/m^3
Thermal conductivity	k_s	80 W/m ∙K
Dynamic viscosity	μ_s	< 10^{12} Pa s
	μ_l	0.006 Pa s
Young's modulus	E	211 GPa
Poisson's ratio	ν	0.29
Thermal expansion	α_L	11.8 μm/m ∙K

Table 2.1 Available experimental thermo-physical properties of pure iron

The subscripts s and l indicate solid and liquid, and the corresponding thermal properties are obtained at room temperature and the melting point respectively. The mechanical properties, e.g., Young's modulus, Poisson's ratio, and the coefficient of thermal expansion, which are usually measured in the vicinity of room temperature, are also assumed to be proportional to the change in temperature.

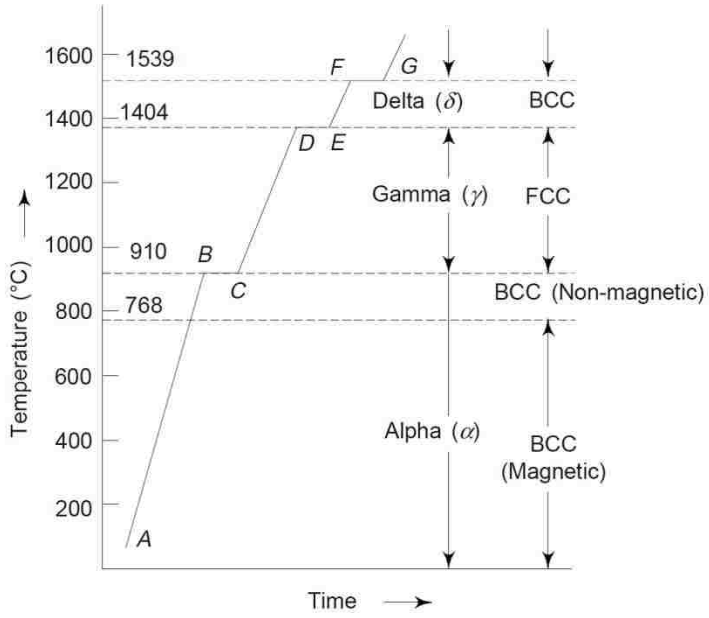

Figure 2.1 Ideal heating and cooling (vice versa) curves for pure iron [25]

In general, pure iron exists in several crystalline forms over a wide range of temperatures. The phenomenon is called "polymorphism" for crystalline materials or "allotropy" especially for metals [24]. Figure 2.1 is the graphical description of phase changes of pure iron during a heating cycle, and the phase transformations can be reversible during the cooling [25]. Assuming that the crystal structures of pure iron can be observed with an increase of temperatures as shown in Figure 2.1 and vice versa on the cooling cycle, the pure iron can form solid-state allotropes, i.e. alpha, gamma, and delta irons. Pure iron forms a body-centered cubic (BCC) structure called α-

iron from room temperature to 910 ℃, and then it has a face-centered cubic (FCC) structure called γ-iron in the temperature ranges of 910 ℃ to 1404 ℃. Above 1404 ℃ the pure iron changes into the BCC structure called δ-iron until the temperature reaches the melting point. The melting point of pure iron is about 1540 ℃, and the pure iron has a liquid phase above the melting. Reading the heating cycle and vice versa, the solid-state phase transitions are noticeable at 910 ℃ and 1404 ℃, and the material properties of the transformed iron can be significantly changed. In this research the allotropic, solid-liquid, and liquid-gas phase changes take place in a relatively wide temperature range with a magnitude of 100 although the real transformations may occur over an infinitesimally small temperature difference. The reason is because of the existence of a high risk which numerical algorithm may jump over the small temperature range and read improper values ignoring the actual physical changes.

Similar to the real characteristics of pure iron, the material properties are highly nonlinear due to the temperature dependent phase transformations during the heating and cooling cycles. The thermo-physical properties of the desired pure iron therefore requires careful selection, and theoretical approaches are conducted along with the data fitting of available experimental measurements for the estimation of the unknown properties. The benefit of the complementary measures is that this welding research can be more reliable to get a particular correlation between melt pool dynamics and welding parameters with a precise control of thermo-physical properties.

2.2 Density and thermal expansion

Density is defined as mass per unit volume. ρ is a symbol for density, and the unit of density is [kg/m^3] in the SI system. Pure metals and their alloys usually have different densities varying with temperatures, thus density in welding is obviously one of the important material properties due to the effect of thermal expansion during the heating and the cooling cycles. The density of metals is usually temperature-dependent in the solid and liquid phases; increasing temperature decreases the density due to the volumetric thermal expansion. Density of solid iron is 7874 kg/m^3 at room temperature. The density decreases gradually with increasing temperature, and iron has the density of 6980 kg/m3 in liquid state near the melting point.

The density of solid iron at room temperature can be easily found in the look-up property tables. But, the profiles with increasing temperatures are neither of great interest nor provided in many material handbooks, thus the fundamental principles of thermal expansion has been used to estimate the densities of solid iron. Law of thermal expansion was the mainly used to determine the density as shown in equation (2.2).

$$\frac{\Delta V}{V} = \frac{V - V_0}{V_o} = \int \alpha_V dT \tag{2.1}$$

$$\frac{1}{\rho} = \frac{1}{\rho_0}\left[1 + \int_{T_0}^{T} \alpha_V \cdot dT\right] \tag{2.2}$$

ρ_0 is a reference density at room temperature T_0. The reference density is easy to obtain using the definition of $\rho_0 = M_w/V_0$ where M_w is the molar weight and V_0 is the molar volume of solid iron at T_0. α_V is a volumetric thermal expansion coefficient. Assuming that a material is isotropic, α_V can be replaced with a linear thermal expansion coefficient α_L through the relation of $\alpha_V = 3\alpha_L$. Conservation of mass is a general principle to make the thermal expansion available for the unknown densities. Using a set of experimental measurements from reference data [26], the density profiles of solid iron is expressed as in equation (2.3).

$$\begin{cases} \frac{1}{\rho} = \frac{1}{\rho_0}\begin{bmatrix} 1 + 3\{0.009 + 1.21 \cdot 10^{-3}(T - 298) \\ +6.504 \cdot 10^{-7}(T - 298)^2 \\ -3.14 \cdot 10^{-10}(T - 298)^3\} \end{bmatrix}, 298 \le T \le 1183K \\ \frac{1}{\rho} = \frac{1}{\rho_0}[1 + 3\{-1.76805 + 0.00233T\}] \quad , 1183 \le T \le 1773K \end{cases} \tag{2.3}$$

Density of solid iron varies with temperature, and density of liquid iron also has a tendency to follow the standard rules. This laser welding study required the density of the material especially in its liquid state; the density over the melting point referred to the recommended values presented by Assaela M. J. *et al.* [27] as shown in Figure 2.2.

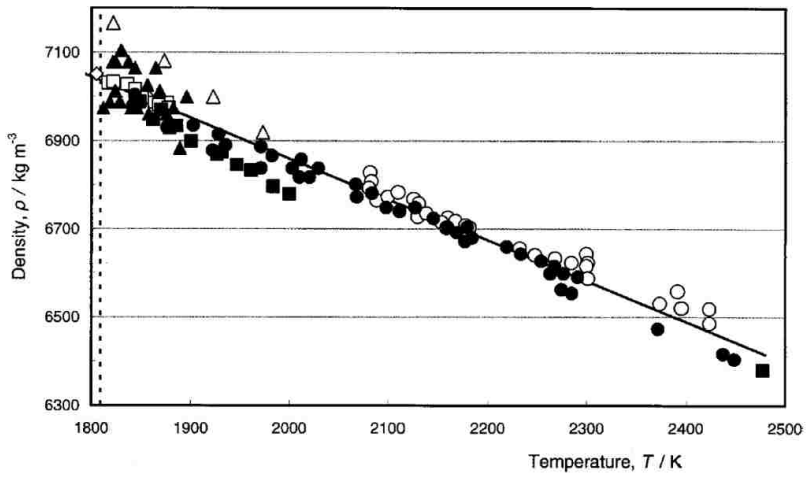

Figure 2.2 Density primary data for liquid iron as a function of temperature [27]

Figure 2.2 represents that the increase in temperature decreases the density. As thermal expansion of liquid iron is known to be a primary factor to increase the volume of liquid iron, the density of liquid iron is gradually reduced over the range of temperatures. The laser welding

process numerically computes the melt behavior using nonlinear material properties; data fitting and an approximate solution for unknown density is highly required up to the boiling point.

Beutl M. *et al.* also investigated several thermo-physical properties of liquid iron. In the research, the density of liquid iron was expressed as a function of enthalpy as shown in Figure 2.3. The least-square fit of density was given in the range of enthalpy from 1.3 to 2.2 MJ/kg, and the enthalpy was obtained at constant pressure over the temperature range of 1808K to 5000K [28]. As a result of the enthalpy changes for the given temperature ranges, the density is expressed as a function of temperature, $\rho = 8312 - 997 \cdot (-0.18626 + 0.00082516 \cdot T)$ kg/m^3.

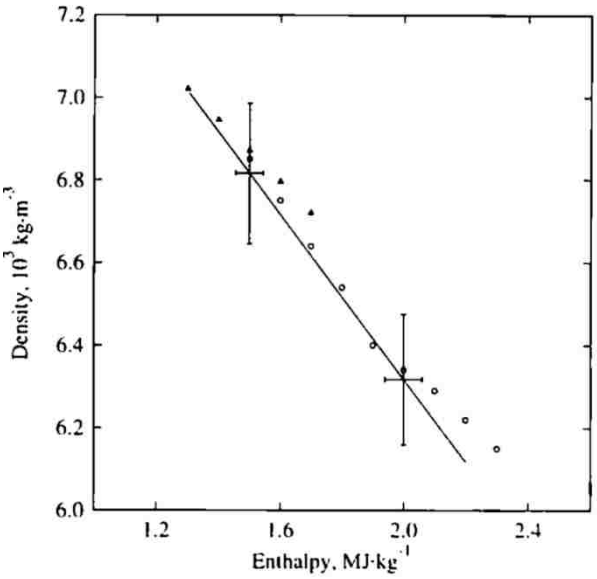

Figure 2.3 Variation of density as a function of enthalpy for iron [28]

A series of iron density over a wide range of temperatures can be properly modified using the recommended references. Plotting the data measured by Buetl *et al.* and Assaela *et al*. with the calculated results from equation (2.2), the density of pure iron shows an overall decreasing tendency from room temperature to a temperature far above the melting point as shown in Figure

2.4. If the density variance is small for solids and liquids and the allotropic phase change at 1183K is negligible, the profile of the liquid density can be extended down to room temperature by an extrapolation method to approximate the density of solid iron.

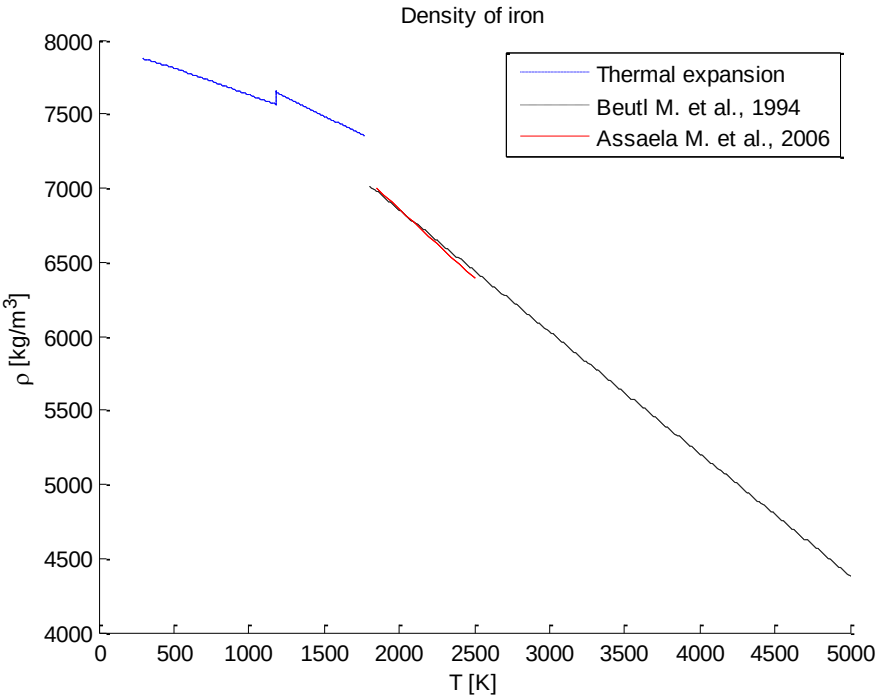

Figure 2.4 Density as a function of temperature and at room temperature

Solids and liquids are all in condensed phases exhibiting an equilibrium vapor pressure equivalent to the ambient air pressure of 101350 Pa. However, gases usually are not in condensed phases and substantially influenced by thermal expansion of gas at high temperatures. Assuming that the atmospheric pressure is remained constant not compressing the evaporated iron, the density of iron vapor can be estimated within the ideal gas law.

$$P_0 V = nR_u T \tag{2.4}$$

$$\rho = \frac{P_0}{R \cdot T} \tag{2.5}$$

P_0 indicates the ambient air pressure. R is the specific gas constant which is the ratio of the universal gas constant to the iron molar mass. The universal gas constant R_u is 8.314462 J/mol K, and the molar mass of iron is 55.845 g/mol. Therefore, the specific gas constant for iron vapor is about 149 J/kg K in the SI unit system. Equation (2.4) is the ideal gas law to obtain volume which varies with the temperature over the boiling point. The density is expressed as a function of temperature as shown in equation (2.5) at constant atmospheric pressure of 101350 Pa.

The density of iron vapor is calculated with the ideal gas law and graphically described in Figure 2.5. Combining the densities of solid and liquid into the gas density profiles, the overall densities are plotted in Figure 2.6 based on the complete range of temperatures from solid to gas. The density profiles were used for the thermo-fluid computation of laser welding.

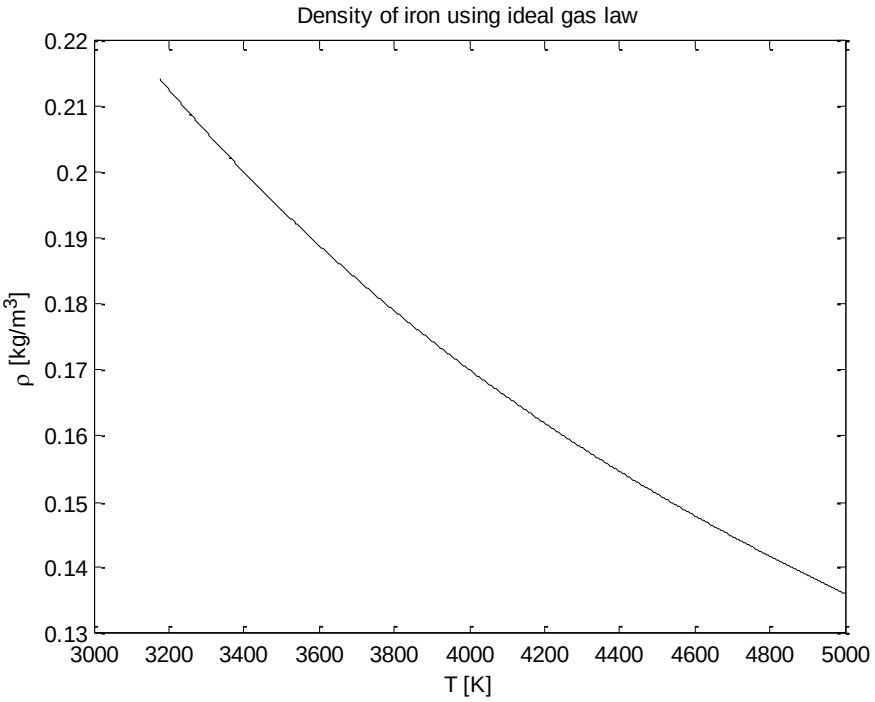

Figure 2.5 Density of iron vapor using ideal gas law at constant atmospheric pressure

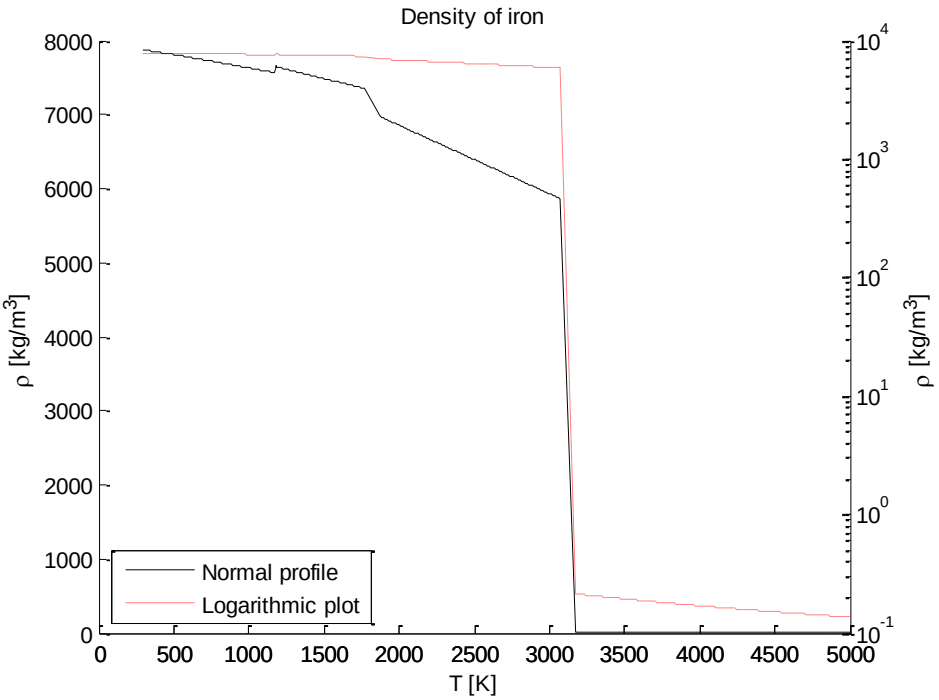

Figure 2.6 Logarithmic density profiles of iron as a function of temperature degrees in Celsius

2.3 Specific heat and enthalpy

Metals and alloys are temperature sensitive materials. Increasing the temperature of a material is responsible for the increase in internal energy and external work done by the heat-induced volume change. Therefore, a physical quantity called heat capacity is useful to measure the effect of the thermal energy accumulation.

$$Q = C\Delta T \tag{2.6}$$

Q is the heat energy added or removed, and C is the heat capacity of a material. In general heat capacity denotes an ability to absorb heat energy for a one-degree change in temperature, and heat capacity is expressed in units of [J/K] in the SI system. The physical quantity is often divided by mass; heat capacity per unit mass is expressed as specific heat capacity.

Specific heat is categorized into two separate terms because the internal energy or the external work is accompanied with the measurement of the heat energy at constant volume or constant pressure respectively. c_p is a symbol for specific heat at constant pressure, and c_v denotes specific heat at constant volume. However, c_v is difficult to use for solid and liquid due to the thermal expansion of a material. The change in internal energy at constant volume needs excessive pressure work to the solid and liquid phases to maintain the shape of a material against the temperature-induced thermal expansion. This will bring more complicated thermo-physical mechanisms into the welding study.

This laser welding research is assumed that the melt pool is subject to stable atmospheric pressure to minimize the environmental effect, thus the specific heat at constant pressure is more adequate not to disobey the rule of thermal expansion. The specific heat of gas is usually measured at constant volume, but c_p can replace c_v using Mayer's relation when c_v is available instead of c_p.

$$C_p = C_v + R_u \tag{2.7}$$

The capitalized $C_p = \left(\frac{dH}{dT}\right)_p$ and $C_v = \left(\frac{dQ}{dT}\right)_v$ are heat capacities which are not yet divided by unit mass, and R_u is the universal gas constant. Equation (2.7) is Mayer's relation derived from the first law of thermodynamics and obeys the ideal gas law.

The relationship between heat and temperature change is usually expressed in the form shown in equation (2.8). The relationship does not follow the basic rule in the range of phase transition because the general tendency of a temperature change is not much involved in a phase transition. Sudden heat addition will be more suitable to explain the energy required for the phase changes, e.g., solid to liquid, solid to gas, and liquid to gas. The sudden increases in energy are defined as heat of fusion H_f and heat of vaporization H_v for the solid to liquid and the liquid to gas phase transitions respectively.

Understanding of the correlation between enthalpy and heat capacity is very useful to obtain specific heat in a wide range of temperatures. In equation (2.9) H is a symbol for enthalpy, and the unit of enthalpy is [J] in the SI system. Enthalpy is a measure of the internal energy including the external work done by the thermal expansion at constant pressure. However, there is no direct method to measure enthalpy because H is a state function indicating a thermodynamic potential, e.g., chemical and physical reactions. Measuring ΔH which is the change in enthalpy is therefore more practical to obtain the quantity in the energy level.

$$\Delta Q = c_p m \Delta T \tag{2.8}$$

$$H = E + PV \tag{2.9}$$

$$\Delta H = C_p \Delta T \tag{2.10}$$

$$c_p = \left(\frac{dh}{dT}\right)_p \tag{2.11}$$

Equation (2.10) is the mathematical expression of heat capacity when the enthalpy change is given as a function of temperature. As the word "specific" means a physical quantity divided by its unit mass, the change in enthalpy will follow the same "per mass" expression as shown in equation (2.11).

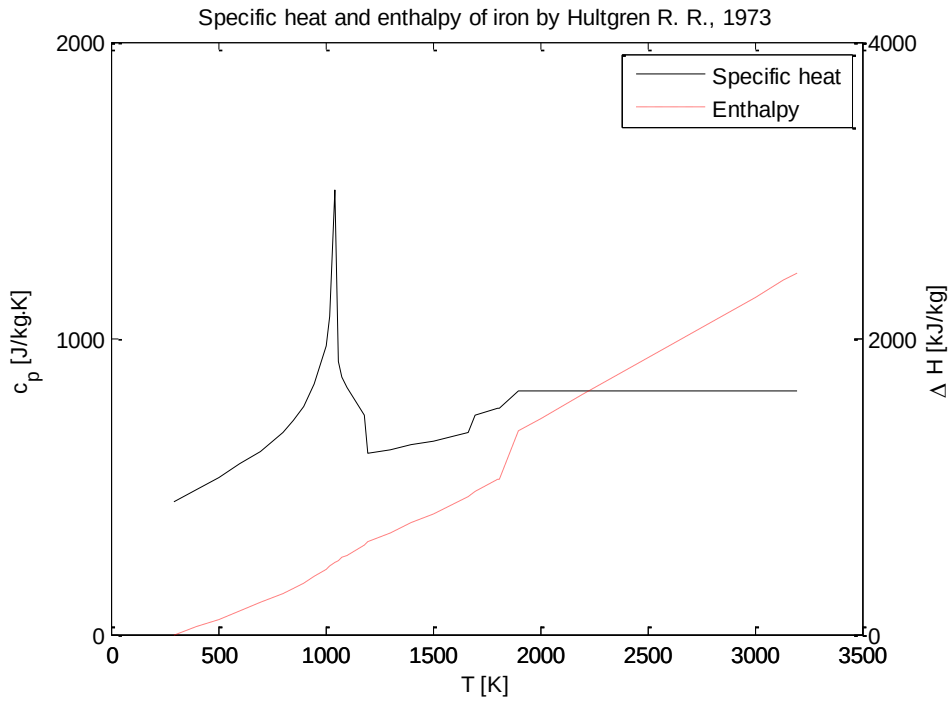

Figure 2.7 Specific heat and enthalpy change of iron

Using equation (2.11) is more suitable for this welding research although there are some available experimental data. The reason is to remove abrupt property changes during an evolution of microstructure which has different crystal structures over a certain range of temperatures. Solid iron can exist in three different forms, e.g., α-ferrite, γ-ferrite, and δ-ferrite, while temperature falls down to room temperature in solidification. The change in specific heat is apparent when iron has phase changes in the solid state. Figure 2.7 indicates a sudden change in the profile slope

at 1042K which is corresponding to the solid-state structure change [29]. In general the property change with a steep profile slope is less predictable, highly nonlinear, only observed during experiments, and susceptible to increase computational errors. In order to avoid the problems, equation (2.11) is mostly used to obtain the specific heat of pure iron.

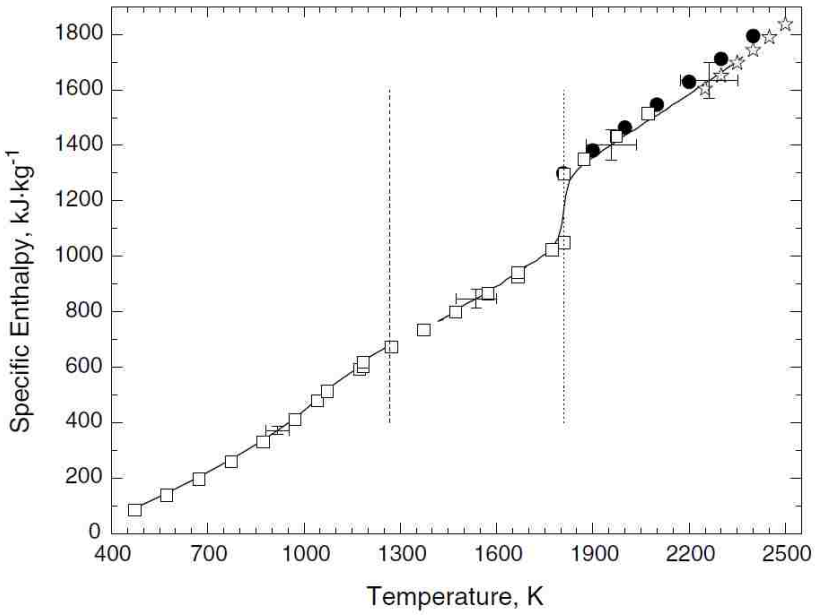

Figure 2.8 Specific enthalpy versus temperature for iron [30]

Wilthan B. *et al*. measured the specific enthalpy of iron over the temperature range of 473K to 2370K [30]. The melting point of 1808K was used for the solid to liquid phase separation, and the enthalpy was measured continuously in several discrete temperature ranges. The results are graphically displayed in Figure 2.8.

Beutl M. *et al*. and Hixson R. S. *et al*. also studied the change in enthalpy as a function of temperature as shown in Figures 2.9 and 2.10. Beutl M. *et al*. measured the enthalpy of iron over the wide temperature range of 1808K to 5000K [28], and Hixson R. S. *et al*. obtained the linear

least squares fitting of the enthalpy in the range of 2125K to 3950K with the constant c_p of 815.4 J/kg K [31].

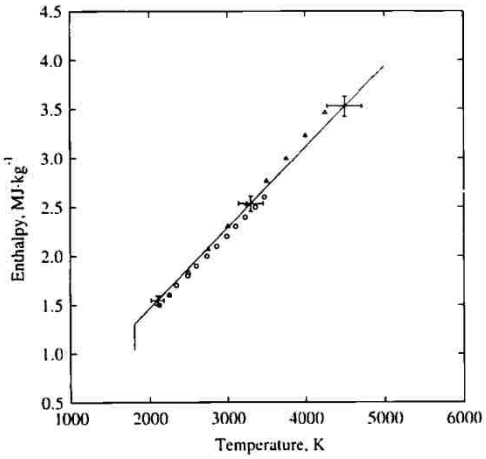

Figure 2.9 Variation of enthalpy as a function of temperature for iron [28]

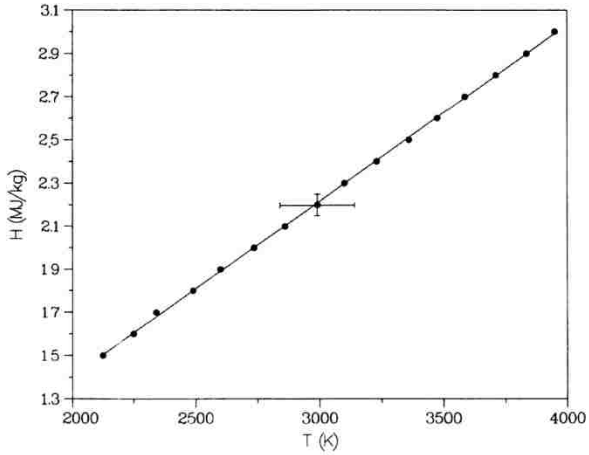

Figure 2.10 Specific enthalpy versus temperature of liquid iron [31]

Using the available experimental data measured at constant pressure, the enthalpy of iron can be properly approximated for the complete range from solid to gas. In the multiple plots of Figure 2.11 each line is very similar to one another; the most recent experimental research from Wilthan B. *et al*. has been chosen as reference data to be compared with the modified enthalpy adequate to this numerical laser welding simulation.

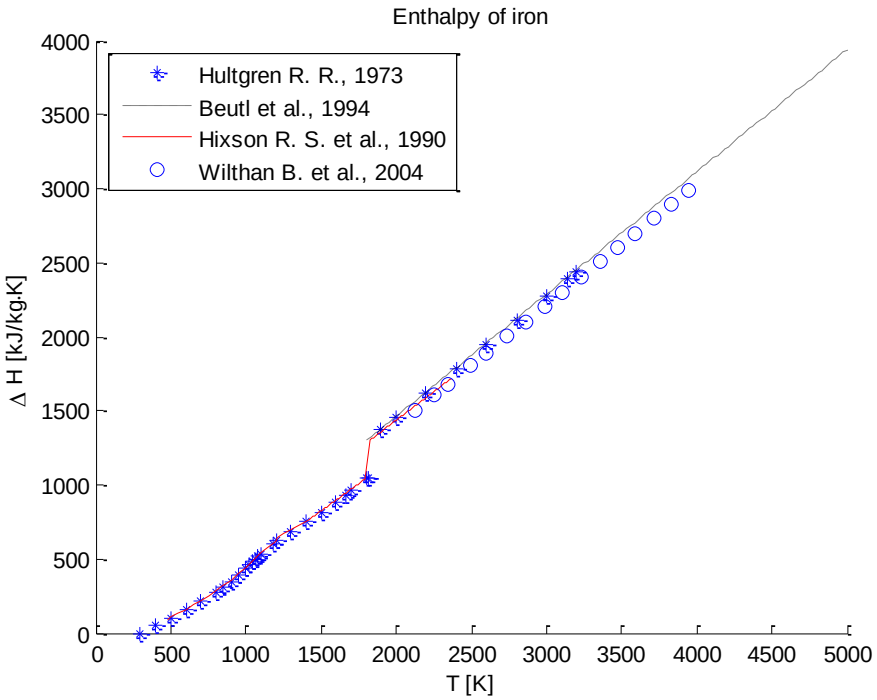

Figure 2.11 Enthalpy of iron from the available experimental data

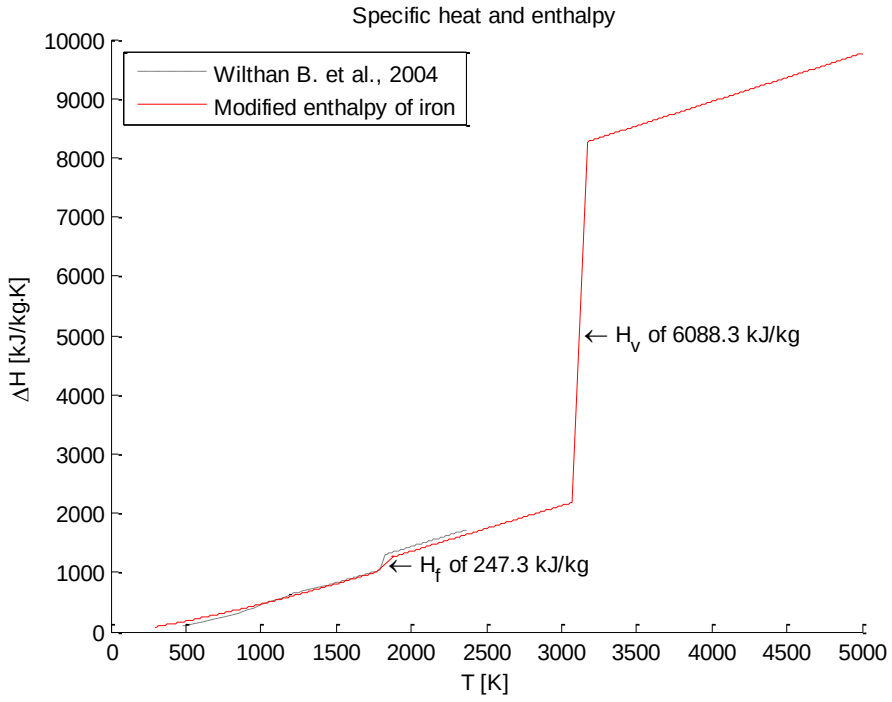

Figure 2.12 Enthalpy of iron from Wilthan B. *et al.* and from the differential equation (2.11)

The enthalpy was modified over the temperature range of room temperature 298K to a high enough temperature 5000K. As in Figure 2.11 the specific heat was not consistent at 1184K, and it was assumed to be due to the effect of solid-state phase change. The enthalpy of solid is often modeled to have a gradual temperature increase because of the relation between heat addition and thermal expansion; therefore, specific heat is assumed to be responsible for the rate of the volume change.

As a result of that, the first requirement was to reduce the inconsistent metallurgical effect adjusting the specific heats to the thermal expansion of solid. A central difference approximation was applied into equation (2.11) to obtain a numerical solution of specific heat. Integrating equation (2.11) resulted in a set of enthalpies which could be compared with the referenced experimental data as shown in Figure 2.12. The modified enthalpy in Figure 2.12 agreed well with the referenced data when the temperature changes in the range below the melting point. Although most available references did not take the latent heat of the vaporization into consideration, the modified enthalpy did have the certain change in enthalpy according to H_v at 3133K

The modified enthalpy profiles are presented in equations (2.12) and (2.13) for the solid, liquid, and gas phases of iron. Using the available experimental data, the specific heat of solid iron is expressed as the third-order polynomial in the temperature range from 298K to 1773K. The specific heat of liquid and gas is also expressed as a function of temperature as in equation (2.13).

The specific heat of iron has not been fully investigated in the gas phase, thus it was assumed it would be similar to that of liquid iron. Analyzing the experimental studies, the specific heat of liquid iron remained constant with a value of 770 J/kg ⁄K (based on the temperature range of 1830K to 2370K by Wilthan B. *et al*.), and that of iron gas had a constant value of 815.4

J/kg K (related to the temperature range of 2125K to 3950K by Hixson R. S. *et al*.). There was a high risk that numerical computation jumps over the small temperature range; therefore, heat of fusion and heat of vaporization were assumed to take place in a wide range of temperatures as shown in equations (2.12) and (2.13) to avoid the misinterpretations.

$$H(T) = -5.885 \cdot 10^{-8}T^3 + 3.368 \cdot 10^{-4}T^2 + 0.354T - 39.686, \qquad (2.12)$$

$$298\text{K} < T < 1773K$$

$$H(T) = \begin{cases} 0.770T - 187.177, & 1873K < T < 3073K \\ 0.770T + 5.824 \cdot 10^3, & 3173K < T < 5000K \end{cases} \qquad (2.13)$$

T [K]	c_p [J/kg K]
298	449
373	471
473	500
1003	632
1183	670
1423	714
1673	753
1773	2456
1813	2456
1873	2456
1923	770
2973	770
3073	60288
3133	60288
3173	60288
3273	815.4
5000	815.4

Table 2.2 Modified specific heat of iron versus temperature degrees in Kelvin

Finally the modified specific heat of pure iron is provided in Table 2.2 for numerical computation, and its profile is graphically displayed in Figure 2.13. The mathematical expression of Figure 2.13 results in Equation (2.14) which is corresponding to the entire temperature range from room temperature to 5000K.

$$\Delta H = \int_{T_0}^{T_m} c_{p,s}(T)dT + H_f + \int_{T_m}^{T_v} c_{p,l}(T)dT + H_v + \int_{T_v}^{T_\infty} c_{p,g}(T)dT \qquad (2.14)$$

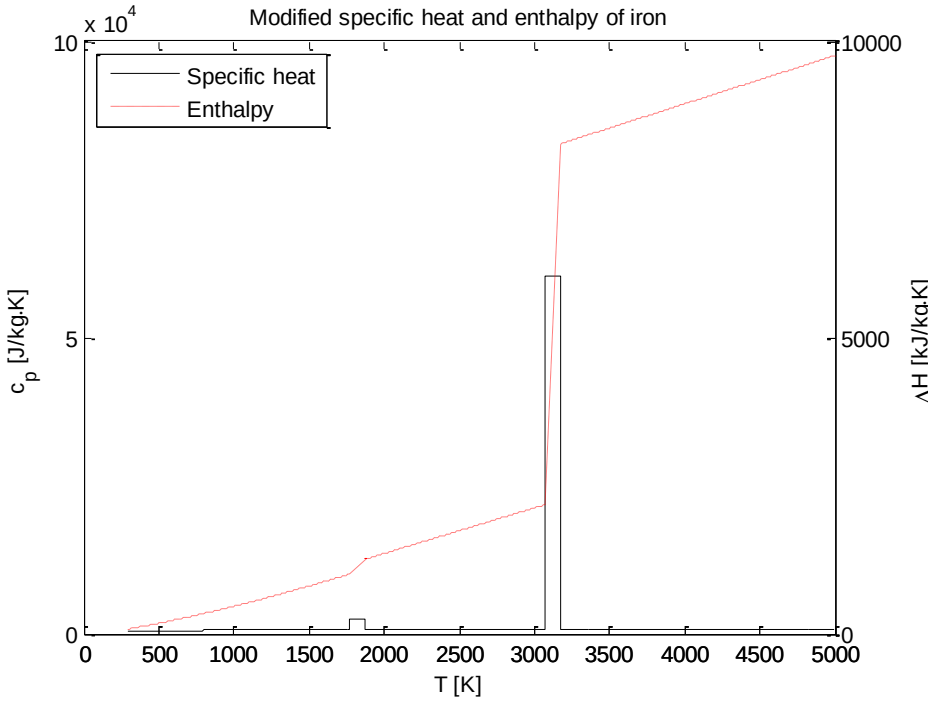

Figure 2.13 Modified specific heat and enthalpy of iron as a function of temperature degrees in Kelvin

2.4 Viscosity and shear stress

Viscosity is a measure of the frictional fluid property, and stands for the resistance to the flow of a molten material in the welding process. Viscosity can be an important physical property for the analysis of fluid circulation adjacent to not-yet-melted solid boundaries and in the melt pool. A melt flow resistance is caused by intermolecular friction when melts attempt to slide by one another. Dynamic and kinematic viscosities, two different measures of the fluid friction, are introduced to explain the viscous melt flow behavior.

Dynamic viscosity is known as absolute viscosity or the coefficient of absolute viscosity. A relationship between dynamic viscosity and the shear stress is expressed in equation (2.15). A non-turbulent fluid is often defined as a Newtonian fluid, and the velocity gradient $\frac{\partial u}{\partial y}$ is a coefficient of shear stress in the Newtonian fluid. As Newtonian fluid dynamics is applicable to most common fluids, e.g., liquids and gases, pure iron at high temperatures was assumed to be the Newtonian fluid in this laser welding study.

$$\tau = \mu \frac{\partial u}{\partial y} \tag{2.15}$$

τ is shear stress, and μ is dynamic viscosity. Equation (2.15) is known as Newton's Law of Friction. In the SI system the unit of dynamic viscosity is [Pa s], [N s/m^2], or [kg/m s]; however, metric CGS (centimeter-gram-second) system of [g/cm s], [P], or [cP] is often used for dynamic viscosity due to extremely low magnitude of it in liquid state. Although several units of viscosity are available, [Pa s] will be mostly used to be consistent with other thermo-physical properties in the standard MKS system.

Kinematic viscosity is the ratio of dynamic viscosity to density, and kinematic viscosity is simply obtained by dividing the dynamic viscosity of the fluid density as in equation (2.16).

$$\nu = \frac{\mu}{\rho} \tag{2.16}$$

ν is kinematic viscosity, and ρ is density. The unit of kinematic viscosity is [m^2/s] and in the SI system. However, this welding study will use dynamic viscosity to reduce the risk of computational divergence because the kinematic viscosity includes two temperature-dependent variables, dynamic viscosity and density, which are highly nonlinear over a wide temperature range.

The term "viscosity" is originally devised for fluidity, thus experimental data for solid viscosity is very limited and almost not obtainable compared to the resources available for liquids. The difficulty in viscosity measurement requires rough estimation; therefore, viscosity of a solid can be approximated to have extremely high magnitude different from that of a liquid or gas. Assuming that liquid cooling and solid melting transitions are processed in a long period of time, viscosity of a solid can be in the range of 10^{13} to 10^{15} cP (equivalent to the magnitude of 10^{10} to 10^{12} in Pa s) [32]. If the assumption is extended down to the ambient temperature level, the hypothetical solid-liquid transition will possibly result in the value of 10^{12} Pa s for the viscosity of solid iron at room temperature.

Liquid is the most adequate phase to apply viscosity out of all the different material phases. Liquid viscosity is known to be highly temperature dependent but pressure independent if liquid is not exposed to extremely high pressure. Since the Newtonian fluids are incompressible, an increase in pressure does not have a great effect on molecular expansion or contraction. In contrast to the pressure, a liquid molecule obtains more energy that motivates the fluid free to move when thermal energy is transferred into the molecular level of a fluid. While the magnitude of molecular vibration or translation is increased due to heat addition, the molecular bonds are weakened and finally cause less friction to the neighboring molecules. That is why liquid viscosity generally decreases with increasing temperature. The measurements of liquid viscosity therefore rely on a number of experimental research activities while heating up the fluid.

The viscosity of liquid iron can be determined through experimental results achieved over the melting point. Assaela M. J. *et al.* conducted research on the dynamic viscosity of liquid iron, and the results are plotted in Figure 2.14. The recommended viscosities for iron are limited in the temperature range of 1850K to 2500K; the dynamic viscosity of liquid iron has a tendency to decrease gradually from 0.00544 to 0.00228 Pa s when temperature increases [27].

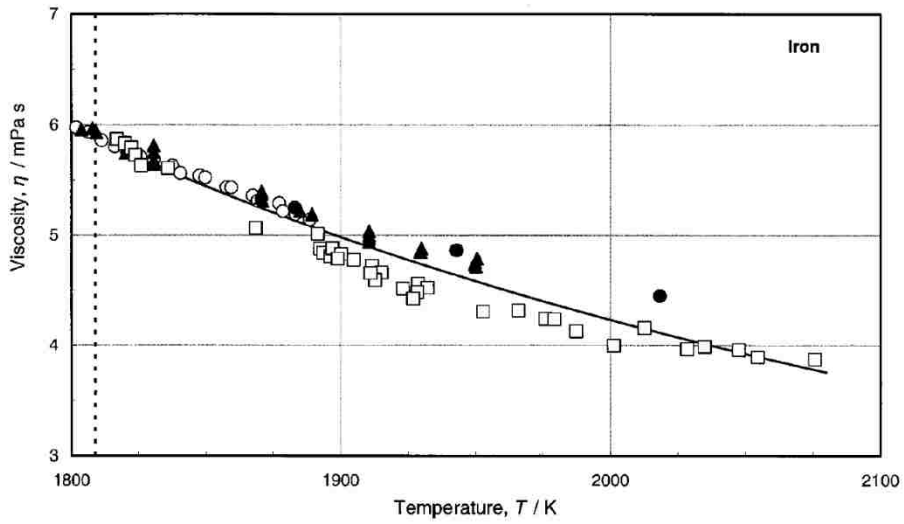

Figure 2.14 Density primary data for liquid iron as a function of temperature [27]

Another reference written by Baukal C. E. *et al*. provides the correlation between the temperature and the dynamic viscosity of iron in the form of the following equation: $\mu = 1.573 \cdot 10^{-8}T^2 - 6.739 \cdot 10^{-5}T + 0.07741$ [Pa · s] with the unit of temperature in Kelvin [33]. The equation is valid for the temperature range of 1850K to 2150K, the viscosity varies from 0.00657 to 0.00523 Pa s when temperature increase.

For gas, it is obvious that kinematic viscosity is substantially elevated with increasing temperature because density of ideal gas approaches close to zero by the ideal gas law. In contrast, dynamic viscosity decreases markedly over the vaporization point due to no fluid friction in the gas phase; however, there is no clear way to quantitatively determine the dynamic viscosity of gas. As a result, appropriate estimates were preceded for the dynamic viscosity of iron vapor at high temperatures.

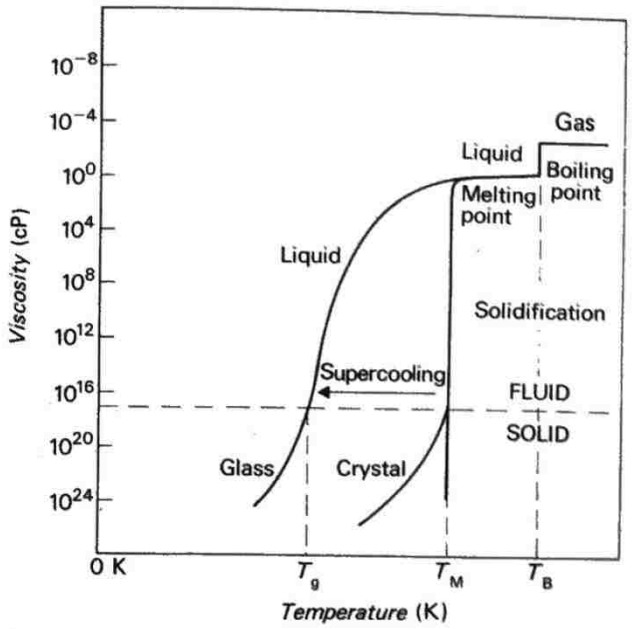

Figure 2.15 Effect of temperature on viscosity of fluids [34]

Figure 2.15 shows the hypothetical approaches to estimate viscosity of gas. The graphs are mostly based on the phase changes of water, thus there will be a slight or huge deviation when the profile is used for pure iron. A reference edited by Tottle C. R. approximates the average dynamic viscosity of gas to 10^{-2} cP [34]. The dynamic viscosity of a liquid is 1 cP at around the melting point, and that of a liquid condensed from a gas decreases 1 to 2 orders of magnitude and consequently results in a value of 10^{-2} to 10^{-1} cP at around boiling point.

Since the dynamic viscosity of pure iron is not fully investigated, proper estimates must supplement the limited measurements to provide a reasonable set of viscosities. As described, the only availability from the experimental researches was the linear decrease of the dynamic viscosity profiles over the temperature range of 1850K to 2150K; the corresponding viscosities were from 0.006 to 0.004 Pa s. Using the available literatures, approximations resulted in two dynamic viscosities: 10^{12} Pa s [32] for the solid at room temperature, and $< 10^{-4}$ Pa s (2 to 3 orders of magnitude lower than the liquids) for iron vapor above the boiling point. Assuming that the change in dynamic viscosity could be developed in the similar decreasing manner of the profiles in Figure 2.15 but more stable within the same phase, the viscosity was modified as given in Figure 2.16.

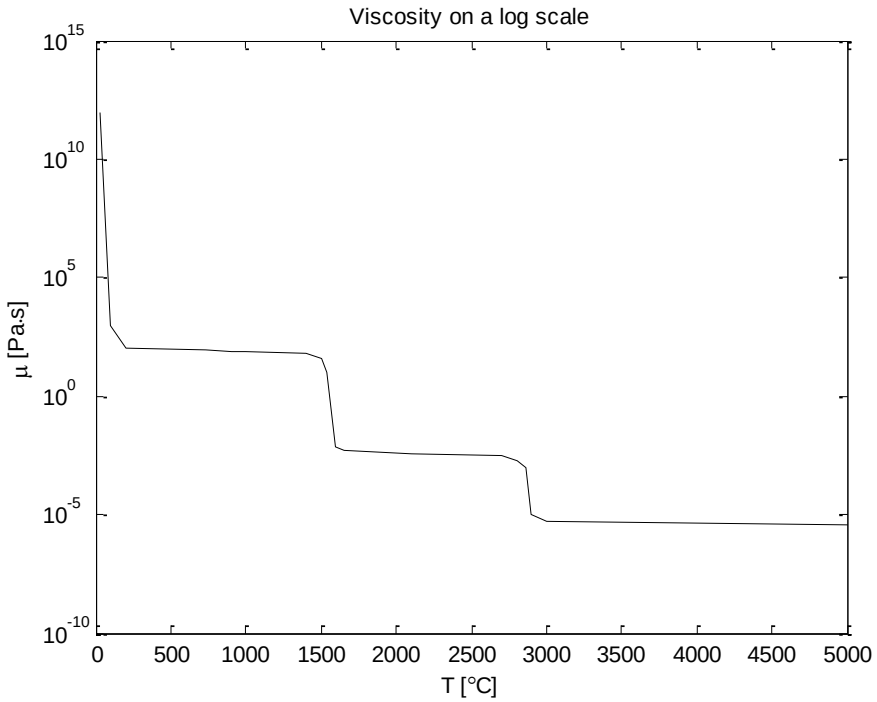

Figure 2.16 Logarithmic modified viscosities as a function of temperature degree in Celsius

2.5 Conduction, radiation, and thermal conductivity

Conduction is the most fundamental method of transferring thermal energy by the direct contact of materials. The definition of thermal conductivity is an ability to conduct thermal energy from one to another material. Thermal conductivity is therefore relevant to the rate of heat conduction through a material in welding. The law of heat conduction, known as Fourier's law, derives the mathematical expression of equation (2.17) when materials are in thermal contact.

$$\frac{\vec{Q}}{A} = \vec{q} = -k\nabla T \qquad (2.17)$$

k is a symbol for thermal conductivity, and the unit is [W/m K] in the SI system. $\vec{q}$ [W/m^2] is heat flux which is the ratio of thermal energy $\vec{Q}$ [W] to an area A [m^2]. The area is usually normal to the direction of heat flow, and a temperature gradient ∇T induces heat conduction in a material. The "negative sine" in equation (2.19) denotes that the direction of heat flow is opposite to the temperature gradient because heat always transfers from the higher energy level to the lower energy level.

Heat conduction rate usually varies by the weight percentage of alloying components with increasing temperature, thus thermal conductivity is a highly chemical composition and temperature dependent property. The conductivities of alloy steels in Figure 2.17 have a tendency to converge into a certain value over the range of temperatures; however, pure iron tends to have an inflection point at around 1200K. This is assumed to be because of the effect of the solid-state phase transition; the structural transformation may induce the significant change in thermal conductivity due to the relocation of internal molecular structure [35].

It is common that the high alloy steel, e.g., high carbon and stainless steels, have lower thermal conduction rates compared to pure iron. The thermal conductivity rapidly decreases with increasing carbon contents because addition of carbon causes brittleness, less thermal expansion and lower heat conduction [36]. Figure 2.18 by Powell R. W. *et al.* [37] shows the change in

thermal conductivity of pure iron with increasing temperature, and Figures 2.19 and 2.20 investigated by Peet, M. J *et al*. [38] are the plots of thermal conductivities of the iron alloys.

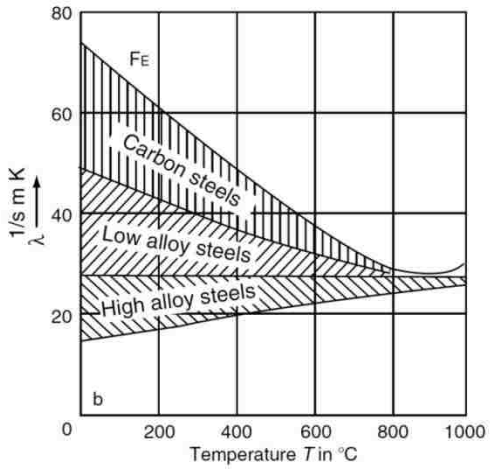

Figure 2.17 Influence of temperature and alloying elements on the thermal conductivity of steels [35]

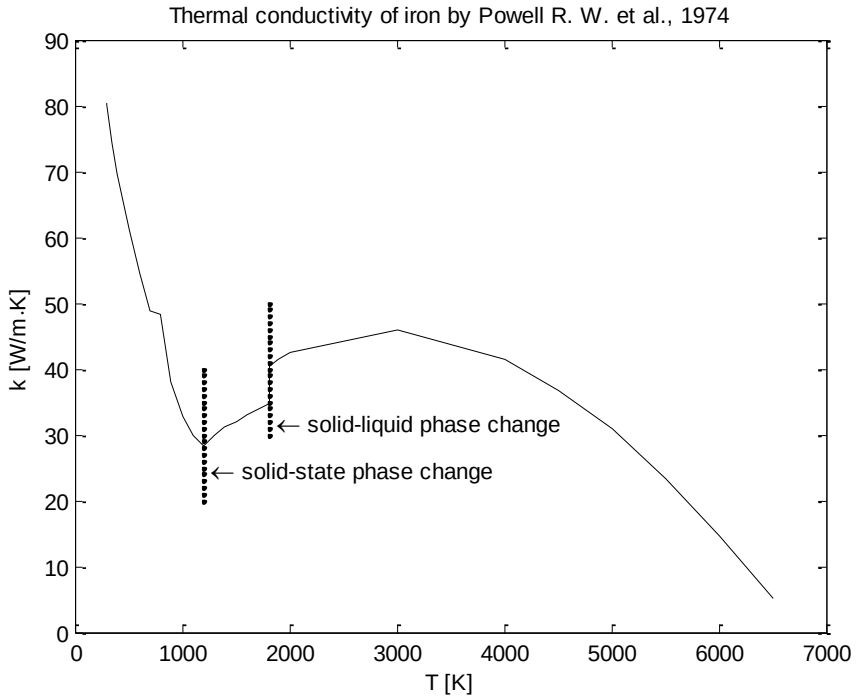

Figure 2.18 Thermal conductivity of iron as a function of temperature [37]

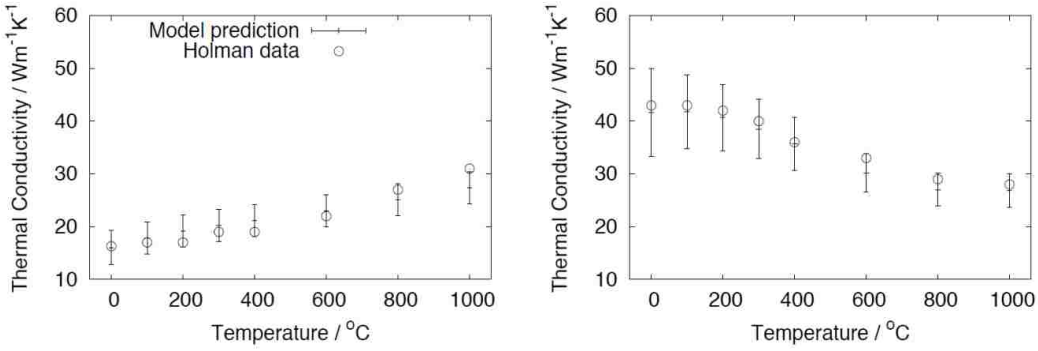

Figure 2.19 18Cr-8Ni wt% stainless steel (Left) and 1C wt% steel (Right) [38]

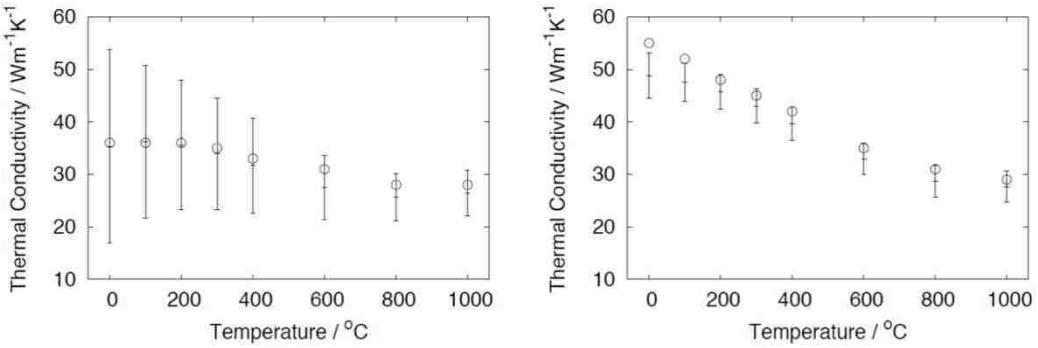

Figure 2.20 1.5C wt% steel (Left) and 0.5C wt% steel (Right) [38]

Thermal conductivity is a primary interest because the analysis of the numerical welding research is mostly dependent on the distribution of temperature. The thermal conductivity of pure iron is well measurable in the solid and liquid phases, but the gas phase thermal conductivity requires proper approximations and estimations. Referring to Figure 2.18, the thermal conductivity of pure iron is about 80 W/m Ŧ at room temperature, and it decreases gradually with increasing temperature up to the solid-state phase transition point of 1200K. The thermal conductivity has a certain increase of 35 to 41 W/m Ŧ near the melting point, and the profile curvature increases gradually in the liquid phase until it reaches near the boiling point of 3000K. Within the melting temperature ranges, a certain increase in thermal conduction is because of the

solid to liquid phase change. A decreasing trend over the boiling is assumed to be associated with continuously reduced iron's contribution to heat conduction while it evaporates out.

This numerical study requires a modification on the thermal conductivity of iron gas. The possibility of keyhole mode observation can be raised by the use of the high density laser heat which causes rapid thermal energy transfer from the heat source to a neighboring material. The intensity for deep penetration laser welding is approximately 10^{10} W/m^2 [19], and the amount of radiation being emitted is much greater than the rate of heat conduction through the medium in the keyhole. The radiation is usually applied as the boundary condition in the numerical welding studies [39-42], thus the real-time diagnostics of melt radiation is difficult to implement unless the thermal boundary is continuously updated.

It is not an effective way to use either the experimental measurement of thermal conductivity or the application of moving thermal boundaries. If the measured thermal conductivity is used without a proper modification, the rate of heat conduction is not high enough to replace the radiation heat exchange in the melt pool. Moreover, the moving boundary causes enormous computational load in this coupled analysis due to the fact that boundary tracking takes place every single time step to update the geometrical change of the melt pool. Therefore, the relation between the coefficients of radiation and heat conduction had to be established for the better estimation of melt pool heat transfer.

Assuming that the radiation heat exchange has a great effect on gas to liquid heat transfer, the reference surface temperature T_s is the boiling point of pure iron. Equation (2.18) is the radiation heat transfer to obtain a mathematical expression of a radiation heat coefficient, $h_r = \varepsilon\sigma(T^2 + T_s^2)(T + T_s)$. Using Newton's Law of Cooling, an overall heat transfer coefficient is the sum of convection and radiation heat transfer coefficients, $\bar{h} = h + h_r$ because the melt flow is also correlated with convectional heat exchange in the melt pool. The effect of radiation

is ,however, much greater than the heat convection due to the extremely high melt temperatures, thus the overall heat transfer results in equation (2.19) with the relation of $\bar{h} \approx h_r$.

$$q = \varepsilon\sigma(T^4 - T_s^4) = \varepsilon\sigma(T^2 + T_s^2)(T + T_s)(T - T_s) = h_r(T - T_s) \quad (2.18)$$

$$q = \bar{h}\,(T - T_s) \quad (2.19)$$

A dimensionless parameter, Nusselt number, can be introduced for a measure of the heat convection when it occurs through a liquid-gas thermal boundary in the melt pool. The Nusselt number is given as a function of dimensionless parameters, Reynolds' number Re and Prandtl number Pr. The definition of Nusselt number is the ratio of convective to conductive heat transfer across the thermal boundary, the average heat transfer coefficient can be calculated using the knowledge of Nusselt number, $Nu = \frac{\bar{h}D}{k} = f(Re, Pr)$.

The overall heat transfer coefficient is of interest for better prediction of heat transfer rate through the liquid-gas boundary. Assuming the downward melt flow generated by the high laser intensity is similar to the velocity profile of an impinging jet convection mode, equation (2.10) recommended by Martin can be first used to find Nusselt number [43]. The Nusselt number is expressed as $f(G, Re, Pr)$ and the expression of G and the Reynolds' number are given in equations (2.21) and (2.22). Prandtl number is a dimensionless parameter and dependent on the fluid status by the definition of $Pr = \frac{\nu}{\alpha} = \frac{\mu c_p}{k}$.

$$\frac{Nu}{Pr^{0.42}} = G\left(Ar, \frac{H}{D}\right) \cdot 2Re^{0.5} \cdot (1 + 0.005Re^{0.55})^{0.5} \quad (2.20)$$

$$G = 2A_r^{0.5} \cdot \frac{1 - 2.2A_r^{0.5}}{1 + 0.2\left(\frac{H}{D} - 6\right)A_r^{0.5}} \quad (2.21)$$

$$Re = \frac{\rho V_s D}{\mu} \quad (2.22)$$

$$k_r = \frac{\bar{h}D}{Nu} = \frac{\varepsilon\sigma\left(T^2 + T_s^2\right)(T + T_s)}{G\left(Ar, \frac{H}{D}\right) \cdot 2Re^{0.5} \cdot (1 + 0.005Re^{0.55})^{0.5}} \quad (2.23)$$

A_r is the laser nozzle area defined as $\mathrm{A_r} = D^2/4r^2$. D is the diameter of a round laser nozzle and r is equivalent to the half of the effective melt surface which is subject to the overall heat transfer by $\bar{h}$. H is a vertical distance from the nozzle exit to the target surface, and H/D is the ratio of the distance to the nozzle diameter. There are some assumptions needed to adapt the impinging jet convention mode into the laser induced heat transfer: 1. the overall heat transfer rate depends on the property values averaged between the temperatures of liquid and vapor iron, 2. the pool velocities are suitable for the Reynolds' number instead of the actual injection velocity at the nozzle exit, and 3. a certain degree of the melt surface curvature is ignorable to apply the impinging jet convection mode.

Several preview simulations which run in the fast mode have been conducted to roughly determine the melt velocity for the estimation of the Reynolds' number. The preview simulations resulted in the range of velocities from 300 to 900 mm/s; therefore, the average melt velocity of 600 mm/s was selected referencing a recent laser spot welding study investigated by He, J. *et al.* [44]. Many computational welding researches noted that the melt tended to exhibit a roughly circular pattern of flow as shown in Figure 2.21 and the melt was assumed to be a Newtonian fluid exhibiting laminar flow [45-47]. Assuming the melt behaved as a Newtonian viscous laminar flow, the thermal conductivity for the melt pool could be approximated using equation (2.23) and the variables and material properties used for the calculation are provided in Table 2.3.

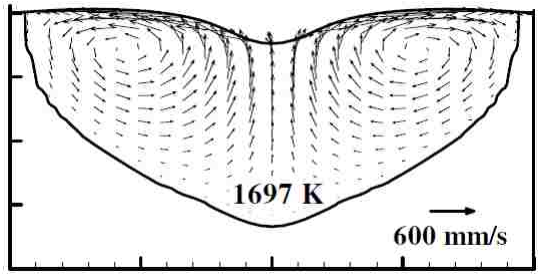

Figure 2.21 Laser spot welding of 304 stainless steel: laser power of 1300W, pulse duration of 4ms, and spot diameter of 0.42 mm [44]

Name	Symbol	Value
Surface temperature	T_s	3133K
Distance ratio	H/D	12
Nozzle diameter	D	0.4 mm
Viscosity	μ	~ 10^{-6} Pa s
Specific heat	c_p	~ 815.4 J/kg K
Melt surface velocity	V_s	~ 600 mm/s
Density	ρ	~ 1 kg/m^3
Emissivity	ε	0.35
Stefan-Boltzmann constant	σ	5.67×10-8 J/s m^2 K^4

Table 2.3 Thermo-physical properties used for Nusselt, Reynolds, and Prandtl numbers

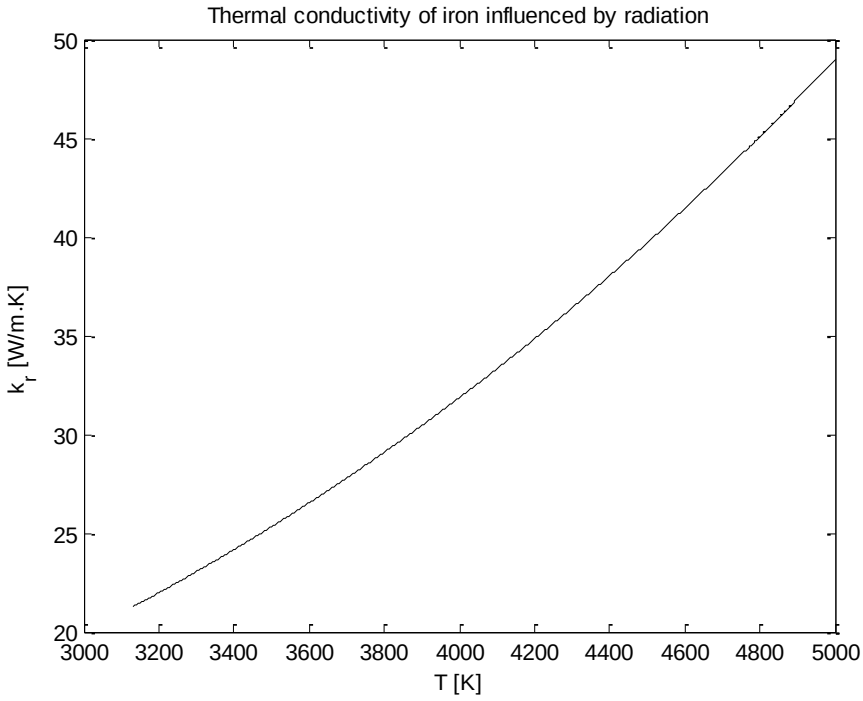

Figure 2.22 Thermal conductivity of iron influenced by radiation above the boiling point

In equation (2.23), k_r is the thermal conductivity including the influence of the radiation exposure above the boiling point. Assuming that the overall effective thermal conductivity had a relation of $\bar{k} = k + k_r$, this laser welding study used the profile of the thermal conductivities described in Figure 2.23.

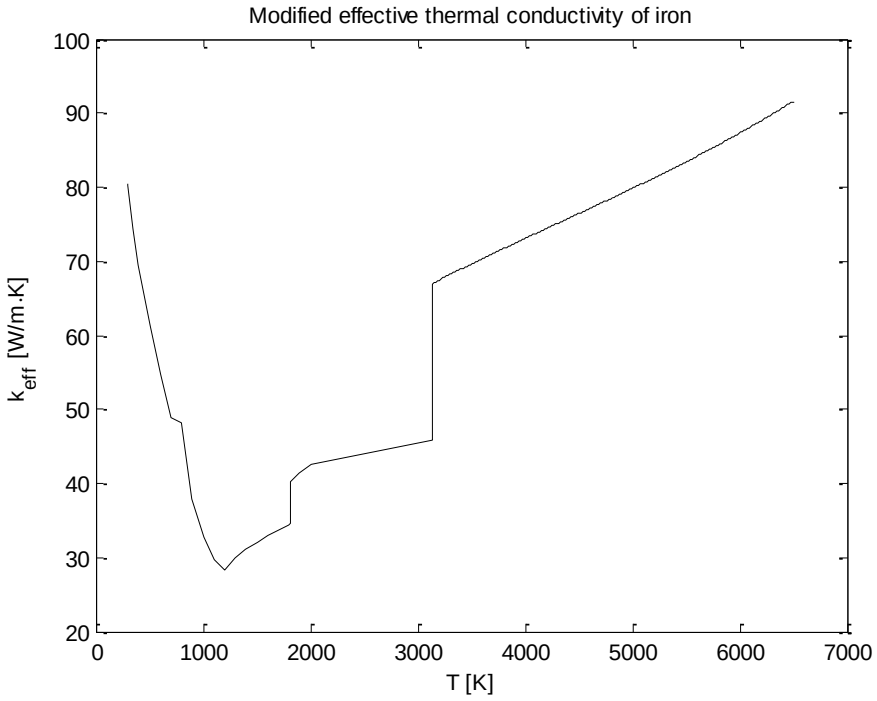

Figure 2.23 Modified effective thermal conductivity of iron as a function of temperature degrees in Kelvin

2.6 Coefficient of thermal expansion and ideal gas law

Basic thermal expansion is the rate of volume change when a material is heated or cooled. As thermal energy supplied is proportional to the amount of work done by system, the material expansion is corresponding to the degree change in temperature. The rate of thermal expansion is the derivative of volume with respect to temperature at constant pressure as the below.

$$\alpha_V = \frac{1}{V}\left(\frac{\partial V}{\partial T}\right)_p \tag{2.24}$$

The mathematical expression in equation (2.24) is suitable for a solid, liquid, and gas. Corresponding to the dimensions of interest, the different coefficients of thermal expansion, e.g., volumetric, area, or linear expansion, can be used. Assuming that a material expands in all directions at the same rate, the volumetric thermal expansion is reduced to the linear thermal expansion. In the F.E. based laser welding analysis, equation (2.25) is more practical due to the use of an isotropic thermal expansion coefficient.

$$\alpha_L = \frac{1}{L}\left(\frac{\partial L}{\partial T}\right) \tag{2.25}$$

$$\alpha_V = 3\alpha_L \tag{2.26}$$

The subscript L indicates a particular length of interest and $\partial L/\partial T$ is the rate of elongation per degree change in temperature. Therefore, α_L is often called as the fractional increase in length for a one-degree change in temperature. In the SI system the unit of the linear thermal expansion coefficient is [m/m ·℃], [$℃^{-1}$], or [K^{-1}].

The ratio in equation (2.26) is because of that a unit volume is composed of three equal unit lengths ($V = L^3$) in Cartesian coordinates. Infinitesimal increase in volume is expressed as $V + \Delta V$, similarly the amount of change in terms of length is $(L + \Delta L)^3$. By the use of Taylor series expansion, thermal effect on the infinitesimal volume change yields the relation of equation (2.26).

Thermal expansion of solid does not change much over the range of temperatures even though the thermal expansion coefficient of metals and alloys is highly temperature-dependent. The thermal expansion coefficient of pure iron is about 11.8×10^{-6} m/m·K at room temperature and it does not exceed 1 order of magnitude with increasing temperature up to the melting point. Figure 2.24 is the plot of the change in thermal expansion coefficients which compare the actual measurements by Nix F. C. *et al.* with results from Grüneisen theory [48].

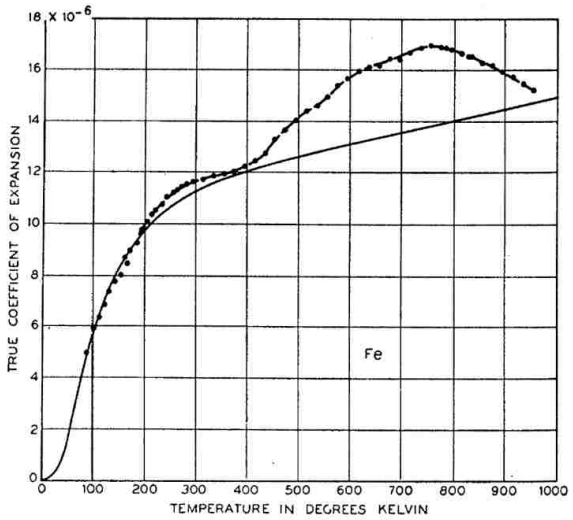

Figure 2.24 True coefficient of thermal expansion vs. temperature for iron: The dots are experimentally derived coefficients, and the solid curve is the Grüneisen plot [48]

Austin, J. B. *et al*. also measured the linear thermal expansion coefficient from room temperature to 950 ℃ where the solid-state phase change was assumed to be occurred at [49]. The profile in Figure 2.25 is similar to the results from Nix F. C. *et al.* even though their theoretical approaches using Grüneisen's parameters do not match well with the experimental measurements approximately over 450 ℃.

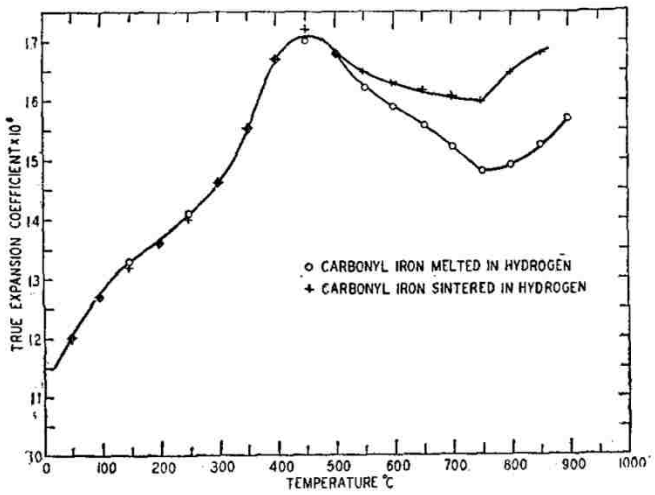

Figure 2.25 Thermal expansion coefficient of iron as a function of temperature [49]

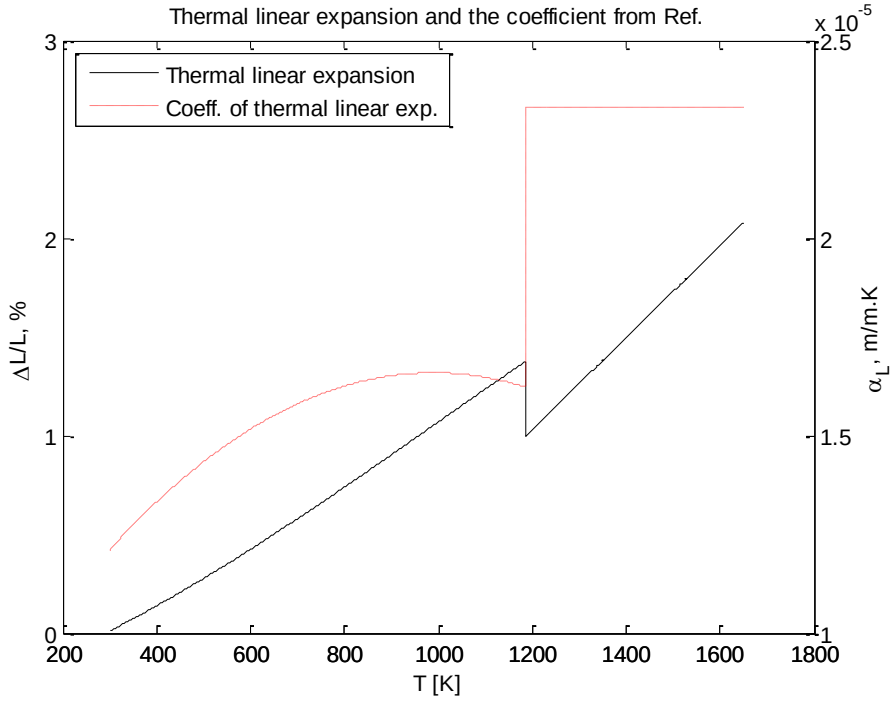

Figure 2.26 Coefficient of thermal linear expansion of iron

Since the coefficient of thermal expansion does quantitatively have a slight difference with increasing temperature, a data fitting of the slope of the coefficient profiles which can be equated as a function of temperature is more practical to make the nonlinearity of the coefficients suitable for numerical computation with well predictable values. Reference data based on many measurements in the temperature range 5K to 1807K have been used to approximate the relation between temperature and linear thermal expansion into an appropriate mathematical expression [27]. Using the reference, a set of experimental results was properly adjusted for the coefficients of thermal expansion to be associated with the several discrete ranges of temperatures, e.g., 300K to 1185K and 1185K to 1650K. An allotropic transformation has been expected at 1185K, and the effect of the solid-state phase change is clearly noticeable in the profile. The plot for the adjusted coefficients is displayed in Figure 2.26

The volumetric thermal expansion of iron vapor could be calculated assuming that the iron obeyed the idea gas law. Differentiating equation (2.27) with respect to temperature, the relation between temperature and volume resulted in equation (2.28) at constant pressure. The coefficient of thermal expansion in isobaric condition is finally expressed as equation (2.29).

$$\ln\left(V = \frac{nRT}{P}\right) \quad \rightarrow \quad \ln V = \ln T + \ln\frac{nR}{P} \tag{2.27}$$

$$\frac{d}{dT}\left\{\ln V = \ln T + \ln\frac{nR}{P}\right\} \quad \rightarrow \quad \frac{1}{V}\left(\frac{\partial V}{\partial T}\right)_p = \frac{1}{T} \tag{2.28}$$

$$\alpha_V = \frac{1}{V}\left(\frac{\partial V}{\partial T}\right)_p = \left(\frac{1}{V}\cdot\frac{\partial V}{\partial T}\right)_p = \frac{1}{T} \tag{2.29}$$

Finally the modified linear thermal expansion coefficients of iron are plotted on a log scale in Figure 2.27 over the temperature range from room temperature to 5000K. The magnitude

for α_L while heating and cooling cycles is as the follows: 1×10^{-5} to 3×10^{-5} m/m K for solid, ~ 4×10^{-5} m/m K for liquid, and 6.67×10^{-5} to 1×10^{-4} m/m K for gas.

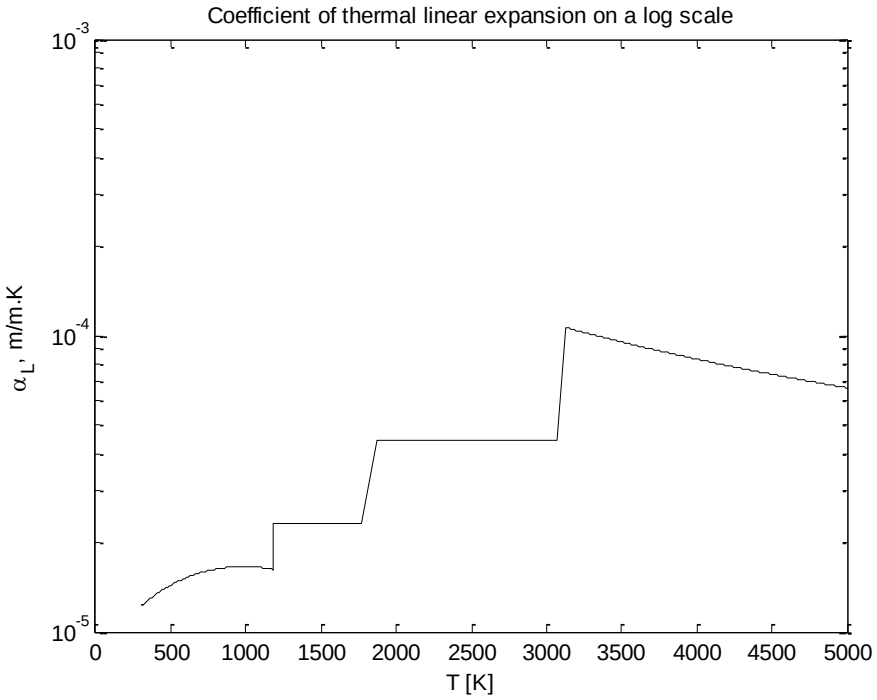

Figure 2.27 Modified coefficient of linear thermal expansion as a function of temperature degrees in Kelvin

2.7 Young's modulus

Elastic modulus is a measure of resistance to elastic deformation. Elastic modulus is often called as modulus of elasticity, and Hooke's law represents the elastic material behavior until a material begins to deform plastically. A stress point where plastic deformation occurs is the yield strength of a material; the elastic modulus of a material denotes the ratio of stress to strain until this yield point which a material is ready to exhibit non-elastic behaviors.

In general, Young's modulus indicates the elastic modulus of a material, and the definition is the ratio of uniaxial tensile stress to uniaxial tensile strain. The ratio is usually constant because stress is proportional to load applied, and strain is a measure of elastic deformation according to the Hooke's law. A mathematical expression of Young's modulus is given in equation (2.30).

$$E = \frac{\sigma}{\varepsilon} = \frac{F/A_0}{\Delta L/L_0} \tag{2.30}$$

In the mathematical expression of equation (2.30), E is a symbol for Young's modulus, and the unit in the SI system is [N/m^2] or [Pa].

Young's modulus is experimentally determined from the slope of a stress-strain diagram during tensile tests. Hence, Young's modulus can be used to measure the elongation or compression of a material unless the applied stress does not exceed the yield strength. Metals and alloys often exhibit linear elasticity on a stress-strain diagram within the region that follows the Hooke's Law. If a material is homogeneous isotropic, Young's modulus has all equivalent values for all directions in Cartesian coordinate system. However, Young's modulus in welding has to be a function of temperature since the strength of a material is vulnerable to thermal attack.

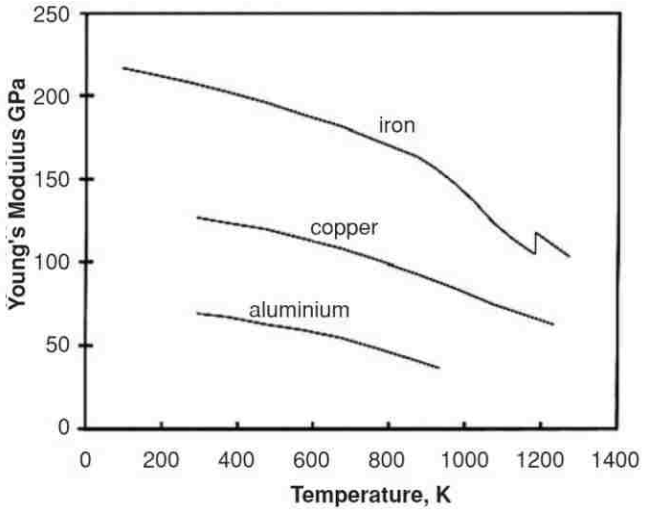

Figure 2.28 Variation of Young's moduli with temperature [50]

Young's modulus of pure iron is highly susceptible to the metallurgical effect of phase transitions e.g., allotropic, solid-liquid, and liquid-gas transformations, similar to other thermo-physical properties. Figure 2.28 shows the evidence of the allotropic transformation of iron. The decrease in the elastic modulus of iron is noticeable in the temperature range of 1150K to 1200K [50]. The Young's modulus of pure iron is 211 GPa at room temperature, but there are not many available reference data with increasing temperature.

Assuming that the elastic modulus of low alloy steel, AISI A182 Grade F22 (2¼% Cr 1% Mo), is similar to that of pure iron, a series of elastic moduli of the Chromium-Molybdenum alloy steel [51] has been used to replace the unknowns of pure iron. Young's modulus of Grade F22 is in the range of 190 to 210 GPa at room temperature, and the melting occurs in the temperature range of 1450 ℃ to 1510 ℃ depending upon its grade. Since the melting point of pure iron varies from 1500 ℃ to 1540 ℃, there are only slight differences in terms of a few mechanical properties. The elastic moduli of Grade F22 fall gradually down with increasing temperature, and the plot of the elastic moduli is in Figure 2.29.

Low carbon steel DC04 of which a final weld shape was investigated by Pornsak, T. [4] was compared for result discussion. The elastic moduli of DC04 are also described as shown in Figure 2.29.

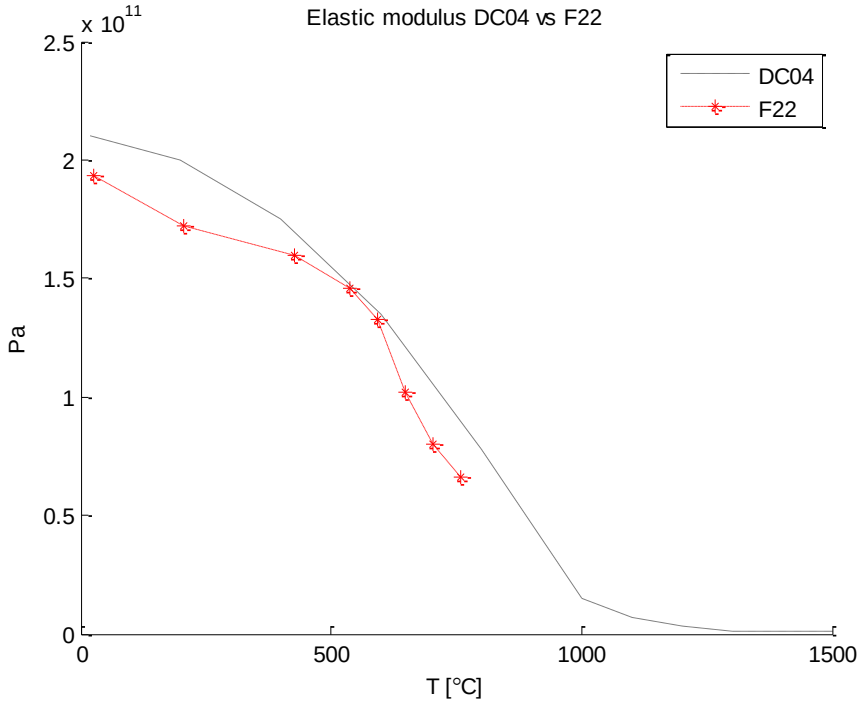

Figure 2.29 Modulus of elasticity with increasing temperature

Chapter 3 Fundamental study on modeling of laser welding

3.1 Two dimensional cross-section system modeling

In numerical laser welding, a heat source function travels along a weld line. A weld line lies on the z-axis as shown in Figure 3.1 since the direction of the moving heat source is determined by a users' defined coordinate system. The figure shows that a basic disk heat source model slides on the top surface of a base metal along the z-directional axis. The welding path indicates the motion of the heat source because a heat source model is usually a function of time in the transient welding analysis.

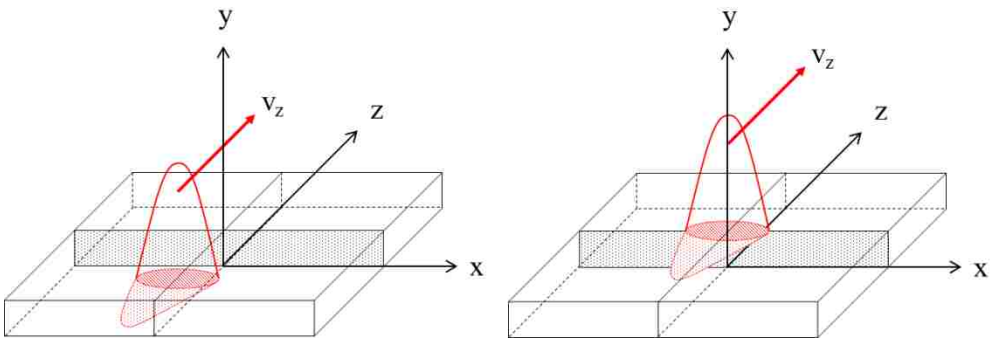

Figure 3.1 Disk laser heat source model on a thin sheet metal structure

The use of a 2D cross-section heat source model as in Figure 3.2 however is much more efficient to perform a fast computation than an operating the disk or a volumetric heat sources in 3D domain because a use of fewer elements usually consumes less computation time in numerical simulation. As shown in Figure 3.3, it is common that the image of the microstructure is obtained at the cross section which is normal to the weld line in order to estimate the depth and width of the melt pool. Similar to the experimental observation, the use of the cross-section is assumed to be a proper choice to measure the melt pool geometries.

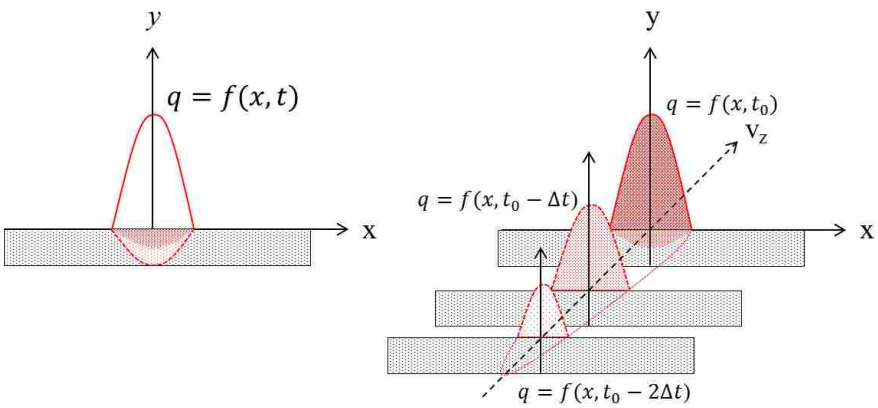

Figure 3.2 Time dependent laser heat source on a 2D cross section area

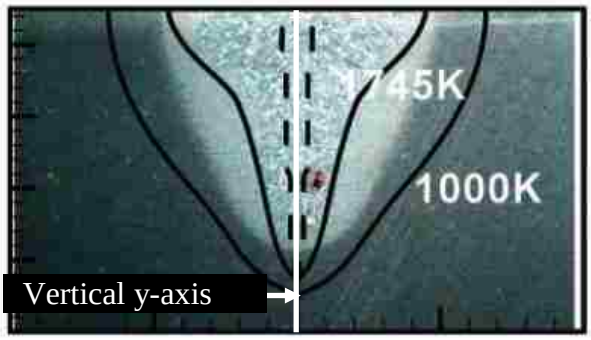

Figure 3.3 laser welded A131 structural steel: 10 mm thickness, 1.9 kW laser power [52]

As shown in Figure 3.2, the application of transient linear heat distribution was applied on the top of the 2D cross section during this laser welding simulation research. In contrast to most previous numerical laser welding researches, the applied 2D cross-section enabled a full contribution to a fast coupled thermal-fluid-structure system analysis. This modeling was a new approach which has never been used for the study on the weld formations and the post-weld behaviors although the cross section model has been involved in many welding simulation processes.

The fluid motion in the direction of welding was assumed to be less effective for the formation of the final weld. The z-directional moving components were therefore less important. The z-directional stress components were also thought to be less important because welding distortions and residual stresses were mostly dependent on the directions normal to the weld line. As the y-axis symmetric melts circulation and active stress components were described in the x-y plane of the cross-section, the 2D analysis was a dominant thermal-fluid-structure system in this laser welding process.

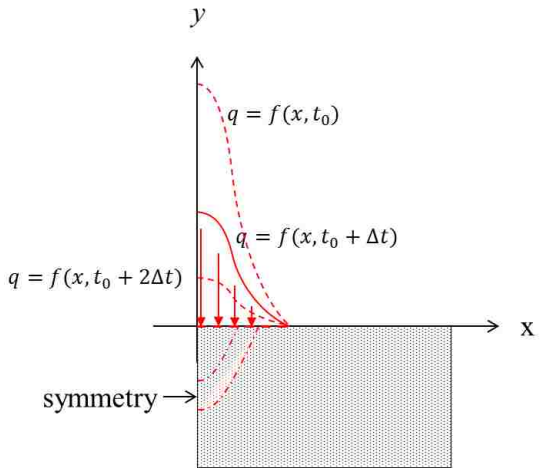

Figure 3.4 2D symmetric cross-section model for thermo-fluid-structure analysis

In this study, the 2D model performed the coupled simulation in the x-y domain, and the time dependent heat function was computed proportional to their geometric configuration by increasing or decreasing intensities on the top layer. Since a transient analysis has close connection with the continuously ongoing welding process, the time dependent heat input was devised expecting the influence of real-time heat source approach. A schematic presentation of the 2D systems with the heat source application is described in Figures 3.5, and the applied thermal boundary constraints are in Figure 3.6.

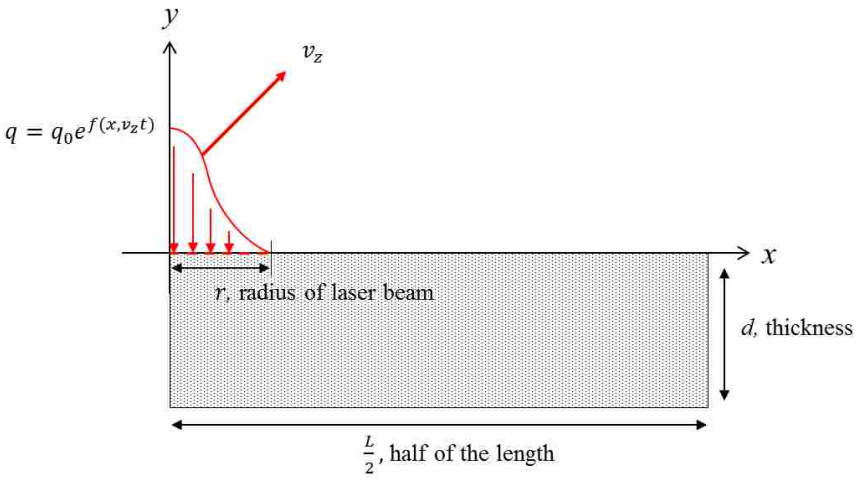

Figure 3.5 2D cross-section geometries

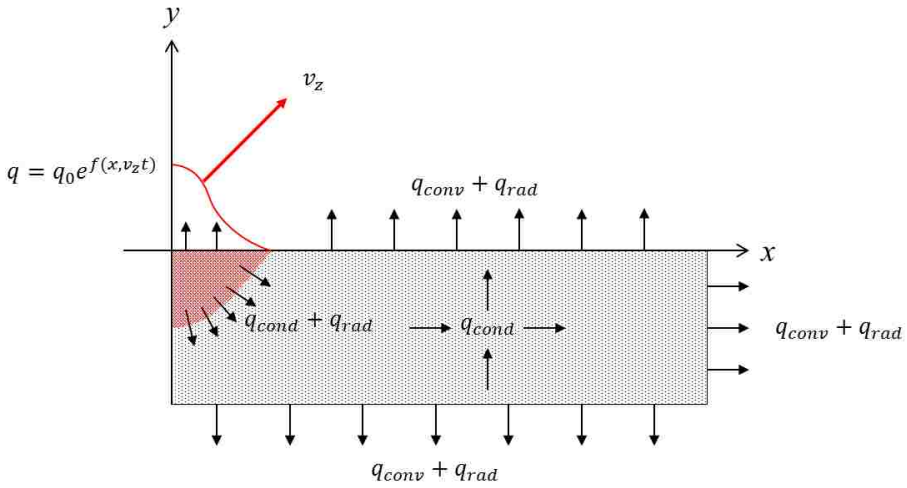

Figure 3.6 2D system boundary conditions

3.2 Heat source modeling

This welding study did not rely on the use of predefined heat source distribution that has better been used to characterize the evolution of the weld pool. The predetermined heat modeling can be suitable to certain types of laser welding applications where the melt pool shape and size is not critical.

Referring to the history of the numerical welding processes, Gaussian distribution of surface heat flux has been a realistic heat source modeling in most welding processes [21]. The Gaussian heat distribution has provided a useful approximation of the heat density in the welding processes [12, 53]. The first empirical heat source proposed by Pavelic *et al*. was a 2D circular disk heat model on the basis of Gaussian distribution, as in Figure 3.1 [54]. The mathematical expression of the adaptive disk heat source model is described below.

$$\dot{q} = Q_0 \cdot \exp[-Cr^2] \tag{3.1}$$

where C is a distribution width coefficient, and r is a radial distance from the heat source center on the circular disk. Q_0 is a rate of heat energy input equivalent to ηVI and yields the maximum heat density at the center of heat source model. The use of exponential function contributes to heat concentration at the core and rapid deduction of thermal energy increasing the radius of the disk. In transient computation the velocity of the circular disk heat allows the disk move along a desired weld line, and geometric heat densities of the laser beam source should be redefined to satisfy a normal heat distribution on the proposed 2D system.

Assuming that the laser heat source is traveling on the z-axis as shown in Figure 3.1, the temperature gradient is influenced by the location of heat source center. A process of high-intensity laser welding is time-sensitive because the change in welding velocity has a great effect on heat diffusion. As a result of that, a laser heat source model should be a function of time and distance for accurate estimations of welding phenomena.

The heat density is defined as a function of time and x-coordinates and applied in the 2D cross section as shown in Figure 3.4. The maximum of the heat density is located at the center of the heat source and the minimum is at the boundary of the Gaussian function along the x-axis. The surface where the laser beam is targeted on is influenced directly by the heat source as given in equation (3.2). This assumption makes there is no predetermined penetration of the heat density into the proposed 2D cross section model. m ($m = 3$ by Goldak et al. [54]) is a heat distribution factor, and z_0 is unit thickness for the conversion of planar heat into linear heat distribution. r_0 is a radius of laser beam, and πr_0^2 is an approximate area of direct laser projection. The definition of q_0 is $Q_0 z_0 / \pi r_0^2$, therefore $\dot{q}$ is the rate of heat generation per unit length for the linear heat allocation on the 2D cross section.

$$\dot{q} = q_0 \cdot \exp\left[-m\left(\frac{x^2}{r_0^2}\right)\right] \cdot \exp\left[-m\left(\frac{(v_z t)^2}{r_0^2}\right)\right] \tag{3.2}$$

$$\dot{q} = q_0 \tag{3.3}$$

$$\dot{q} = q_0 \cdot \frac{1}{2}\left\{\mathrm{erf}\left[\frac{r_0 + x}{m}\right] + \mathrm{erf}\left[\frac{r_0 - x}{m}\right]\right\} \cdot \frac{1}{2}\left\{\mathrm{erf}\left[\frac{r_0 + v_z t}{m}\right] + \mathrm{erf}\left[\frac{r_0 - v_z t}{m}\right]\right\} \tag{3.4}$$

On the other hand, verification of the Gaussian heat modeling is a matter how the distribution yields good suitability for the laser welding processes. A constant heat density model in equation (3.3) is introduced for the comparison of suitability between the Gaussian variation and the constant heat flux, although the Gaussian distribution is known to be a reliable approximation in the numerical welding process. Another uniform heat density in equation (3.4), a hypothetical heat density flattening the center concentrations of the Gaussian flux efficiently, is proposed using the mathematical expression of multiple error functions. The shape comparison between the equations (3.2) and (3.4) is provided in Figures 3.7 and 3.8. The heat density models subject to the welding study are listed in Table 3.1.

No.	Heat Source Modeling	Mathematical Expression
1	Gaussian heat distribution	$\dot{q} = q_0 \cdot \exp\left[-m\left(\frac{x^2}{r_o^2}\right)\right] \cdot \exp\left[-m\left(\frac{(v_z t)^2}{r_0^2}\right)\right]$
2	Constant heat distribution	$\dot{q} = q_0$
3	Uniform heat distribution	$\dot{q} = q_0 \cdot \frac{1}{2}\left\{\text{erf}\left[\frac{r_0 + x}{m}\right] + \text{erf}\left[\frac{r_0 - x}{m}\right]\right\} \cdot \frac{1}{2}\left\{\text{erf}\left[\frac{r_0 + v_z t}{m}\right] + \text{erf}\left[\frac{r_0 - v_z t}{m}\right]\right\}$

Table 3.1 Heat source models – geometrical time dependent heat distribution

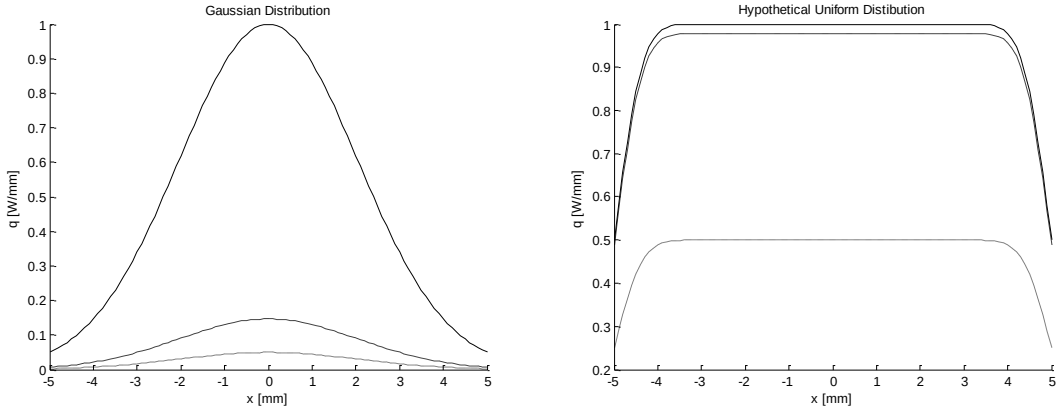

Figure 3.7 Gaussian and hypothetical uniform heat density functions with arbitrarily selected $q_0 = 1$ W/mm, $r_0 = 5$ mm, and $v_z = 10$ mm/s: solid line at $t = 0$ sec, dashed line at $t = 0.4$ sec, and dotted line at $t = 0.5$ sec while heat source is moving along the weld line normal to the proposed 2D cross section

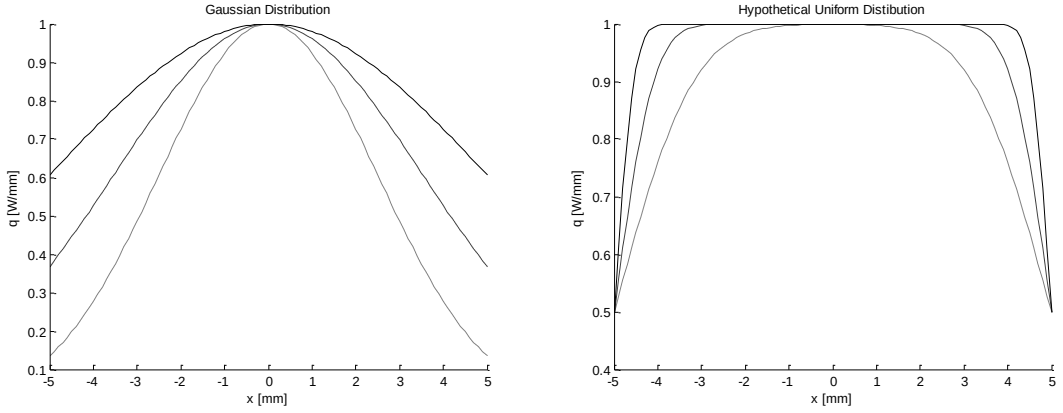

Figure 3.8 Gaussian and hypothetical uniform heat density functions with arbitrarily selected $q_0 = 1$ W/mm, $r_0 = 5$ mm, and $v_z = 10$ mm/s: solid line at $m = 0.5$, dashed line at $m = 1$, and dotted line at $m = 2$ while varying heat distribution factors

3.3 Theoretical approach for thermo-fluid analysis

Energy balance is the basis for modeling the heat transfer system. Most conductive heat transfer in solid materials is governed by conservation of heat energy; the energy balance results in a simple thermal conduction to obtain temperature distribution in the numerical laser welding simulation. Temperatures obtained through the energy balance in equation (3.5) are employed to estimate residual stresses using a functional relation of thermal expansion.

$$\rho c_p \frac{\partial T}{\partial t} = k\nabla^2 T + \dot{q} \tag{3.5}$$

The material properties (ρ: density, k: thermal conductivity) are assumed to be constant or temperature dependent. Specific heat c_p is given similar to other material properties, but the latent heat of fusion which is defined as $H = \int \rho c_p dT$ allows particular modification on the properties in the melting point and boiling point.

$k\nabla^2 T$ is thermal conduction crossing the boundary of each element and $\dot{q}$ indicates the internal or boundary heat generation rate which is the source term of the moving laser heat density. Most thermal systems are in the forms of differential equations to solve for the overall temperature distributions. In the field of numerical analysis, applying Galerkin's technique into the finite element algorithm is a common method to handle the nonlinear thermal conduction. Solving the nonlinear equation (3.5), all nodal temperatures are obtained at each time step taking matrix inversion [54, 55].

As several irregular weld shapes have been found observing laser welded microstructures, the melt pool dynamics and the pool shape are thought to have a close connection one another during laser welding. As surface tension of the melt yields the relative stability of surface free energy on the melt surface, the stability is known to have a great effect on the melt flow and the

formation of the pool shape. In order to find the effects of the surface tension stresses, the extra work done by the melt flow is required in the equation of thermal energy balance.

$$\rho c_p \frac{\partial T}{\partial t} = k\nabla^2 T + \dot{q} + \dot{W}_\gamma \tag{3.6}$$

$$\gamma = \mu \frac{\partial u}{\partial y} = f \frac{\partial \gamma}{\partial T} \frac{\partial T}{\partial x} \tag{3.7}$$

An additional surface work energy term is defined as $\dot{W}_\gamma = \int \gamma dA$ and assumed to be active over the melting point, and the surface tension γ in equation (3.7) is considered as a major contribution to widen the melt pool. Dynamic viscosity μ is a temperature dependent variable as the same as $\rho, c_p,$ and k. A sudden viscosity drop is expected in a narrow melting point range since vigorous fluid motion occurs at relatively low viscosity. f is the mass fraction of liquid representing material phase transformation [15, 52]. The value for f varies from 0 to 1 within a solid-liquid mixed region, and it becomes 1 where all materials are in the liquid phase. Initial and real-time temperature updates are required to decide the activation of the surface work energy of equation (3.6), and experimental results of the surface tension gradients are provided for the surface tension within a given temperature range [56].

On the other hand, the dynamics of heat and fluid flow in the melt is another potential factor inducing the instability of the melt pool formation. Therefore, conservation of heat energy in fluid is required to measure the effect of the fluid flow.

$$u\frac{\partial u}{\partial x} + v\frac{\partial u}{\partial y} + \frac{\partial u}{\partial t} = -\frac{1}{\rho}\frac{\partial p}{\partial x} + \frac{\mu}{\rho}\left(\frac{\partial^2 u}{\partial x^2} + \frac{\partial^2 u}{\partial y^2}\right) \tag{3.8}$$

$$u\frac{\partial v}{\partial x} + v\frac{\partial v}{\partial y} + \frac{\partial v}{\partial t} = -\frac{1}{\rho}\frac{\partial p}{\partial y} + \frac{\mu}{\rho}\left(\frac{\partial^2 v}{\partial x^2} + \frac{\partial^2 v}{\partial y^2}\right) \tag{3.9}$$

$$\rho c_p \left(u\frac{\partial T}{\partial x} + v\frac{\partial T}{\partial y} + \frac{\partial T}{\partial t}\right) = \frac{Dp}{Dt} + k\nabla^2 T + \dot{q} + \dot{W}_v + \mu\Phi \tag{3.10}$$

Conservations of linear momentums along the x- and y-axis are expressed in equations (3.8) and (3.9) to evaluate x- and y-directional fluid velocities in the melt pool. A heat and fluid energy

balance in equation (3.10) is used to obtain the temperature profile. u and v ($V_x = u, V_y = v$) are velocity components in the x and y directions ($X_x = x, X_y = y$), and the velocities and their gradients remain inactive unless temperature rises over the melting temperature. $\dot{W}_v$ and $\mu\Phi$ are the results of the viscous liquid metal flow when solid transforms into liquid. The two terms indicate viscous work and viscous dissipation respectively [57, 58].

The existence of surface tension results in equation (3.11) and the surface tension has high potential to form the irregular shaped melt pool. Detailed expressions of viscous work and viscous dissipation are explained in equations (3.12) and (3.13) where the numerical symbols i and j satisfy the relation $i \neq j$ and $i, j = x, y$.

$$\rho c_p \left(u\frac{\partial T}{\partial x} + v\frac{\partial T}{\partial y} + \frac{\partial T}{\partial t} \right) = \frac{Dp}{Dt} + k\nabla^2 T + \dot{q} + \dot{W}_v + \mu\Phi + \dot{W}_\gamma \tag{3.11}$$

$$\Phi = 2\sum_i \left(\frac{\partial V_i}{\partial X_i} \right)^2 + \sum_i \sum_j \left(\frac{\partial V_j}{\partial X_i} + \frac{\partial V_i}{\partial X_j} \right)^2 \tag{3.12}$$

$$\dot{W}_v = \mu \sum_i \sum_j \frac{\partial}{\partial X_i} \left(\frac{\partial V_j}{\partial X_i} + \frac{\partial V_i}{\partial X_j} \right) V_j \tag{3.13}$$

Additional linear momentum terms, $S_u = Au$ and $S_v = Av$, can be appended to the equations (3.8) and (3.9) to account for the solid to liquid phase transformation in the melt pool. A is a phase change parameter which is a function of a mass fraction of liquid f [15, 52]. As explained in the earlier chapter, the modified pure iron has a full participation to the required phase transformations. The mathematical expressions of the additional momentum equations are already involved during the evaluation of the thermo-physical properties. In this study, the faction of liquid is modified taking a linear interpolation; two available upper and lower limits are taken within the phase change to proportionally compute the mass fraction of liquid. The limits are the melting and boiling points of pure iron, and the solid-liquid and liquid-gas mixture phases are assumed to exist in the temperature ranges before and after the melting and boiling points.

The summary of governing equations and their descriptions is listed in Table 3.2, and the boundary conditions required for thermo-fluid analysis is described in Figure 3.9.

No.	Governing Equation	Mathematical Expression
1	Energy balance	$\rho c_p \frac{\partial T}{\partial t} = k\nabla^2 T + \dot{q}$
2	Energy balance with effect of surface tension	$\rho c_p \frac{\partial T}{\partial t} = k\nabla^2 T + \dot{q} + \dot{W}_\gamma$
3	Energy balance in fluid	$\rho c_p \left(u\frac{\partial T}{\partial x} + v\frac{\partial T}{\partial y} + \frac{\partial T}{\partial t}\right) = \frac{Dp}{Dt} + k\nabla^2 T + \dot{q} + \dot{W}_v + \mu\Phi$
4	Energy balance in fluid with effect of surface tension	$\rho c_p \left(u\frac{\partial T}{\partial x} + v\frac{\partial T}{\partial y} + \frac{\partial T}{\partial t}\right) = \frac{Dp}{Dt} + k\nabla^2 T + \dot{q} + \dot{W}_v + \mu\Phi + \dot{W}_\gamma$

Table 3.2 Governing equations – conservation of energy balance

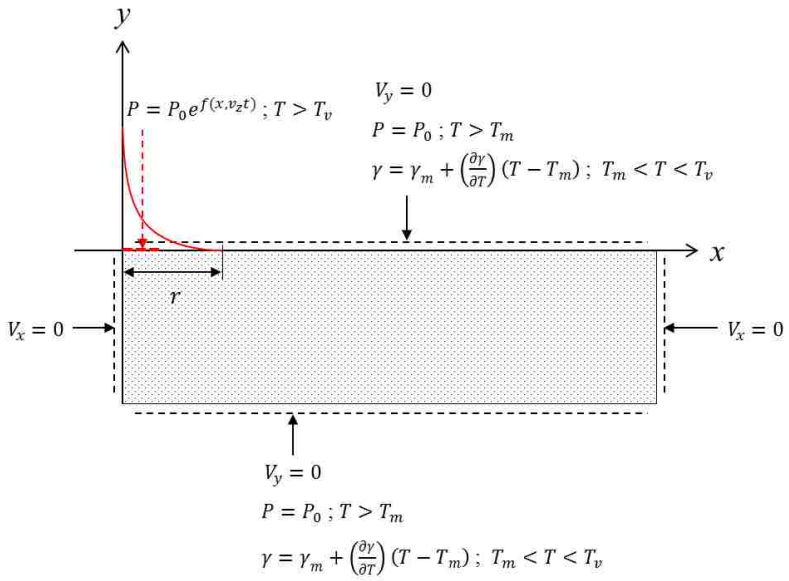

Figure 3.9 Boundary conditions for thermo-fluid analysis

3.4 Surface tension and Marangoni convection

Wetting is one of the important thermo-physical characteristics due to the effect of the melt surface tension in the laser welding process. When a material melts, the wetting behavior exhibits surface tension of the liquid between the melt and not-yet-melted material. Surface tension is a measure of the surface energy that a liquid has to minimize its surface area. Surface tension generally acts tangential to the liquid surface reducing the surface energy of the liquid.

Marangoni convection is the heat transfer between the molten material and the surrounding air, and the surface tension gradient induces the Marangoni convection along the melt pool surface layer due to the temperature variations. Surface tension is dependent on a temperature gradient which can be produced by temperature difference at the liquid/gas interface. In brief, surface tension decreases with the increase of temperature, reaching 0 at the melting temperature as expressed in equation (3.14).

$$\gamma = \gamma_m + \left(\frac{\partial \gamma}{\partial T}\right)(T - T_m) \tag{3.14}$$

γ is surface tension at temperature T [℃], and γ_m is surface tension at the melting point T_m [℃]. A gradient, which is surface tension with respect to temperature $\left(\frac{\partial \gamma}{\partial T}\right)$, is a thermal coefficient of surface tension.

The gradient causes the melt flow by taking the differences in surface tension gradients into consideration of strong interrelation; the melt is subject to flow from the higher gradient to the lower gradient. Pure iron collects relatively low and linear surface tension profiles than alloying metals whose magnitude of the surface tension increases with the amount of the iron content [59]. Therefore, the melt is assumed to flow from the center of the pool to the solid boundary which is not yet melted as shown in Figure 3.10 due to the nearly constant $\frac{\partial \gamma}{\partial T}$ ratio.

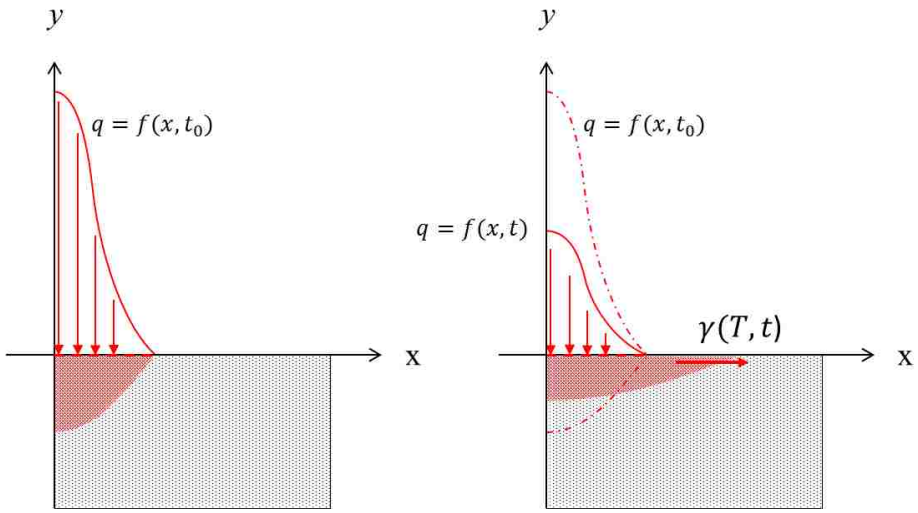

Figure 3.10 Schematic diagram of temperature dependent surface tension on the melt top layer

The thermal coefficient is a determinant of Marangoni convection which influences the shape of the melt pool. Marangoni number, Ma, is a dimensionless number which is proportional to the thermal coefficient of surface tension which is divided by viscosity and thermal diffusivity as in equation (3.15).

$$Ma = \frac{\partial \gamma}{\partial T} \cdot \frac{1}{\mu \alpha} \cdot L^2 \cdot (T - T_m) \tag{3.15}$$

μ is dynamic viscosity [N s/m], α is thermal diffusivity [m^2/s], and L is characteristic length [m]. Keene B. J. investigated thermo-physical properties of liquid iron. In the research, the surface tension of liquid iron was expressed as a function of temperature. The least-square fit of surface tension was originally given for the range of temperatures from 1530 ℃ to 1862 ℃ [56]. However, the surface tension profiles have been modified over the temperature range of 1540 ℃ to 2860 ℃ assuming no significant change in the decreasing tendency with increasing temperature. Mean γ at the melting point is 1862 mN/m, the surface tension of liquid iron is expressed as $\gamma = 1862 - 0.39(T - T_m)$ mN/m. The profiles are graphically displayed as Figure 3.11.

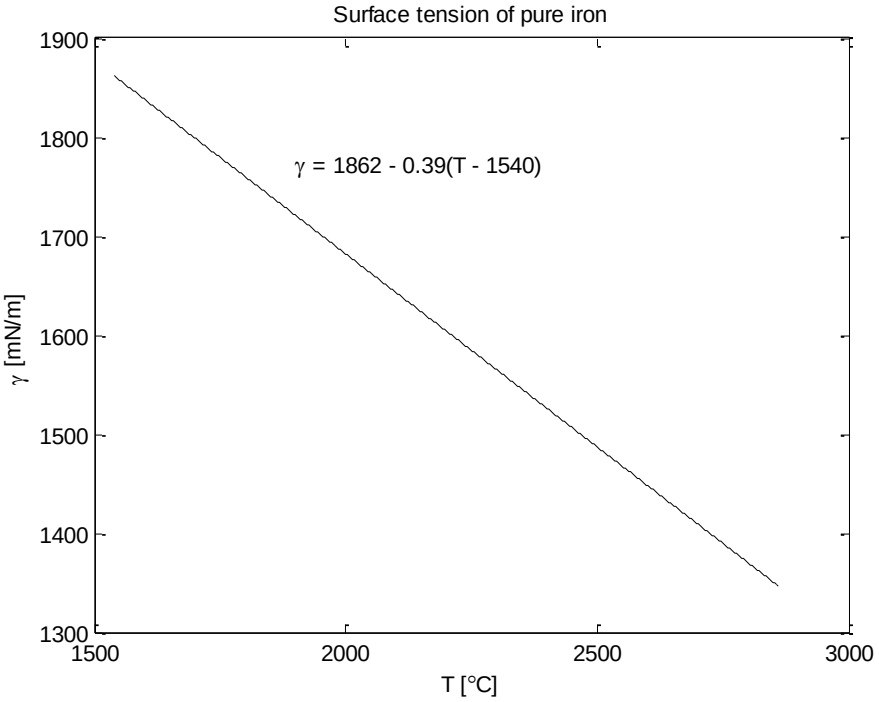

Figure 3.11 Surface tension of pure iron [56]

3.5 Recoil pressure and melt penetration

In general, the vapor pressure means the evaporation rate of liquid, and the evaporation is the process of molecules escaping from the liquid state. Therefore, the boiling temperature is a measure of the moment when the vapor pressure of iron molecules is equivalent to the ambient atmospheric pressure. The equilibrium vapor pressure over the boiling point is practically used to obtain the recoil pressure in relation to rapid iron evaporation. The recoil pressure work in deep laser welding is described in Figure 3.12.

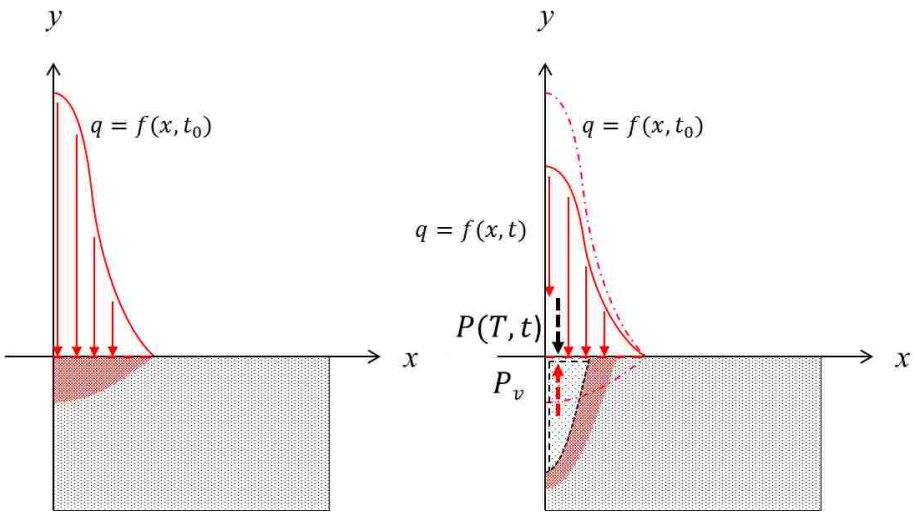

Figure 3.12 Schematic diagram of recoil pressure effect in deep laser welding

The equilibrium between liquid iron and the vapor depends on the temperature of the melt pool. The 1st and 2nd laws of thermodynamics provide an equation for the vapor pressure as a function of temperature. However, the variation of vapor pressure versus temperature may not be in a straight line because the saturation pressure of the iron vapor more rapidly increases while the temperature rises. The relation between vapor pressure and temperature can be explained with

the Clausius-Clapeyron equation. Equation (3.16) is the Clausius-Clapeyron equation to obtain the vapor pressure which varies with the temperature as given in Table 3.3.

$$P = P_0 \cdot \exp\left[\frac{\Delta H_v}{R_u}\left(\frac{1}{T_v} - \frac{1}{T}\right)\right] \tag{3.16}$$

T [K]	P [MPa]
3133	101.35
3135	102.20
3200	133.20
3400	282.47
3600	551.00
3800	1001.83
4000	1715.82
4200	2791.87
4400	4346.06
4600	6510.05
4800	9428.64
5000	13256.97

Table 3.3 Vapor pressure of iron as a function of temperature degrees in Kelvin

Name	Symbol	Value
Atmospheric pressure	P_0	101.35 MPa
Boiling point	T_v	2860 ℃
Heat of vaporization	ΔH_v	340 kJ/mol
Universal gas constant	R_u	8.3145 J/mol Ⱪ

Table 3.4 Thermo-physical properties of iron used in the Clausius-Clapeyron equation

In equation (3.16), P indicates vapor pressure which is a function of temperature, and P_0 is the atmospheric ambient pressure on the melt pool. ΔH_v is heat of vaporization at the boiling point T_v, and the universal gas constant R_u is 8.314462 J/mol K in the SI unit system.

If we approximate that: 1. the volume of gas is much larger than that of liquid or solid, and 2. the evaporated gas obeys the ideal gas law, the Clausius-Clapeyron equation can be valid for all types of phase changes, e.g., solid to liquid, solid to gas, and liquid to gas. Therefore, equation (3.16) is suitable for measuring the vapor pressure of iron, and the required thermo-physical properties are given in Table 3.4.

This laser welding study requires verification of the obtained values from the Clausius-Clapeyron equation because the vapor pressure may have a great effect on the thermal or thermo-fluid simulation result. Reference data investigated by Hultgren R. *et al.* [29] is graphically compared in Figure 3.14 with the calculated values to verify the reliability of the Clausius-Clapeyron equation. As shown in Figure 3.13, the vapor pressure of iron from the Clausius-Clapeyron equation agrees with the referenced vapor pressure values. A sixth order polynomial fit of the vapor pressure [Pa] yields equation (3.17) as a function of temperature degrees in Kelvin.

$$P = 7 \cdot 10^{-15}T^6 - 5.9 \cdot 10^{-11}T^5 + 2 \cdot 10^{-7}T^4 - 3.3 \cdot 10^{-4}T^3 + 0.28T^2 - 110T - 1.6 \cdot 10^4 \quad (3.17)$$

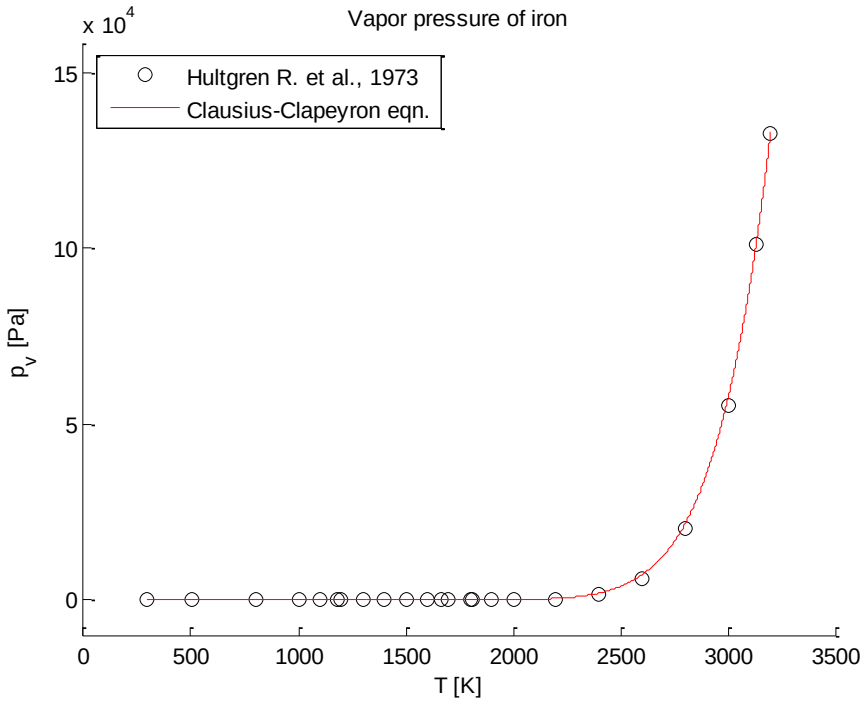

Figure 3.13 Vapor pressure of iron from Hultgren R. *et al*. and from the Clausius-Clapeyron equation

3.6 Welding and dimensionless parameters

Laser beam application is classified into several thermal processes, e.g., coating, welding, and cutting, according to its intensity on a target substrate [62]. The intensity of the laser is the highest priority when deciding the manufacturing processes. The categorized items from coating to cutting are dependent on the application of appropriate laser power. The thickness of the substrate also influences on the laser intensity, and the change in laser power is subject to the material components of the weld. A material's surface reflectance has high potential to cause difficulty in laser welding, thus the welding process may require excessive heat input to overcome the reflection. The variation of welding speed is expected to have a great effect on the size and shape of the melt pool since the laser beam travels along a desired weld line with an increment of time step. Changes in welding speed induce more or less heat transfer rate into the 2D cross section, and the consequent heat diffusion through the model relates to the depth and the width of the melt pool.

The characteristics explained above are practical welding parameters conducting the formation of the melt pool, and the various applications of those parameters are provided in this welding study to verify the effects of parameter changes. The results will be graphically displayed using dimensionless parameters, e.g., Reynolds, Péclet, and Marangoni numbers [16, 60], as mathematically described in equations (3.18) through (3.20). The characteristic length L used in dimensionless numbers is assumed to be a radius of a laser beam [16]. Welding parameters used for the welding simulation are listed in Table 3.5.

$$Re = \frac{\rho V L}{\mu} \tag{3.18}$$

$$Pe = \frac{LV}{\alpha} = Re \cdot Pr \tag{3.19}$$

$$Ma = \frac{d\gamma}{dT} \cdot \frac{1}{\mu\alpha} \cdot L^2 \cdot \Delta T = \frac{d\gamma}{dT} \cdot \frac{1}{\mu\alpha} \cdot L^2 \cdot (T_s - T_\infty) \tag{3.20}$$

No.	Welding Parameter	Value
1	Welding speed	100 mm/s ~ 200 mm/s
2	Thickness of substrate	1.2 mm ~ 2.0 mm
3	Laser intensity	1×10^{10} W/m ~ 1×10^{11} W/m

Table 3.5 Welding parameters

Changes in welding parameters may require slight modification of the governing equations. If the thickness of the plate is less practical to generate fluid motion, a body force will be insignificant in the conservation law. However, the thicker the plate is, the body force becomes remarkable to obtain strong propulsion due to the restoring force of gravity or buoyance. The predictions of the excessive repulsion associated with the initial laser heat intensity are shown in Figure 3.14; a top-wide parabolic weld lined shape, a deep penetration shape (known as a key-hole) or an hour glass shaped melt pool. For the importance of the weight-driven effect, the body force can be added in conservation of linear momentum as a form of equation (3.21).

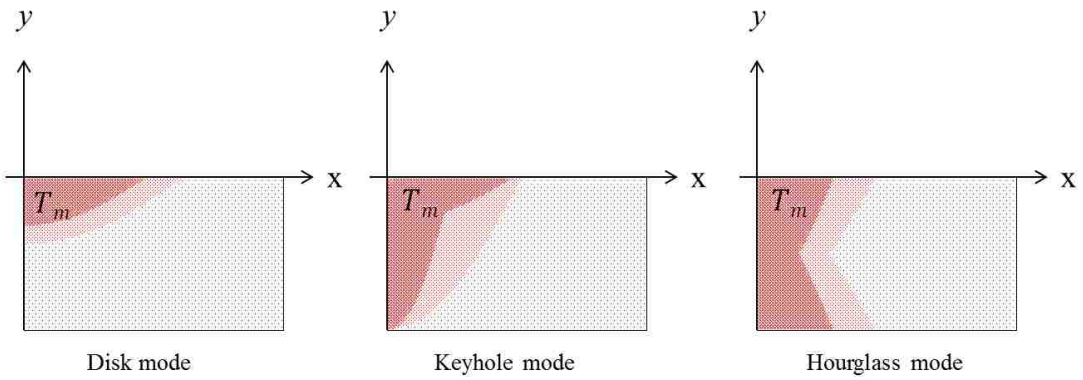

Figure 3.14 Predictions of weld pool shapes due to changes in welding parameters

$$F_b = \rho\beta(T - T_0)\vec{g} \tag{3.21}$$

β is the coefficient of thermal expansion, a function of temperature. $\vec{g}$ is the gravitational acceleration, but the gravitation is expected to have different signs. A negative sign will be given when the temperature of the molten material is in the range up to the melting point; a positive sign will be placed when the temperature is over the boiling point due to the direction of temperature dependent weight vector.

A pressure gradient in the conservation of momentum can be a dominant factor motivating the weld penetration if the laser plasma ejection is considerable by the increase of the laser intensity. Existence of an additional momentum input by the pressure becomes important evidence supporting how the weld elongates along the direction of the laser projection and dissipates heat more efficiently into the material. According to the pressure balance in the weld pool, an appropriate pressure equilibrium as shown in equation (3.23) is required to account for the fluid mechanism of the melt [61]. The pressure gradients with respect to x- and y-coordinates are expressed as in equation (3.24) assuming the molten material conducts slow viscous flow. Equation (3.24) is called Pressure-Poisson equation.

$$P_d + P_z \approx P_\gamma \tag{3.23}$$

$$\nabla P = \mu \nabla^2 \cdot \boldsymbol{V} = \begin{cases} \frac{\partial p}{\partial x} = \mu \left(\frac{\partial^2 u}{\partial x^2} + \frac{\partial^2 u}{\partial y^2} \right) \\ \frac{\partial p}{\partial y} = \mu \left(\frac{\partial^2 v}{\partial x^2} + \frac{\partial^2 v}{\partial y^2} \right) \end{cases} \tag{3.24}$$

where P_d is hydrodynamic pressure, P_z is pressure maintaining the weld penetration, and P_γ is pressure derived from the surface tension. P_d will be a function of fluid velocity in the melt pool, and P_z is assumed to be a function of plasma jet velocity from a initial laser intensity. However, P_z can be equivalent to vaporization pressure P_v in this laser welding research because P_v is the driven factor inducing the melt penetration. As the traditional form of laser heat flux follows Gaussian function, the laser recoil pressure may result in a form of the Gaussian distribution.

3.7 Thermal expansion induced Mechanical analysis

The 2D cross-section model was assumed to deform by thermal expansion or contraction when a base metal was heated or the melt cools down to the ambient temperature being in the solid phase. The thermal expansion of the model was of interest in this study since the result temperature profiles from the thermo-fluid analysis were sequentially employed to the structure analysis. If the welding deformation is restricted during the heating and cooling cycles, the stresses in the structure are increased due to the constraints. Therefore, thermal stresses were introduced in the structure analysis due to the heat induced thermal expansion of the material associated with the displacement constraints.

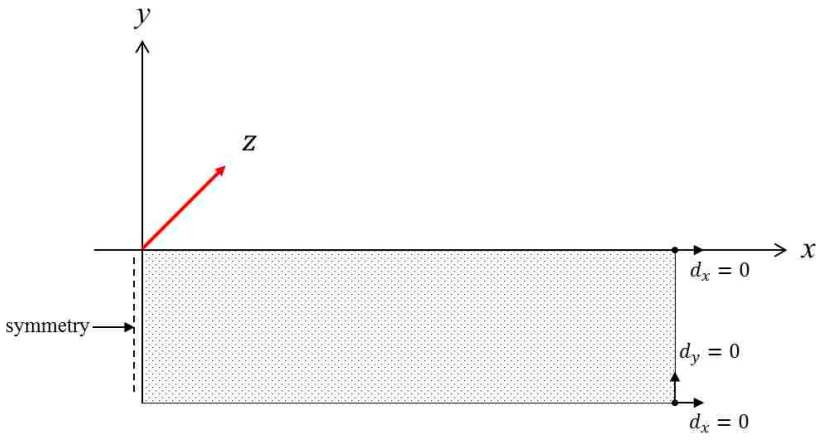

Figure 3.15 Boundary constraints for structure analysis

The structure analysis in welding was a study of thermal stresses resulting from an increase in internal stresses opposing to the deformation. The required clamping conditions for a laser welded plate were assumed to be simple displacement constraints due to the less distortion of laser welded products. Figure 3.15 shows the boundary constraints of the 2D cross-section model for the structure analysis. The system was a half of its full model, thus symmetry condition

was necessary for one side. The other side had to be responsible for less distortion since a free-to-move motion was mostly prohibited to reduce the welding deformation.

If a not-yet-melted material is assumed to be isotropic, the material exhibits an equivalent coefficient of the thermal expansion in all directions. Since the thermal expansion is because of an increase in temperature, the thermal stress which is proportional to the change in temperature can be expressed as the follows.

$$\varepsilon_t = \alpha_L(T - T_0) \tag{3.25}$$

$$\sigma_t = \varepsilon_t E = \alpha_L E(T - T_0) \tag{3.26}$$

where ε_t is thermal strain, α_L is the coefficient of linear thermal expansion, T_0 is the reference temperature related to the length of a material before thermal expansion occurs, σ_x is temperature induced thermal stress, and E is modulus of elasticity. Since a basic relation between stress and strain is derived from Hooke's law, most materials in the elastic region follow the expression as in equation (3.27).

$$\sigma_e = \varepsilon_e E \tag{3.27}$$

Plastic deformation of the weld also has a substantial influence on the increase in residual stresses because a metallic solid is often strengthened by plastic deformation during heating and cooling cycles. Plastic strain ε_p was therefore necessary to account for elevating residual stresses since work hardening was assumed to be in the solidification of the melt. The total strain rate can be finally written as the below, multi-linear isotropic hardening was used for the computation in ANSYS.

$$\varepsilon = \varepsilon_e + \varepsilon_t + \varepsilon_{\mathrm{p}} \tag{3.28}$$

Using the principle of virtual work, a virtual change of the internal strain energy is counterbalanced by an identical change in external work done by applied thermal load. The equivalent differential equation to be solved for displacements is as the follow.

$$M\ddot{U} + KU = P \tag{3.29}$$

$$M = \int_A \rho[N]^T[N]dA \tag{3.30}$$

$$K = \int_A [B]^T[D][B]dA \tag{3.31}$$

$$P = \int_A [B]^T[D]\{\varepsilon\}dA \tag{3.32}$$

where Mstands for the mass matrix, K is the stiffness matrix, and P denotes the external force or the load transferred from the thermo-fluid analysis. If the effect of mass is negligible, the final relation results in as the below.

$$KU = P \tag{3.33}$$

where U is a displacement vector. Numerical methods, e.g., Newton-Raphson iteration, are used for solving the nonlinear system of equation (3.33). The mechanical analysis is performed using a mechanism relevant to thermal expansion, and the stress distributions are investigated by the of Von-Mises criterion. The residual stresses and the resulting distortions are associated with the magnitude and extent of laser heat induced thermoplastic deformation. The prediction of the stress distribution is highly dependent on the accuracy of the results from thermo-fluid analysis due to the temperature dependency of the yielding behavior.

Chapter 4 Differential equations used in thermo-fluid analysis

4.1 Conservation of thermal energy

For the F. E. based numerical computation, a two dimensional thermal system is employed with a laser moving heat source. As Fourier's law is the first principle to describe heat conduction rate through the system, the expression is accountable for conductive thermal energy transfer in this laser welding process. One directional heat conduction rate is given as a function of the temperature gradient as shown in equation (4.1). Assuming that the proposed 2D system is an isotropic model, basic conservation of energy in the 2D Cartesian coordinates can be derived as equation (4.2).

$$q_x = -k\left(\frac{\partial T}{\partial x}\right) \tag{4.1}$$

$$\frac{\partial}{\partial x}\left(k\frac{\partial T}{\partial x}\right) + \frac{\partial}{\partial y}\left(k\frac{\partial T}{\partial y}\right) + Q = \rho c_p \frac{\partial T}{\partial t} \tag{4.2}$$

The time dependent term of equation (4.2) can be removed when the numerical algorithm needs a solution of a steady-state welding process. Simplifying the 2D thermal system, the transient term in equation (4.1) is removed, and the governing equation is reduced to the linear differential form of equation (4.3).

$$\frac{\partial}{\partial x}\left(k\frac{\partial T}{\partial x}\right) + \frac{\partial}{\partial y}\left(k\frac{\partial T}{\partial y}\right) + Q = 0 \tag{4.3}$$

If we restrict the degree of freedom of the system, the types of boundary conditions can possibly be as the follows:

1) Fixed temperature (point, surface, volume)

$$T = T_1(x, y, t) \tag{4.4}$$

2) Specified heat flux (surface)

$$k\frac{\partial T}{\partial x}n_x + k\frac{\partial T}{\partial y}n_y = -q \tag{4.5}$$

3) Convection (surface)

$$k\frac{\partial T}{\partial x}n_x + k\frac{\partial T}{\partial y}n_y = -h(T - T_0) \tag{4.6}$$

4) Radiation (surface)

$$k\frac{\partial T}{\partial x}n_x + k\frac{\partial T}{\partial y}n_y = -h_r(T - T_0) \tag{4.7}$$

Through equations (4.5) to (4.7), the "negative" sign means that heat is leaving from the thermal system to outside. According to the given geometries as in Figure 4.1, the boundary conditions for this study are the combination of equation (4.6) and (4.7) on the surface where it is exposed to the ambient air temperature T_0.

$$k\frac{\partial T}{\partial x}n_x + k\frac{\partial T}{\partial y}n_y = -h(T - T_0) - h_r(T - T_0) \tag{4.8}$$

where $\{n\} = \begin{Bmatrix} n_x \\ n_y \end{Bmatrix}$ is a normal vector which is normal to the surface where the heat flows through.

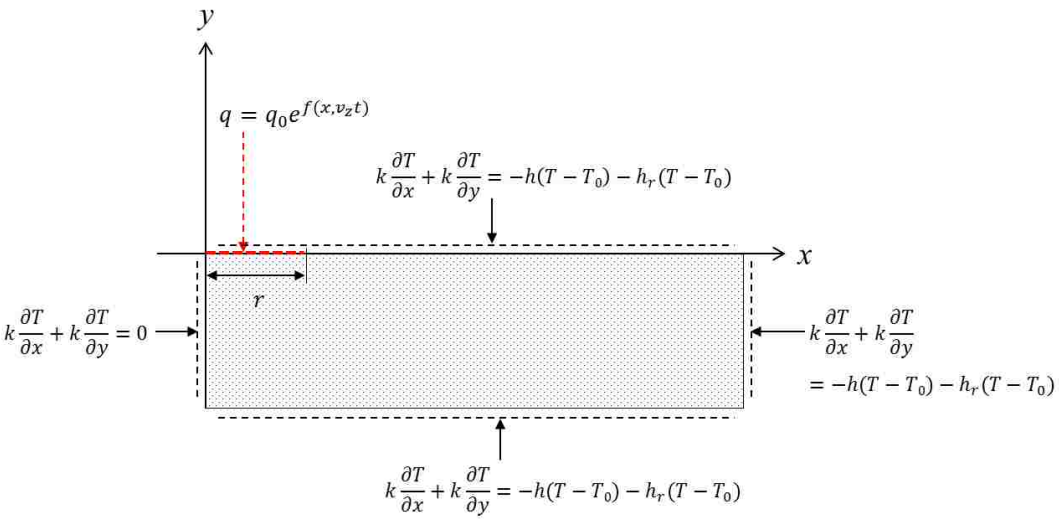

Figure 4.1 Boundary condition of the thermal system

4.2 Conservation of mass and linear momentum in fluid

A melt is assumed to be an incompressible viscous Newtonian fluid in this laser welding research. Therefore, "mass flow rate" which is defined as the amount of mass flowing through a control surface per unit time is firstly concerned to measure the effect of the melt flow through the control volume in the 2D system. Mass flow in an infinitesimal control volume is described in Figure 4.2 and the rate is defined as the below where $\boldsymbol{V} = u\hat{\imath} + v\hat{\jmath}$ in 2D Cartesian coordinates.

$$\dot{M} = \int_C \ \rho \boldsymbol{V} \cdot ds \tag{4.9}$$

The left hand side of equation (4.9) can be expressed as the below.

$$\dot{M} = \frac{\partial \rho}{\partial t} dxdy \tag{4.10}$$

If we derive the net of mass flow rate through the control volume in a form of its derivatives,

$$\begin{aligned}\int_C \ \rho \boldsymbol{V} \cdot ds \ &= \left[\left(\rho - \frac{\partial \rho}{\partial x}\frac{dx}{2}\right)\left(u - \frac{\partial u}{\partial x}\frac{dx}{2}\right) - \left(\rho + \frac{\partial \rho}{\partial x}\frac{dx}{2}\right)\left(u + \frac{\partial u}{\partial x}\frac{dx}{2}\right)\right] dy \\ &\quad + \left[\left(\rho - \frac{\partial \rho}{\partial y}\frac{dy}{2}\right)\left(v - \frac{\partial v}{\partial y}\frac{dy}{2}\right) - \left(\rho + \frac{\partial \rho}{\partial y}\frac{dy}{2}\right)\left(v + \frac{\partial v}{\partial y}\frac{dy}{2}\right)\right] dx \\ &= -\left(\rho \frac{\partial u}{\partial x} + \frac{\partial \rho}{\partial x} u\right) dxdy - \left(\rho \frac{\partial v}{\partial y} + \frac{\partial \rho}{\partial y} v\right) dxdy \\ &= -(\rho \nabla \cdot \boldsymbol{V} + \nabla \rho \cdot \boldsymbol{V}) dxdy \end{aligned} \tag{4.11}$$

By the use of chain rule, we can utilize the relation of $\nabla \cdot \rho \boldsymbol{V} = \nabla \rho \cdot \boldsymbol{V} + \rho(\nabla \cdot \boldsymbol{V})$.

Finally, the mass flux passing through the control volume is defined as the below.

$$\int_C \ \rho \boldsymbol{V} \cdot ds \ = -\left(\frac{\partial \rho u}{\partial x} + \frac{\partial \rho v}{\partial y}\right) dxdy \tag{4.12}$$

If we rearrange the expressions and cancel out $dxdy$ in equation (4.10),

$$\frac{\partial \rho}{\partial t} + \frac{\partial \rho u}{\partial x} + \frac{\partial \rho v}{\partial y} = 0 \tag{4.13}$$

If a fluid is incompressible, density change in time should follow the relation of $\frac{\partial \rho}{\partial t} = 0$. This represents the density is constant over the time period; therefore, the incompressibility finally results in equation (4.14).

$$\frac{\partial u}{\partial x} + \frac{\partial v}{\partial y} = \nabla \cdot \boldsymbol{V} = 0 \tag{4.14}$$

Similarly, final expressions of linear momentums incompressible viscous Newtonian fluid in 2D Cartesian coordinates are expressed as the follows.

$$u\frac{\partial u}{\partial x} + v\frac{\partial u}{\partial y} + \frac{\partial u}{\partial t} = g_x - \frac{1}{\rho}\frac{\partial p}{\partial x} + \frac{\mu}{\rho}\left(\frac{\partial^2 u}{\partial x^2} + \frac{\partial^2 u}{\partial y^2}\right) \tag{4.15}$$

$$u\frac{\partial v}{\partial x} + v\frac{\partial v}{\partial y} + \frac{\partial v}{\partial t} = g_y - \frac{1}{\rho}\frac{\partial p}{\partial y} + \frac{\mu}{\rho}\left(\frac{\partial^2 v}{\partial x^2} + \frac{\partial^2 v}{\partial y^2}\right) \tag{4.16}$$

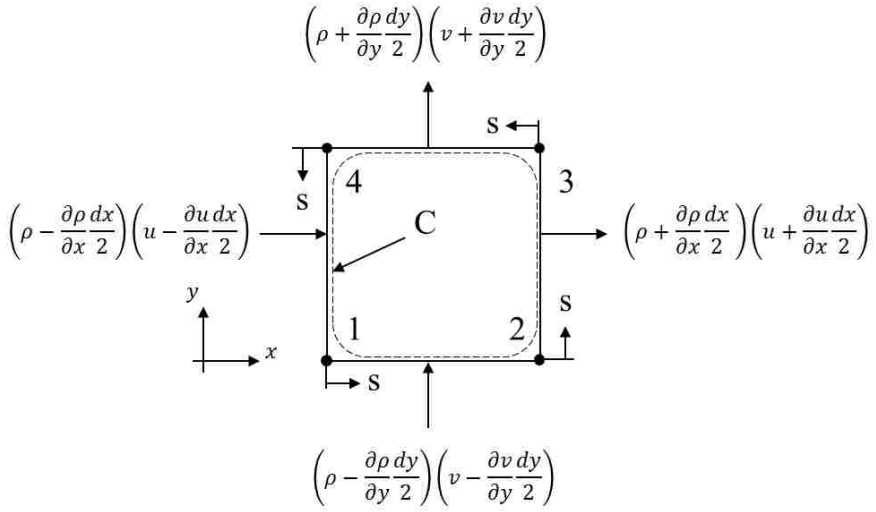

Figure 4.2 Control volume in Cartesian coordinates

4.3 Viscous dissipation and viscous work in Newtonian fluid

As shown in Figure 4.3, the sum of work done by normal stress components applied to the 2D control volume can be expressed as the follows.

$$\begin{aligned}
&\int_C \ \sigma_n \boldsymbol{V} \cdot ds \\
&= \left[\left(\sigma_{xx} + \frac{\partial \sigma_{xx}}{\partial x}\frac{dx}{2}\right)\left(u + \frac{\partial u}{\partial x}\frac{dx}{2}\right) - \left(\sigma_{xx} - \frac{\partial \sigma_{xx}}{\partial x}\frac{dx}{2}\right)\left(u - \frac{\partial u}{\partial x}\frac{dx}{2}\right)\right] dy \\
&\quad + \left[\left(\sigma_{yy} + \frac{\partial \sigma_{yy}}{\partial y}\frac{dy}{2}\right)\left(v + \frac{\partial v}{\partial y}\frac{dy}{2}\right) - \left(\sigma_{yy} - \frac{\partial \sigma_{yy}}{\partial y}\frac{dy}{2}\right)\left(v - \frac{\partial v}{\partial y}\frac{dy}{2}\right)\right] dx \\
&= \left(\frac{\partial \sigma_{xx}}{\partial x}u + \sigma_{xx}\frac{\partial u}{\partial x}\right) dxdy + \left(\frac{\partial \sigma_{yy}}{\partial y}v + \sigma_{yy}\frac{\partial v}{\partial y}\right) dxdy \qquad (4.17)
\end{aligned}$$

If the viscous stress is proportional to the rate of shearing strain in Newtonian fluid, this will follow the basic rules listed below where δ is given as a Kronecker-delta function and i and j vary from 1 to 2 in 2D Cartesian coordinates. μ is the viscosity of fluid and λ is the second viscosity coefficient which will be given if required.

1) δ_{ij}: $\delta_{11} = \delta_{22} = 1, e_{ij} = \frac{1}{2}\gamma_{ij}$

2) $\sigma_{ij} = (-p + \lambda \nabla \cdot \boldsymbol{V})\delta_{ij} + 2\mu e_{ij}$

3) $e_{ij} = \frac{1}{2}\left(\frac{\partial V_i}{\partial X_j} + \frac{\partial V_j}{\partial X_i}\right)$

The normal stress equations for an incompressible Newtonian fluid are given as the follows.

$$\sigma_{xx} = -p + \lambda \nabla \cdot \boldsymbol{V} + 2\mu e_{xx} = -p + 2\mu \frac{\partial u}{\partial x} \qquad (4.18)$$

$$\sigma_{yy} = -p + \lambda \nabla \cdot \boldsymbol{V} + 2\mu e_{yy} = -p + 2\mu \frac{\partial v}{\partial y} \qquad (4.19)$$

$$\begin{aligned}
&\int_C \ \sigma_n \boldsymbol{V} \cdot ds \ = \left[\sigma_{xx}\frac{\partial u}{\partial x} + \sigma_{yy}\frac{\partial v}{\partial y} + u\frac{\partial \sigma_{xx}}{\partial x} + v\frac{\partial \sigma_{yy}}{\partial y}\right] dxdy \\
&= \left\{\left[-p + 2\mu\frac{\partial u}{\partial x} + \lambda\nabla \cdot \boldsymbol{V}\right]\frac{\partial u}{\partial x} + \left[-p + 2\mu\frac{\partial v}{\partial y} + \lambda\nabla \cdot \boldsymbol{V}\right]\frac{\partial v}{\partial y}\right.
\end{aligned}$$

$$+u\left[-\frac{\partial p}{\partial x}+\frac{\partial}{\partial x}\left(\lambda\,\nabla\cdot\boldsymbol{V}+2\mu\frac{\partial u}{\partial x}\right)\right]+v\left[-\frac{\partial p}{\partial y}+\frac{\partial}{\partial y}\left(\lambda\,\nabla\cdot\boldsymbol{V}+2\mu\frac{\partial v}{\partial y}\right)\right]\Big\}dxdy$$

$$=\left\{-p\left(\frac{\partial u}{\partial x}+\frac{\partial v}{\partial y}\right)+2\mu\left[\left(\frac{\partial u}{\partial x}\right)^2+\left(\frac{\partial v}{\partial y}\right)^2+\lambda\nabla\cdot\boldsymbol{V}\left(\frac{\partial u}{\partial x}+\frac{\partial v}{\partial y}\right)\right]\right.$$

$$\left.-\left(u\frac{\partial p}{\partial x}+v\frac{\partial p}{\partial y}\right)+2\mu\left(\frac{\partial^2 u}{\partial x^2}+\frac{\partial^2 v}{\partial y^2}\right)+\lambda\left(u\frac{\partial}{\partial x}\nabla\cdot\boldsymbol{V}+v\frac{\partial}{\partial y}\nabla\cdot\boldsymbol{V}\right)\right\}dxdy$$

$$=\left\{-p(\nabla\cdot\boldsymbol{V})+2\mu\left[\left(\frac{\partial u}{\partial x}\right)^2+\left(\frac{\partial v}{\partial y}\right)^2\right]+\lambda(\nabla\cdot\boldsymbol{V})^2\right.$$

$$\left.-(\boldsymbol{V}\cdot\nabla p)+2\mu(\nabla^2\cdot\boldsymbol{V})+\lambda[\boldsymbol{V}\cdot\nabla(\nabla\cdot\boldsymbol{V})]\right\}dxdy \qquad (4.20)$$

Incompressible satisfies the relation of $\nabla\cdot\boldsymbol{V}=0$; therefore, the fluid work which is normal to the control volume surface can be finally written as the below.

$$\int_C \sigma_n\,\boldsymbol{V}\cdot ds = 2\mu\left[\left(\frac{\partial u}{\partial x}\right)^2+\left(\frac{\partial v}{\partial y}\right)^2\right]dxdy \qquad (4.21)$$

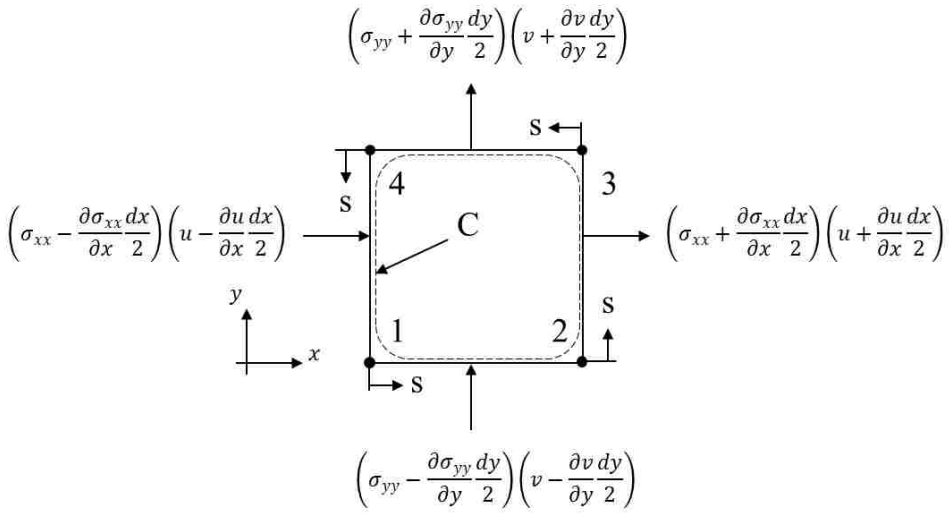

Figure 4.3 Schematic diagram of normal stress components applied to control volume

As shown in Figure 4.4, the net work done by shear stresses is given as the follows.

$$\int_C \boldsymbol{\tau} \cdot \boldsymbol{V}\, ds$$

$$= \left[\left(\tau_{xy} + \frac{\partial \tau_{xy}}{\partial x}\frac{dx}{2}\right)\left(v + \frac{\partial v}{\partial x}\frac{dx}{2}\right) - \left(\tau_{xy} - \frac{\partial \tau_{xy}}{\partial x}\frac{dx}{2}\right)\left(v - \frac{\partial v}{\partial x}\frac{dx}{2}\right)\right] dy$$

$$+ \left[\left(\tau_{yx} + \frac{\partial \tau_{yx}}{\partial y}\frac{dy}{2}\right)\left(u + \frac{\partial u}{\partial y}\frac{dy}{2}\right) - \left(\tau_{yx} - \frac{\partial \tau_{yx}}{\partial y}\frac{dy}{2}\right)\left(u - \frac{\partial u}{\partial y}\frac{dy}{2}\right)\right] dx$$

$$= \left(\frac{\partial \tau_{xy}}{\partial x} v + \tau_{xy}\frac{\partial v}{\partial x}\right) dxdy + \left(\frac{\partial \tau_{yx}}{\partial y} u + \tau_{yx}\frac{\partial u}{\partial y}\right) dxdy \quad (4.22)$$

Using the definition given in equation (4.22), the shear stress in Newtonian viscous flow can be defined as the follows.

$$\tau_{xy} = \mu\left(\frac{\partial v}{\partial x} + \frac{\partial u}{\partial y}\right) = \tau_{yx} \quad (4.23)$$

$$\int_C \boldsymbol{\tau} \cdot \boldsymbol{V}\, ds = \left(\tau_{xy}\frac{\partial v}{\partial x} + \tau_{yx}\frac{\partial u}{\partial y} + \frac{\partial \tau_{xy}}{\partial x} v + \frac{\partial \tau_{yx}}{\partial y} u\right) dxdy$$

$$= \mu\left[\left(\frac{\partial v}{\partial x} + \frac{\partial u}{\partial y}\right)\frac{\partial v}{\partial x} + \left(\frac{\partial v}{\partial x} + \frac{\partial u}{\partial y}\right)\frac{\partial u}{\partial y}\right] dxdy$$

$$+ \left[\frac{\partial}{\partial x}\mu\left(\frac{\partial v}{\partial x} + \frac{\partial u}{\partial y}\right) v + \frac{\partial}{\partial y}\mu\left(\frac{\partial v}{\partial x} + \frac{\partial u}{\partial y}\right) u\right] dxdy \quad (4.24)$$

1) The first term on the right hand side in equation (4.24) yields the relation as the below.

$$= \mu\left[\left(\frac{\partial v}{\partial x} + \frac{\partial u}{\partial y}\right)\frac{\partial v}{\partial x} + \left(\frac{\partial v}{\partial x} + \frac{\partial u}{\partial y}\right)\frac{\partial u}{\partial y}\right] dxdy = \mu\left(\frac{\partial v}{\partial x} + \frac{\partial u}{\partial y}\right)^2 dxdy$$

$$= \mu \sum_i \sum_j \left(\frac{\partial V_j}{\partial X_i} + \frac{\partial V_i}{\partial X_j}\right)^2 dxdy \quad (4.25)$$

2) The second term on the right hand side in equation (4.24) yields the relation as the below.

$$= \mu\left[\frac{\partial}{\partial x}\left(\frac{\partial v}{\partial x} + \frac{\partial u}{\partial y}\right) v + \frac{\partial}{\partial y}\left(\frac{\partial v}{\partial x} + \frac{\partial u}{\partial y}\right) u\right] dxdy$$

$$= \mu \sum_i \sum_j \frac{\partial}{\partial X_i}\left(\frac{\partial V_j}{\partial X_i} + \frac{\partial V_i}{\partial X_j}\right) V_j\, dxdy \quad (4.26)$$

All fluid work due to the normal and shear stresses applied to the control volume can be arranged as the follows where i and j satisfy the relation of $i \neq j$ and $i, j = x, y$

$$\int_C \sigma_n \boldsymbol{V} \cdot ds + \int_C \boldsymbol{\tau} \cdot \boldsymbol{V}\, ds$$

$$= \left\{ 2\mu \left[\left(\frac{\partial u}{\partial x}\right)^2 + \left(\frac{\partial v}{\partial y}\right)^2 \right] \right.$$

$$\left. + \mu \sum_i \sum_j \left(\frac{\partial V_j}{\partial X_i} + \frac{\partial V_i}{\partial X_j} \right)^2 + \mu \sum_i \sum_j \frac{\partial}{\partial X_i} \left(\frac{\partial V_j}{\partial X_i} + \frac{\partial V_i}{\partial X_j} \right) V_j \right\} dxdy \tag{4.27}$$

Finally, the viscous fluid work terms are defined as the follows.

1) Viscous dissipation

$$\mu\Phi = -\mu \left[2 \sum_i \left(\frac{\partial V_i}{\partial X_i} \right)^2 + \sum_i \sum_j \left(\frac{\partial V_j}{\partial X_i} + \frac{\partial V_i}{\partial X_j} \right)^2 \right] dxdy \tag{4.28}$$

2) Viscous work

$$\dot{W}_{vis} = -\mu \sum_i \sum_j \frac{\partial}{\partial X_i} \left(\frac{\partial V_j}{\partial X_i} + \frac{\partial V_i}{\partial X_j} \right) V_j \; dxdy \tag{4.29}$$

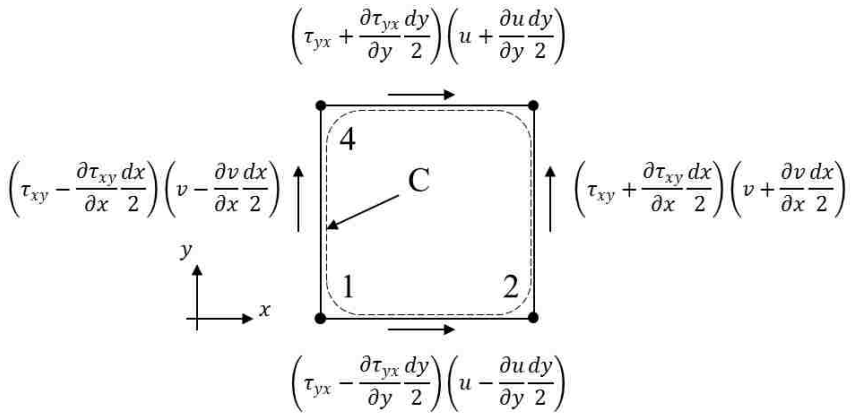

Figure 4.4 Schematic diagram of shear stress components applied to control volume

4.4 System governing equations influenced by fluid flow

If heat transfer rate is influenced by fluid flow in 2D thermal system, conservation of thermal energy should include a certain amount of work done by the system against fluid flow as the given below.

$$\dot{E} = \dot{Q} - \dot{W} \tag{4.30}$$

$\dot{E}$ is the sum of the net transfer of energy by fluid flow and the rate of energy stored in the system. $\dot{Q}$ is the sum of the net heat transfer by conduction and the rate of heat generation, $\dot{W}$ is the net work done by the system,. The rate of work can be equivalent to the sum of shaft, normal, shear, and other work. Assuming that shaft and other work are negligible, the total work done by the system results in the sum of the normal and shear work as in equation (4.31).

$$\dot{W} = \int_C \ \sigma_n \boldsymbol{V}\, ds \ + \int_C \ \boldsymbol{\tau} \cdot \boldsymbol{V}\, ds \ = \mu\Phi + \dot{W}_{vis} \tag{4.31}$$

$\dot{E}$ can be re-expressed assuming that there are moving particles in the fluid, and the details are described as the below.

$$\dot{E} = \frac{dE}{dt} = \frac{\partial}{\partial t}\int_A \ \rho e\, dA \ + \int_C \ \rho e\, \boldsymbol{V}\, ds \tag{4.32}$$

The first term on the right hand side can be rearranged using the definition of enthalpy $h = e + pv = e + \frac{p}{\rho}$ and the relation of $\frac{Dp}{Dt} = u\frac{\partial p}{\partial x} + v\frac{\partial p}{\partial y} + \frac{\partial p}{\partial t}$.

$$\begin{aligned}
\frac{\partial}{\partial t}\int_A \ \rho e\, dA \ &= \frac{\partial(\rho e)}{\partial t}\, dxdy = \frac{\partial}{\partial t}\left(\rho\left(h - \frac{p}{\rho}\right)\right) dxdy \\
&= \frac{\partial(\rho h)}{\partial t}\, dxdy - \frac{\partial p}{\partial t}\, dxdy \\
&= \frac{\partial(\rho h)}{\partial t}\, dxdy - \left[\frac{Dp}{Dt} - \left(u\frac{\partial p}{\partial x} + v\frac{\partial p}{\partial y}\right)\right] dxdy \\
&= \frac{\partial(\rho h)}{\partial t}\, dxdy - \frac{Dp}{Dt}\, dxdy + (\boldsymbol{V} \cdot \nabla p) dxdy
\end{aligned} \tag{4.33}$$

As a result of that,

$$\dot{E} = \frac{\partial}{\partial t}\int_A \rho e \, dA + \int_C \rho e \, \boldsymbol{V} \, ds$$

$$= \frac{\partial(\rho h)}{\partial t} dxdy - \frac{Dp}{Dt} dxdy + \left[(\boldsymbol{V} \cdot \nabla p) dxdy + \int_C \rho e \, \boldsymbol{V} \, ds \right] \quad (4.34)$$

In order to arrange the second term in the "[ ]", the relation of equation (4.35) must be used.

$$\int_C p\boldsymbol{V} ds = \left[\left(p + \frac{\partial p}{\partial x}\frac{dx}{2} \right) \left(u + \frac{\partial u}{\partial x}\frac{dx}{2} \right) - \left(p - \frac{\partial p}{\partial x}\frac{dx}{2} \right) \left(u - \frac{\partial u}{\partial x}\frac{dx}{2} \right) \right] dy$$

$$+ \left[\left(p + \frac{\partial p}{\partial y}\frac{dy}{2} \right) \left(v + \frac{\partial v}{\partial y}\frac{dy}{2} \right) - \left(p - \frac{\partial p}{\partial y}\frac{dy}{2} \right) \left(v - \frac{\partial v}{\partial y}\frac{dy}{2} \right) \right] dx$$

$$= \left(p\frac{\partial u}{\partial x} + \frac{\partial p}{\partial x}u \right) dxdy + \left(p\frac{\partial v}{\partial y} + \frac{\partial p}{\partial y}v \right) dxdy$$

$$= p(\nabla \cdot \boldsymbol{V}) dxdy + (\nabla p \cdot \boldsymbol{V}) dxdy \quad (4.35)$$

By the relation of $\nabla \cdot \boldsymbol{V} = 0$ for incompressible flow, equation (4.35) is expressed as the below.

$$\int_C p\boldsymbol{V} ds = \left(u\frac{\partial p}{\partial x} + v\frac{\partial p}{\partial y} \right) dxdy = (\boldsymbol{V} \cdot \nabla p) dxdy \quad (4.36)$$

Therefore, the second term in equation (4.34) can be replaced using equation (4.36).

$$\left[(\boldsymbol{V} \cdot \nabla p) dxdy + \int_C \rho e \, \boldsymbol{V} \, ds \right] = \int_C p\boldsymbol{V} ds + \int_C \rho e \, \boldsymbol{V} \, ds$$

$$= \int_C p\boldsymbol{V} ds + \int_C \rho \left(h - \frac{p}{\rho} \right) \boldsymbol{V} \, ds$$

$$= \int_S \rho h \, \boldsymbol{V} \, ds \quad (4.37)$$

If we consider the change in enthalpy through the control volume,

$$\int_S h \, \boldsymbol{V} \, ds$$

$$= \left[\left(\rho h + \frac{\partial \rho h}{\partial x}\frac{dx}{2} \right) \left(u + \frac{\partial u}{\partial x}\frac{dx}{2} \right) - \left(\rho h - \frac{\partial \rho h}{\partial x}\frac{dx}{2} \right) \left(u - \frac{\partial u}{\partial x}\frac{dx}{2} \right) \right] dy$$

$$+ \left[\left(\rho h + \frac{\partial \rho h}{\partial y}\frac{dy}{2} \right) \left(v + \frac{\partial v}{\partial y}\frac{dy}{2} \right) - \left(\rho h - \frac{\partial \rho h}{\partial y}\frac{dy}{2} \right) \left(v - \frac{\partial v}{\partial y}\frac{dy}{2} \right) \right] dx$$

$$= \left(\rho h\frac{\partial u}{\partial x} + \frac{\partial \rho h}{\partial x}u \right) dxdy + \left(\rho h\frac{\partial v}{\partial y} + \frac{\partial \rho h}{\partial y}v \right) dxdy \quad (4.38)$$

If we combine all equations from (4.34) to (4.38) and rearrange them,

$$\dot{E} = \frac{\partial}{\partial t}\int_A \rho e\, dA + \int_C \rho e\, \boldsymbol{V}\, ds$$

$$= \frac{\partial(\rho h)}{\partial t} dxdy - \frac{Dp}{Dt} dxdy + \left(\rho h \frac{\partial u}{\partial x} + \frac{\partial \rho h}{\partial x} u\right) dxdy + \left(\rho h \frac{\partial v}{\partial y} + \frac{\partial \rho h}{\partial y} v\right) dxdy$$

$$= \left[\frac{\partial \rho h}{\partial x} u + \frac{\partial \rho h}{\partial y} v + \frac{\partial(\rho h)}{\partial t}\right] dxdy - \frac{Dp}{Dt} dxdy + \rho h \left(\frac{\partial u}{\partial x} + \frac{\partial v}{\partial y}\right) dxdy$$

$$= \left\{\frac{D\rho h}{Dt} - \frac{Dp}{Dt}\right\} dxdy \quad (4.39)$$

Finally, conservation of energy in fluid is expressed as the follows.

$$\dot{E} = \dot{Q} - \dot{W}$$

$$\frac{D\rho h}{Dt} dxdy = \frac{Dp}{Dt} dxdy + \dot{Q} + \mu\Phi + \dot{W}_{vis} \quad (4.40)$$

1) $\dot{Q}$ in equation (4.40) is the sum of the net heat conduction and heat generation.

$$\dot{Q} = \dot{E}_k + \dot{E}_g \quad (4.41)$$

2) $\dot{E}_k$, the rate of total conduction rate through the system, and can be expressed as the below using Fourier's law. $\dot{E}_g$ is the applied heat generation rate.

$$\dot{E}_k = \left(q_x + q_y\right) - \left(q_{x+dx} + q_{y+dy}\right) = -\left(\frac{dq_x}{dx} dx + \frac{dq_y}{dy} dy\right)$$

$$= \left[\frac{\partial}{\partial x}\left(k \frac{\partial T}{\partial x}\right) + \frac{\partial}{\partial y}\left(k \frac{\partial T}{\partial y}\right)\right] dxdy = k\left(\frac{\partial^2 T}{\partial x^2} + \frac{\partial^2 T}{\partial y^2}\right) dxdy \quad (4.42)$$

$$\dot{E}_g = \dot{q} dxdy \quad (4.43)$$

Chapter 5 Effect of melt dynamics

5.1 Laser welding process modeling

The prior material selection was used to investigate the effect of generalized welding parameters relevant to the thermo-fluid mechanism during this laser welding study. Eliminating the metallurgical difficulties associated with most alloys, the determined material properties had an advantage of full concentration on how the molten material flow influenced the formation of the melt pool. Briefly, the fundamental studies on the melt pool heat transfer mechanism were useful for understanding how fluid circulation was related to the weld pool shape and the evolving residual stresses.

The effect of thermal energy transfer in fluid was investigated using a simple 2D plane in ANSYS. The 2D model was very small since the laser was assumed to target on a small spot with the radius of 0.4 mm. The geometries for the 2D cross-section model were a length of 10 mm and a height of 1.2 mm as shown in Figure 5.1. The height was the thickness of the plate, and it varied from 1.2 mm to 2.0 mm according to the laser heat intensity. A fast mode simulation showed that a thin plate exhibited the melt penetration with relatively low laser intensity, but the thicker plate required higher laser power to observe the melt penetration.

In order to increase the simulation accuracy, the elements around melt penetration had extremely fine mesh, a size of 0.4 μm, which was 10 times smaller than the radius of the laser beam. The infinitesimal meshing sizes in Figure 5.2 were extended to the melting areas and expected heat affected zone (HAZ). The HAZ was assumed to be within a horizontal distance of 2 mm away from the heat source center.

The laser heat source was assumed to have its pass normal to the cross-section model. The heat source was given as a function of time to simulate the transient moving heat source, and

the intensity varied by the heat distribution factor m. The welding simulations resulted in that the melt formed a wide pool with no penetration if $m < 1$. Moreover, much higher laser intensity was necessary to yield melt penetration if $m > 1$ due to the concentration of the heat density only at the core of the laser beam. The factor was proportional to the depth of the melt pool; however, the influence was unstable and it could be replaced by the proper control of heat intensity. As a result, the variation of m seemed not important to the pool formation, and several fast-run simulations were optimized well with $m = 1$ for the melt penetration.

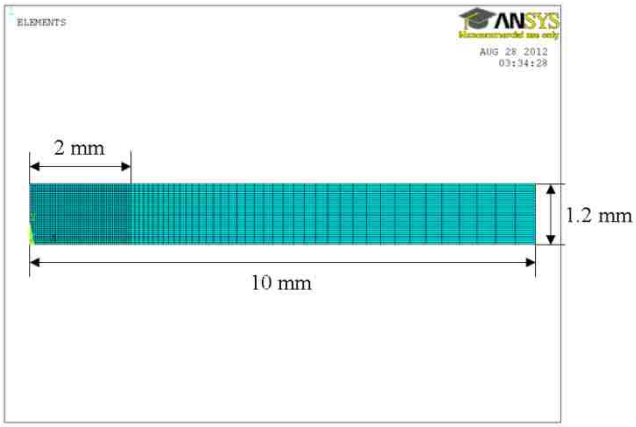

Figure 5.1 Finite element mesh for 2D cross-section model

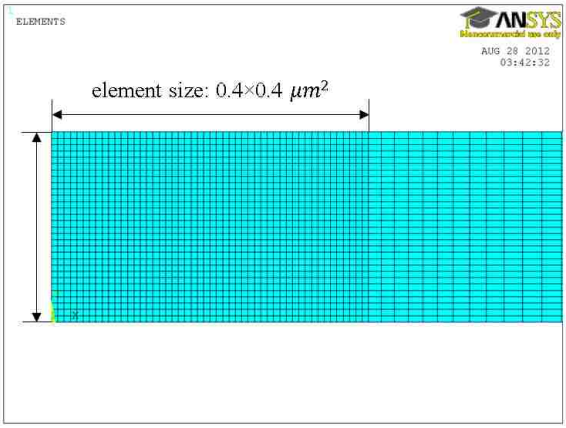

Figure 5.2 Application of fine meshing around the area where melt penetration was expected

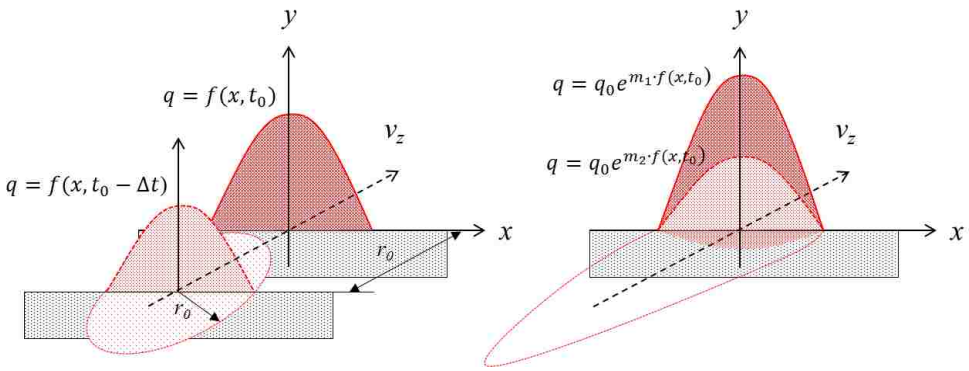

Figure 5.3 Moving heat source along the weld line

On the other hand, the proposed heat source models, e.g., a heat source with multiple error functions and constant value, described in the earlier chapter also exhibited instability similar to the use of the variable distribution factors. Therefore, the research was based on the Gaussian heat distribution model with the distribution factor $m = 1$ for the heat source modeling.

An effect of heat approaching to or leaving the cross-section was expected in the boundary of laser heat source model as in Figure 5.3 since the original disk heat density function had a circular distribution of heat on the x-z plane. As a result, the second term in the exponential of equation (5.1) was properly modified to be adequate to the heat source moving.

$$\dot{q} = q_0 \cdot \exp\left[-\left(\frac{x^2}{r_0^2}\right)\right] \cdot \exp\left[-\left(\frac{(v_z t - r_0)^2}{r_0^2}\right)\right] \qquad (5.1)$$

The welding simulation results were arranged in relation to the formation of the hourglass mode. A criterion for evaluating simulation results was recommended to compare one with other sets of simulation results. The selected criterion was a simulation done on the plate thickness of 1.2 mm with the laser intensity of 3.58×10^{10} W/m^2 since the diversification of the pool formation was uncertain to clearly explain what was the critical factor to determine its shape due to the combined effects of the welding parameters, e.g., heat intensity and welding velocity.

5.2 Hourglass mode welding

It was first assumed that the effects of surface tension and recoil pressure resulted in the formation of deep melt penetration towards the opposite side of the base metal. The first trial was made based on the following welding parameters:

1) Laser intensity of 3.58×10^{10} W/m^2

2) Welding velocity of 100 mm/s

The shape of the melt pool after penetration is shown in Figure 5.4. The molten iron forms a top and bottom wide melt pool due to the effect of surface tension on the both top and bottom melt surface layers. With the laser intensity of 3.58×10^{10} W/m^2, the shape of the melt pool was vertically well-balanced when comparing the widths of the top and bottom layers. In Figure 5.4, the area in red is in the liquid phase, and the temperatures are in the range between the melting and boiling points of pure iron. This red colored region represents an expected final weld shape after the melt cools down to room temperature.

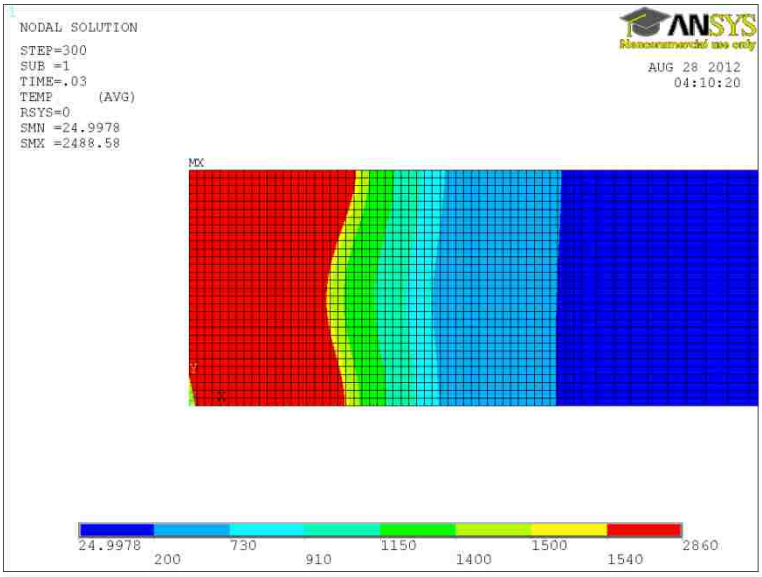

Figure 5.4 Temperature distribution of hourglass: intensity of 3.58×10^{10} W/m^2 and velocity of 100 mm/s

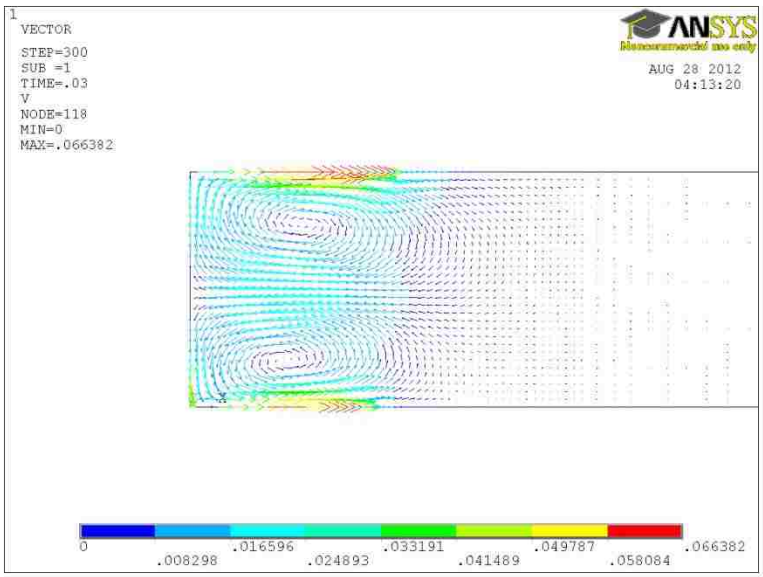

Figure 5.5 Velocity profile of hourglass mode with laser intensity of 3.58×10^{10} W/m^2 and welding velocity of 100 mm/s

Figure 5.5 is the velocity profile relevant to the temperature distribution of Figure 5.4. The maximum velocities of 0.066 m/s were observed at the both top and bottom surface layers, and the use of Reynold's analogy, $Re = \frac{\rho V r_0}{\mu}$, provided a dimensionless number of 42.6. Since the surface tension widens the pool pulling the melt outwards, its dynamics have resulted in hourglass welding mode. The areas in blue, which are of circular pattern in Figure 5.5, represent immobility of the melt, and the melt is assumed to be stagnant due to the counter balance of the two separate major circulation paths from the top and bottom flows. In the right hand side of Figure 5.5, which is all in blue, it is assumed that the iron is not yet melted; therefore, the region exhibits no fluid flow.

A transient result during melt penetration is shown in Figure 5.6. The area in grey is the iron in the gas phase, and the downward velocities evidence the existence of recoil pressure. The

recoil pressure promotes the melts to drill the way downward, and the velocity at the melt front has the maximum of 0.0797 m/s. The evaporation of the melt is responsible for the excessive pressure work along the path of melt penetration; therefore, surface tension at the top melt layer seems less effective to widen the pool during the melt penetration. Graphical displays explaining the effect of heat dissipation are provided in Figure A.1, Appendix A, for the description of the temperature and fluid velocity profiles.

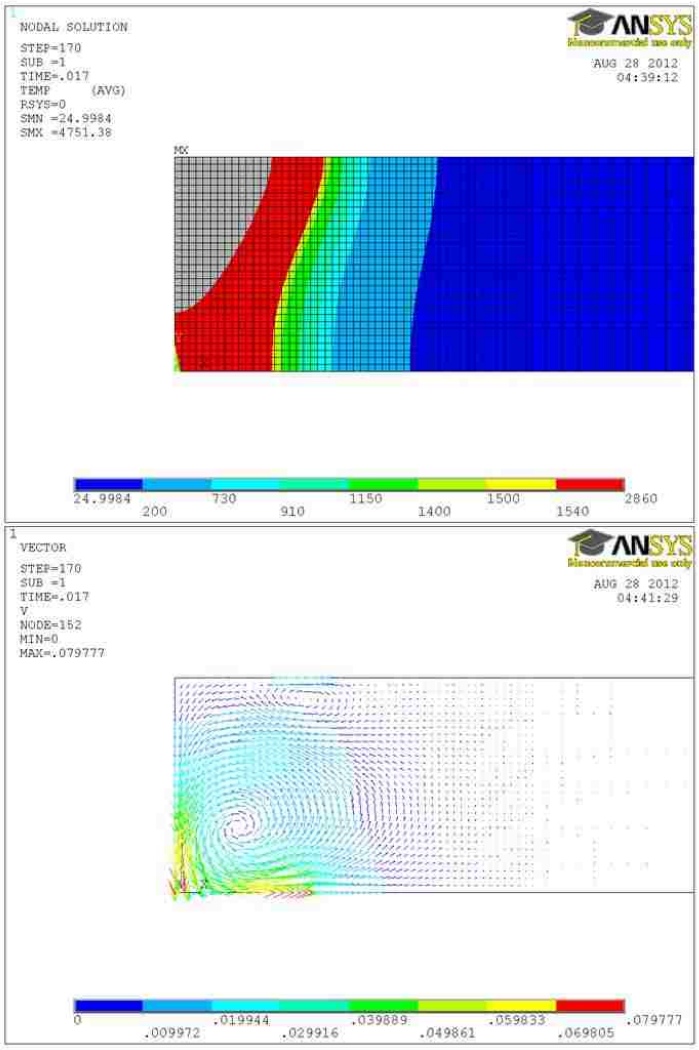

Figure 5.6 Temperature distribution and velocity profile of melt penetration with laser intensity of 3.58×10^{10} W/m^2 and welding velocity of 100 mm/s

5.3 keyhole mode welding

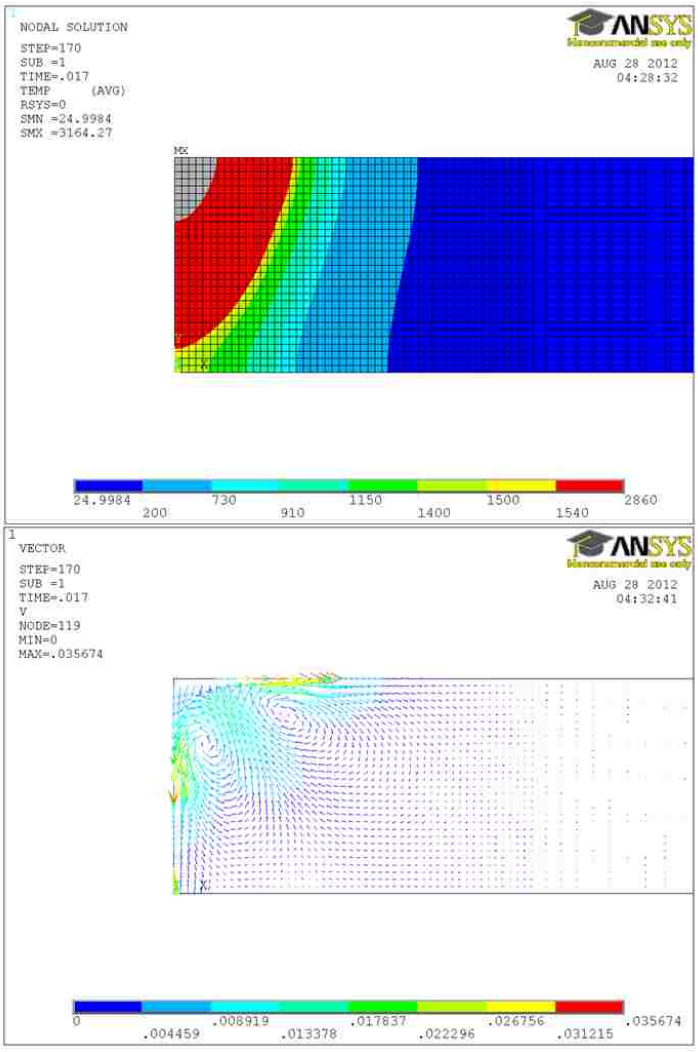

Figure 5.7 Temperature distribution and velocity profile of melt penetration with laser intensity of 2.387×10^{10} W/m^{2}and welding velocity of 100 mm/s

Keyhole mode had a tendency to follow the melt penetration similar to that of hourglass mode, but insufficient heat supply has resulted in lack of penetration instead of an absolute boring path. This computational laser welding process was markedly heat sensitive; therefore, less heat intensity induced no full penetration of the melt as shown in Figure 5.7. The laser intensity used was 2.387×10^{10} W/m^2 and welding velocity was 100 mm/s^2 for this keyhole mode.

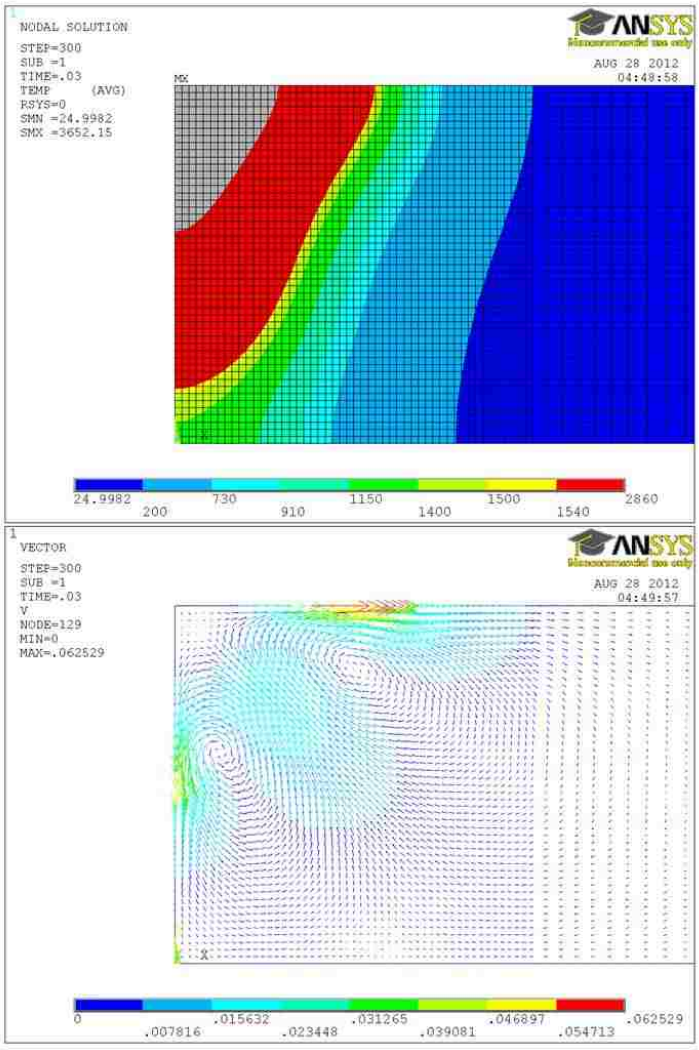

Figure 5.8 Temperature distribution and velocity profile of melt penetration with laser intensity of 5.968×10^{10} W/m^{2}and welding velocity of 100 mm/s

In order to verify of the effect of recoil pressure and surface tension on a melt depth, a plate which has a thickness of 2.0 mm was modeled. As the thicker plate might require more heat for full penetration, the intensity about twice as high as that used in 1.2 mm keyhole mode were applied. The welding velocity was the same as 100 mm/s, and the laser intensity was 5.968×10^{10} W/m^2. As in Figure 5.8, the simulation resulted in no full penetration but indicated that the thicker plate exhibited better description of the melt penetration.

5.4 Evolution of keyhole mode in melt penetration

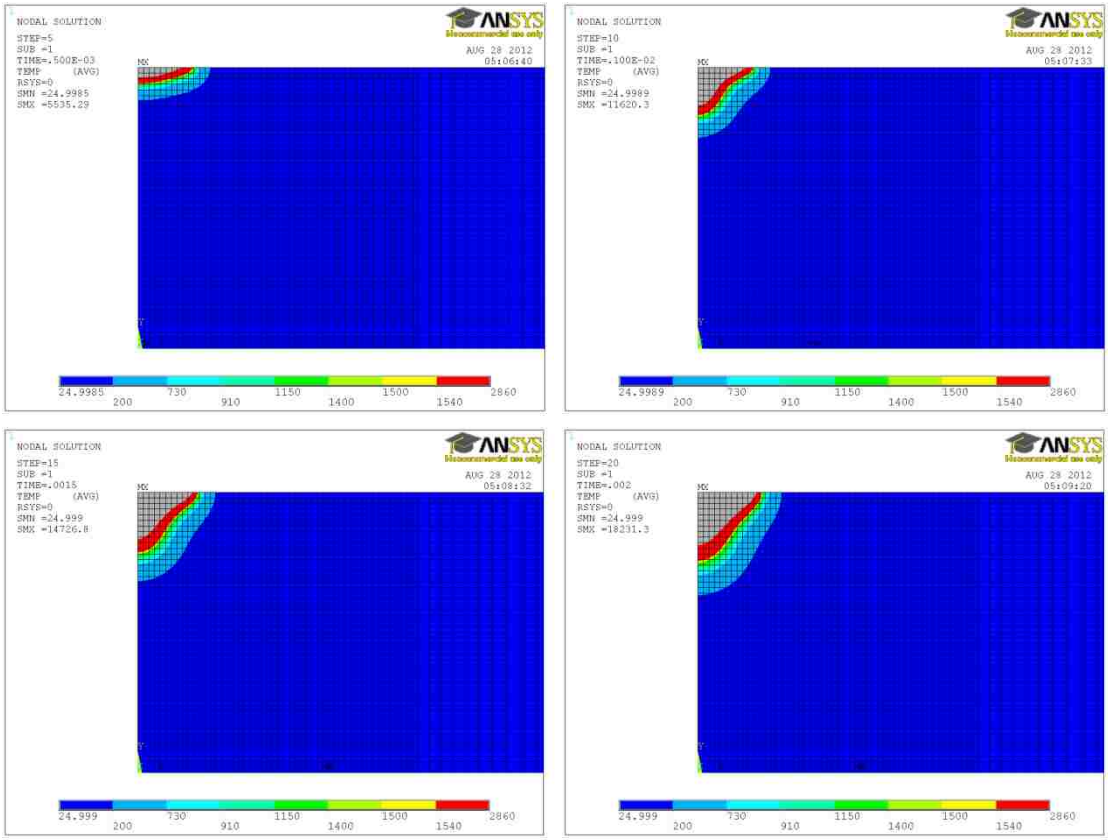

Figure 5.9 Initial stage of melt formation measured at different time steps: 0.5, 1, 1.5, and 2 ms

Iron is about to melt when the laser heat source is approaching the cross-section since the heat density is proportional to the radial distribution of a basic planar disk heat source model. Upon the welding velocities, the melt can be observed before the heat source approaching due to the consideration of the circular heat source moving. Since a welding process with a velocity of 100 mm/s is usually considered as a fast mode welding, this laser welding study requires an extremely small time step to measure the change in melt pool shape. The time steps selected in Figure 5.9 are equivalent to the time at 0.5, 1, 1.5, and 2 ms respectively, and the figures

represent the evolution of the melt pool in its initial stage. The area in grey is the iron in its gas phase above the boiling temperature, and the growth of the area seems responsible for the increase in recoil pressure inside the melt pool. In its initial stage of melt penetration, the melt is ready to penetrate down in the direction parallel to the laser application due to a sudden pressure increase at the melt front.

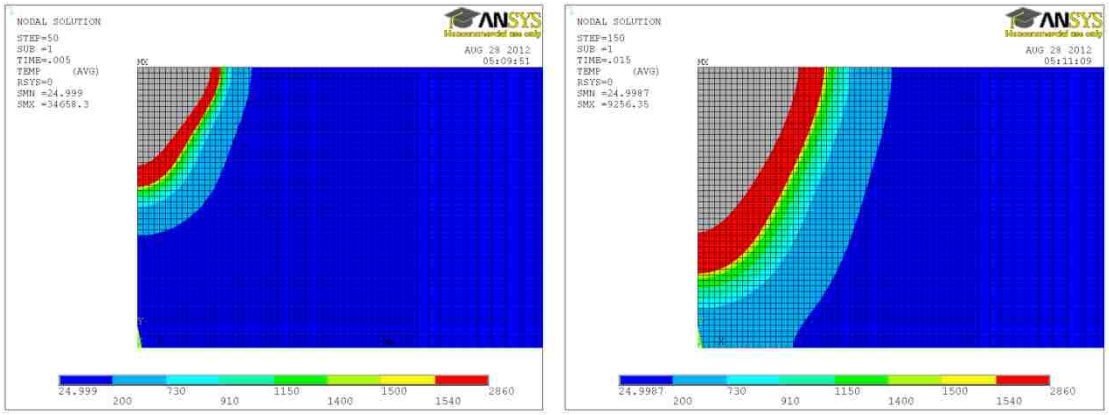

Figure 5.11 Effect of recoil pressure during melt penetration at different time steps: 5 and 15 ms

Beyond the initial stage of melt formation, the penetration propagates down further according to the continuous pressure increase in the melt pool. Laser induced thermal energy keeps influencing the melt to vaporize, thus the rapid evaporation increases the amount of the vapor trapped in the melt pool. As the generation of the vapor is continued in a short period of time, the recoil pressure stimulates the melt to penetrate vigorously as shown in Figure 5.11.

The melt is continuously influenced by the rate of heat transfer through the base metal when the cooling cycle is about to begin with a leaving heat source. Figure 5.12 represents the effect of heat transfer during the cooling cycle. The melt stops penetrating downwards with a decrease in evaporation rate, and the melt starts widening the pool horizontally due to the melt

surface tension. The melt widens the pool width along with the process of penetration, but the major expansion of the pool comes sequentially after the penetration is completed.

The melt evolution is therefore substantially dependent on the relation between recoil pressure in the pool and surface tension on its surface layer. The vertical penetration and horizontal expansion of the melt happen at the same time in real welding dynamics, but the most effectiveness is assumed not to occur simultaneously.

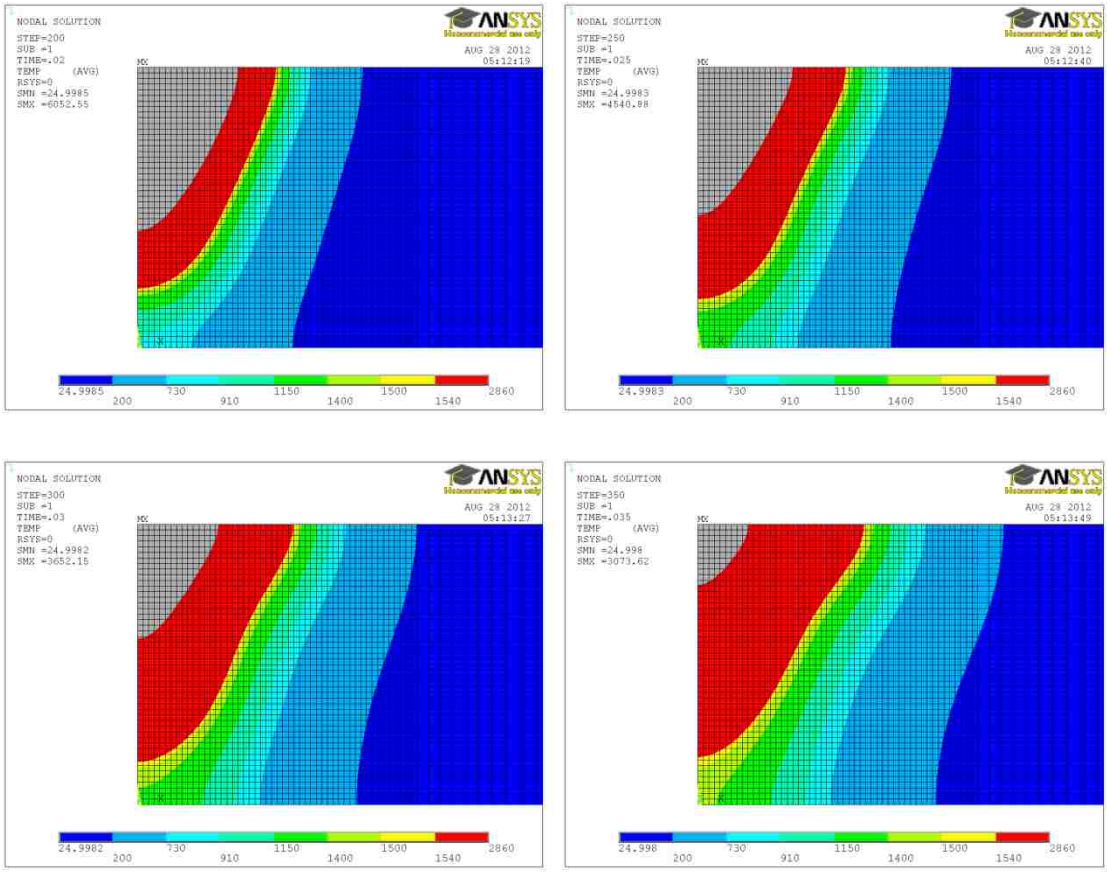

Figure 5.12 Effect of surface tension after melt penetration at different time steps: 20, 25, 30, and 35 ms

5.5 Effect of surface tension on melt pool formation

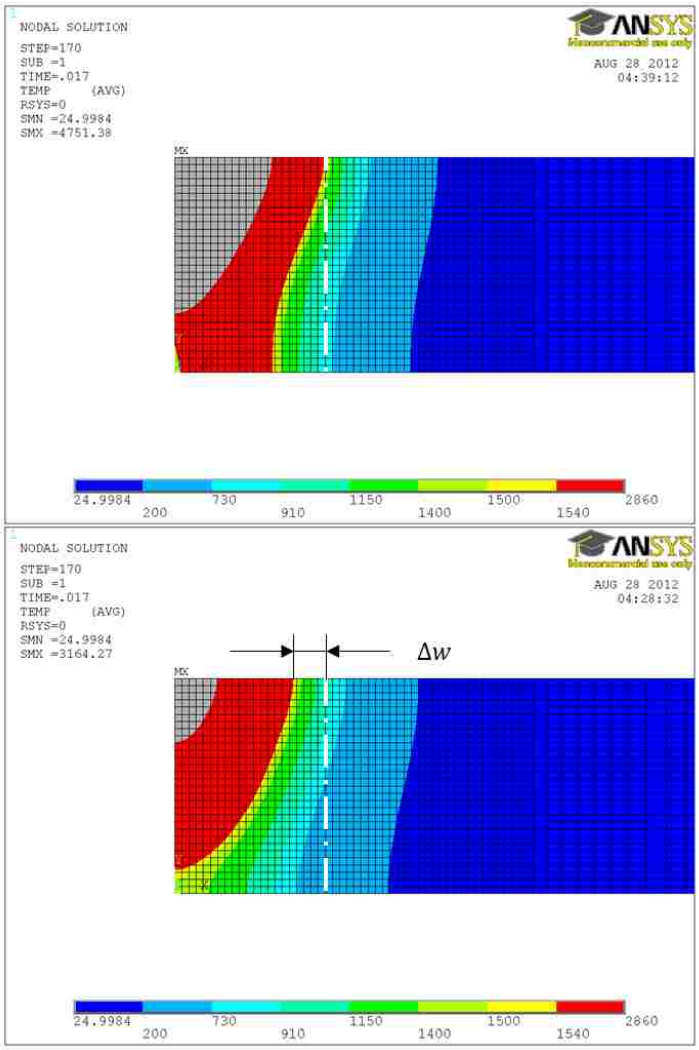

Figure 5.13 Differences in melt pool width due to surface tension with laser intensity of 3.58×10^{10} W/m^2 and welding velocity of 100 mm/s

A surface tension vector tends to be heading towards the direction from the higher to the lower temperature level. Therefore, surface tension in welding is dependent on the relative energy level comparing where the melt is at lower temperatures since surface tension is proportional to the temperature gradient in the direction of increasing slope. A simple meaning is that the higher

surface tension is available at lower temperature, and the direction of tension faces horizontally to the lower temperature. Basic color comparison in Figure 5.13 provides the hottest area which is the center colored in grey. Therefore, the tension raises the magnitude along the direction towards the region in blue. The right hand side of the red on the melt surface collects the highest tension profile as surface tension is valid only in the liquid phase. That is how the tension pushes the melt outwards to widen the width of the pool.

The effect of surface tension was the primary interest in the beginning of this study. Melt penetration could be well observed with increasing laser intensity, but the intensity elevation was not meaningful for the welding phenomena in terms of widening the pool width. A case study without surface tension has been investigated to understand the effect of surface tension on melt pool formation. Figure 5.13 brings two different simulation results to analyze what causes the melt pool to expand. Figure 5.13 is the comparison between the two laser welding processes during the melt penetration:

1) The top profile is the capture of the normal temperature contour with surface tension and recoil pressure
2) The bottom profile is the image captured with no surface tension.

The width difference was clearly noticeable, and the width difference Δw was about 0.16 mm, approximately equivalent to one-third of the radius of the laser beam. The simulation results indicated that the effect of surface tension on melt formation was substantial since the laser intensity and welding velocity were identical.

Figure 5.14 shows the comparison of the expected final weld widths due to the existence of surface tension. The width difference was also apparent, and Δw was approximately 0.08 mm. The difference in relation to the usual case is about 10% reduction in pool width since the usual

melt indicates the width of 0.84 mm, and this is twice larger than the radius of the laser beam. The percentage difference in melt pool width is highly dependent on welding parameters, thus it is less efficient to quantify the relationship between surface tension and pool width. However, the result shows that the surface tension has a substantial effect on lengthening the pool width.

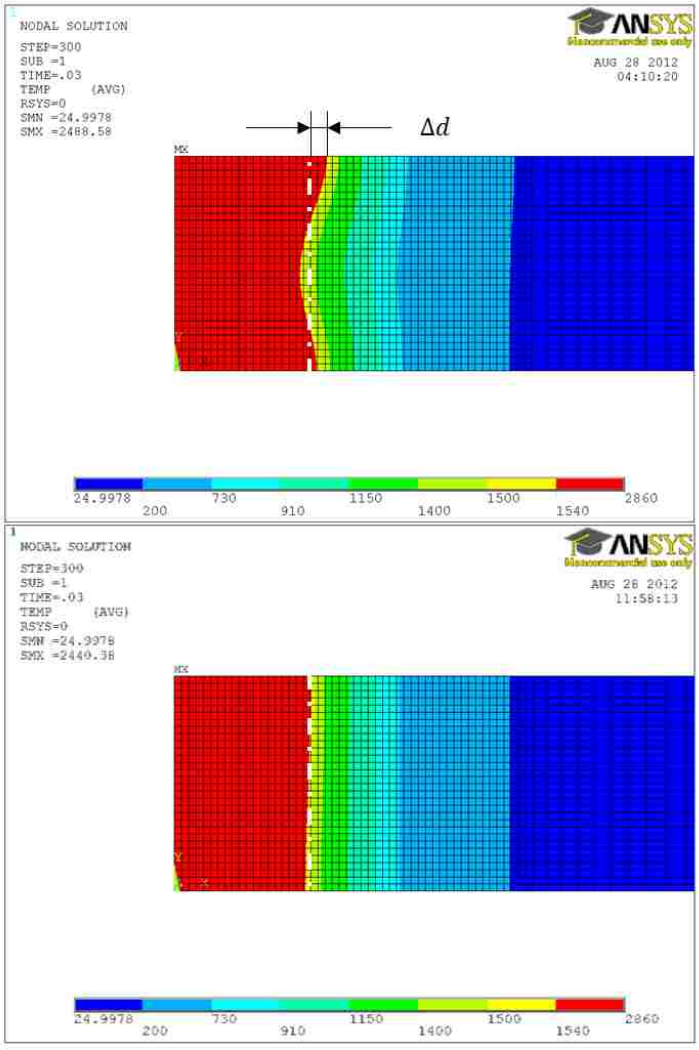

Figure 5.14 Differences in melt pool width due to surface tension with laser intensity of 3.58×10^{10} W/m^2 and welding velocity of 100 mm/s

5.6 Effect of recoil pressure on melt pool formation

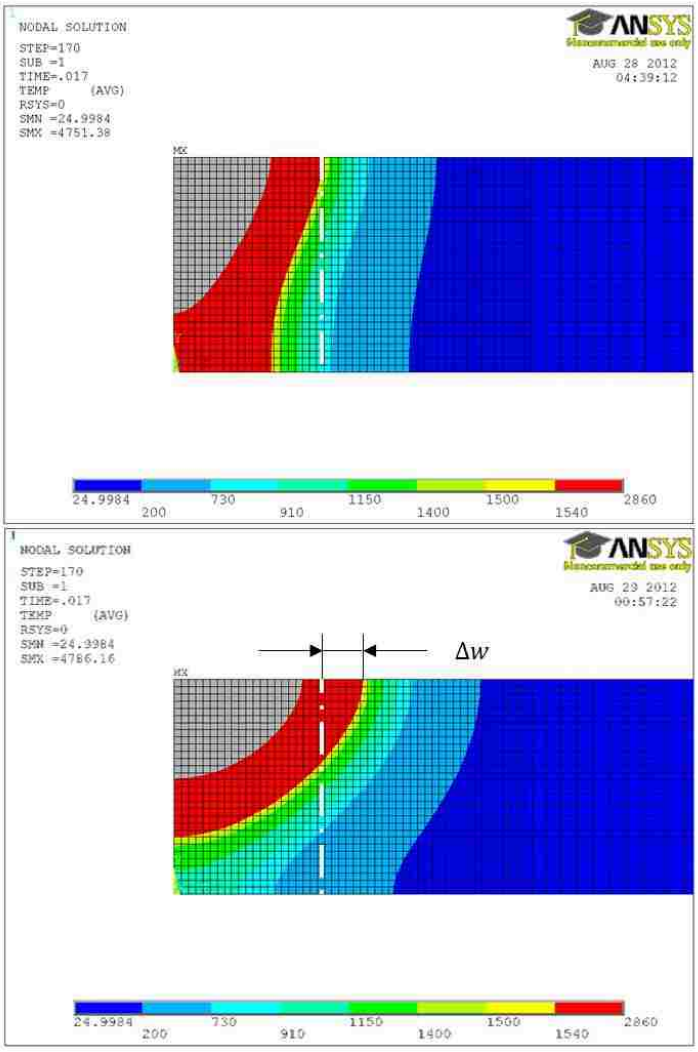

Figure 5.15 Differences in melt pool width due to recoil pressure with laser intensity of 3.58×10^{10} W/m^2 and welding velocity of 100 mm/s

In order to understand the effect of recoil pressure on the formation of the melt pool, a case study without recoil pressure has also been investigated. Figure 5.15 is prepared for the comparison between the two laser welding processes:

1) The top profile is the capture of the temperature contour with recoil pressure and surface tension
2) The bottom profile is the image captured with no recoil pressure.

The width difference is noticeable, and Δw is approximately 0.2 mm. The simulation results indicated that the effect of no recoil pressure during the melt penetration was remarkable when comparing the results with a case study of no surface tension. Zero recoil pressure exhibited larger elongation of the melt width since the major pool dynamics are induced by only surface tension rather than others.

However, Figure 5.16 may require more sophisticated explanation about the melt dynamics because of much wider melt surface. In this study, a physical factor to motivate fluid flow would be surface tension if recoil pressure is invalid. As laser induced rapid heat transfer is related to the vaporization in the melt pool, vigorous iron vaporization rate causes an increase in melt pool pressure which has to be well balanced with the atmospheric pressure. Therefore, the pressure balance forces the vaporized iron to escape from the dense pool area to a sparse region. This escaping process is assumed to be extremely active, thus the melt pool with lack of penetration tries to find another way to emit the pressurized iron vapor. That is why keyhole mode, of which thermal energy is high but insufficient for full penetration, has a relatively deep and narrow hole downwards but very wide top area near the pool surface. The wide top is expected for the evidence of the escaping process.

An expected final weld width due to no recoil pressure is in Figure 5.16. The width difference is clearly noticeable, and Δw was approximately 0.36 mm. The difference in relation to the prior “with recoil pressure” case results in about 42% increase of the pool width since the original melt indicated the width of 0.84 mm. The percentage difference in the pool width is

highly dependent on welding parameters. Hence it is less efficient to quantify the relationship between surface tension and pool width. However, the result shows that the surface tension has a substantial effect on lengthening the pool width.

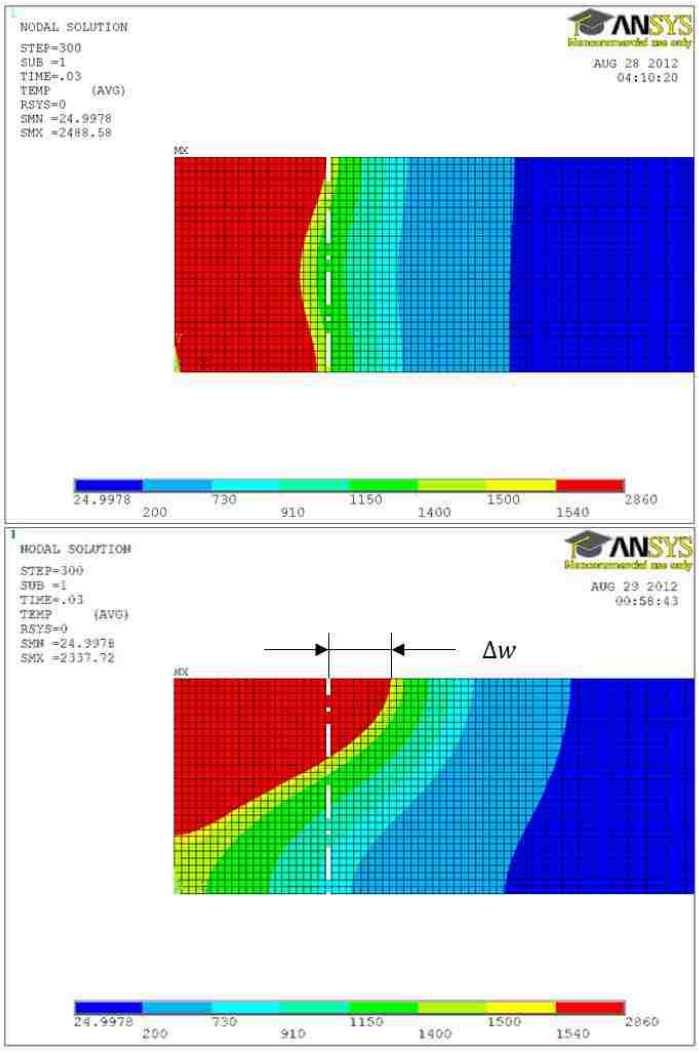

Figure 5.16 Differences in melt pool width due to recoil pressure with laser intensity of 3.58×10^{10} W/m^2 and welding velocity of 100 mm/s

5.7 Effect of welding parameters on melt size and residual stresses

A set of simulations have been compared to understand how the size/shape of the melt pool was influenced by the change in welding parameters. Table 5.1 provides the lists to perform several welding cases varying the welding velocity. The laser intensity was fixed at 3.58×10^{10} W/m^2, and the only variation was the velocity. In the begging of the test, melt was assumed to penetrate a base metal to form a well-balanced hourglass pool, and a set of 100 mm/s and 3.58×10^{10} W/m^2 brought the shape required for hourglass. With the initial set of hourglass mode, the depth and the width of the melt pool were measured while the welding velocities were gradually increased.

Thickness	Welding velocity	Laser intensity	½ width	Depth	Δd
1.2 mm	100 mm/s	3.58×10^{10} W/m^2	0.88 mm	1.2 mm	0 mm
1.2 mm	120 mm/s	3.58×10^{10} W/m^2	0.84 mm	1.2 mm	0 mm
1.2 mm	140 mm/s	3.58×10^{10} W/m^2	0.68 mm	1.2 mm	0 mm
1.2 mm	160 mm/s	3.58×10^{10} W/m^2	0.64 mm	1.08 mm	0.12 mm
1.2 mm	180 mm/s	3.58×10^{10} W/m^2	0.56 mm	0.92 mm	0.28 mm
1.2 mm	200 mm/s	3.58×10^{10} W/m^2	0.52 mm	0.84 mm	0.36 mm

Table 5.1 List of simulation set for welding velocity variation at constant heat intensity

The simulation results are graphically displayed in Figure 5.17. The x- and y-axis values are non-dimensional width and penetration thickness. The original units of measurement are [mm], and the measurements are expressed dimensionless. Δw is a measure of distance from the center to where the melt is in the liquid phase. Δd represents a not-yet-melted vertical distance from the top to the bottom layer. If Δd is equal to zero, the melt penetrates a base metal fully.

Thickness	Welding velocity	Laser intensity	Fig. No.
1.2 mm	100 mm/s	1.79×10^{10} W/m^2	A.2
1.2 mm	100 mm/s	2.38×10^{10} W/m^2	A.3
1.2 mm	100 mm/s	2.98×10^{10} W/m^2	A.4
1.2 mm	100 mm/s	3.58×10^{10} W/m^2	A.5
2.0 mm	100 mm/s	5.96×10^{10} W/m^2	A.6

Table 5.2 List of simulation set for laser intensity variation at constant welding velocity

Figure 5.17 shows that insufficient heat accumulation results in the decrease in the width and depth of the melt pool. It is assumed that the cross-section area did not collect enough thermal energy with increasing welding velocity since a fast welding process prevents heat from staying longer in the desired spot.

Another set of simulations were performed to measure the distribution of residual stresses on 1.2 mm and 2.0 mm thick plates varying laser heat intensity in the range of 1.79×10^{10} W/m^2 to 5.96×10^{10} W/m^2. The welding velocity remained constant, thus the results presented the effect of laser intensity variation. The stress profiles are given in Figure 5.18, and the individual contour profiles are in Appendix A as listed in Table 5.2. Reading the profiles, the peaks of the maximum residual stresses are shifted with increasing laser intensity. As the melt pool can expand more with increasing laser intensity, one possibility of the stress shifting can be related to the fluidity of melt. The melt with sufficient energy is able to flow wider due to the increase in temperature dependent surface tension which drags the melt towards the not-yet-melted region. Hence we may assume the sufficient intensity can require longer solidification. However, the profiles in Figure 5.18 were only measured with insufficient cooling time due to the computational limits; therefore, there will be no direct way to predict the final distribution of residual stresses.

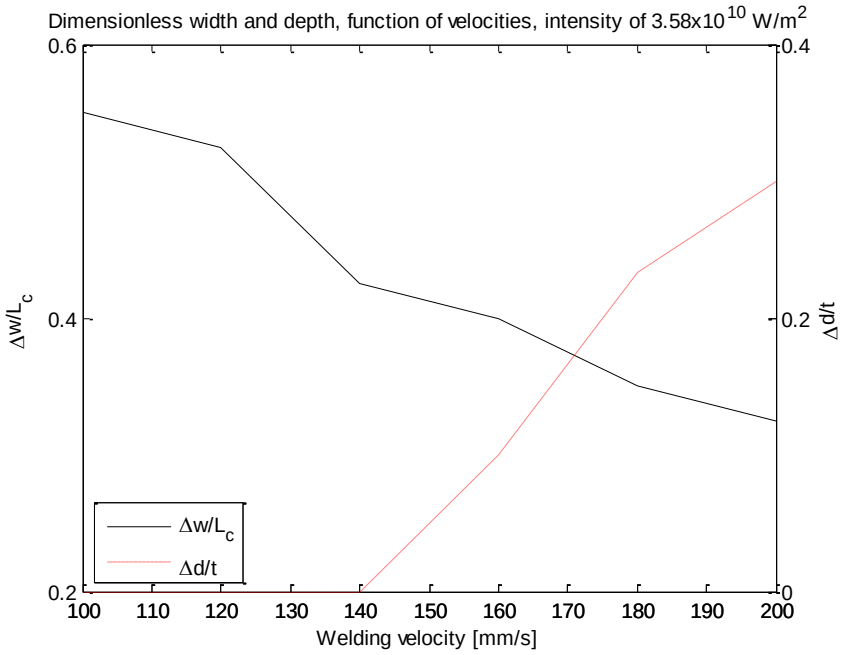

Figure 5.17 Differences in melt pool width due to recoil pressure with constant laser intensity of 3.58×10^{10} W/m^2 and welding velocity in the range of 100 mm/s to 200 mm/s

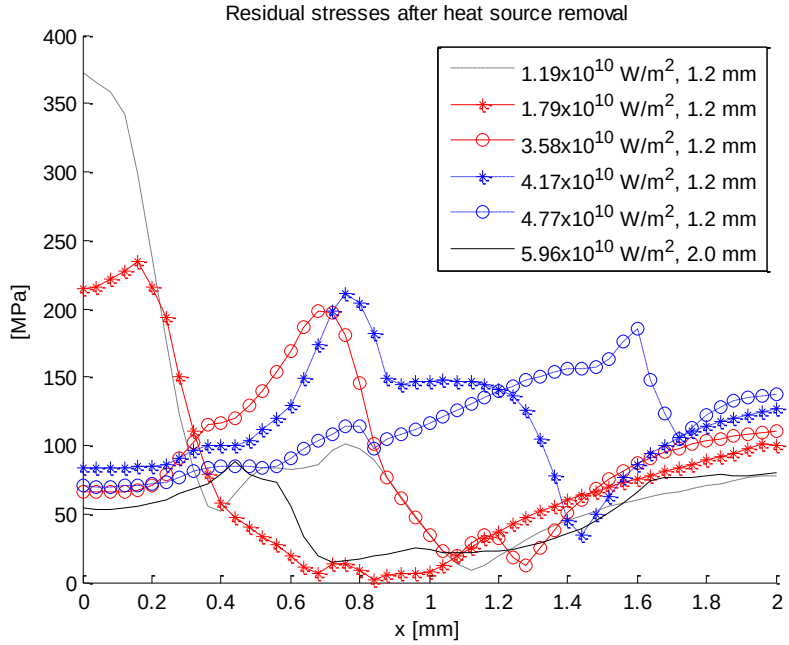

Figure 5.18 Differences in distribution of residual stresses with variable laser intensities at constant welding velocity of 100 mm/s

5.8 Dimensionless numbers and width of melt pool

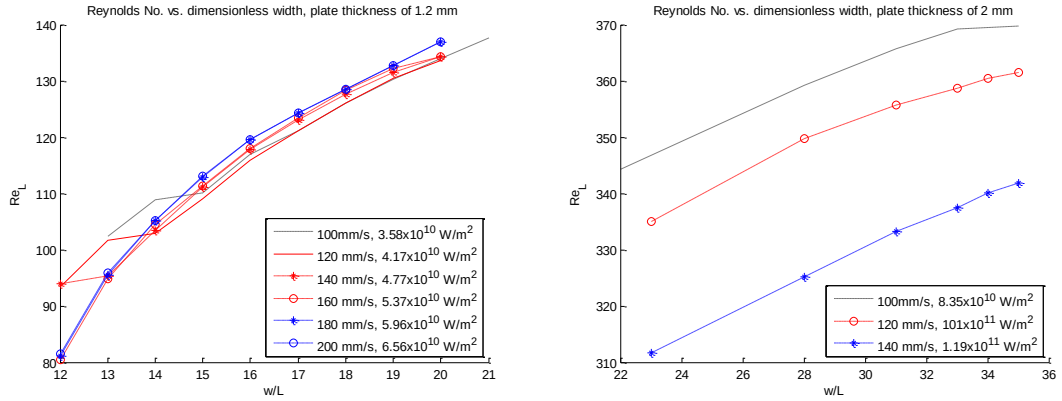

Figure 5.19 Reynolds' number vs. dimensionless width of melt pool with plate thickness of: 1) left: 1.2 mm, and 2) right: 2.0 mm

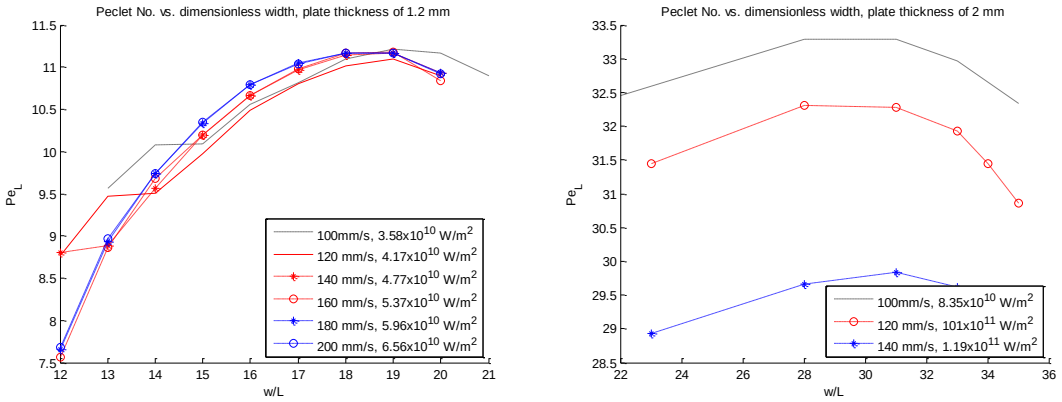

Figure 5.20 Péclet number vs. dimensionless width of melt pool with plate thickness of: 1) left: 1.2 mm, and 2) right: 2.0 mm

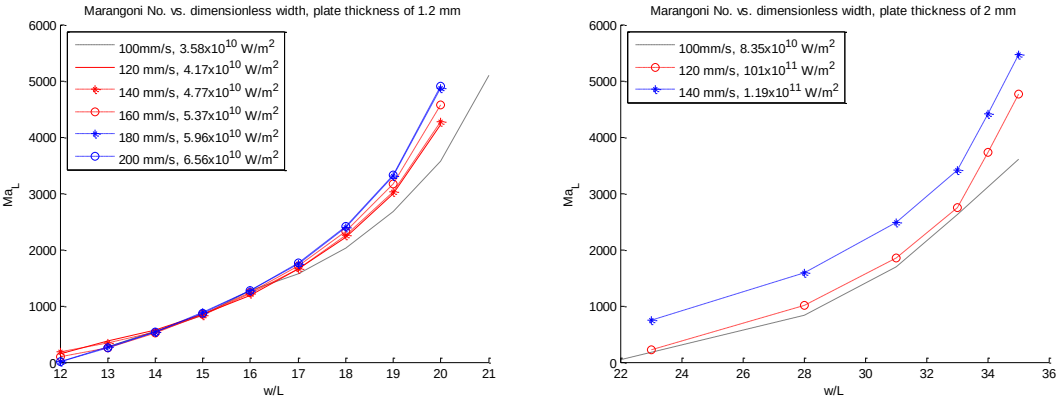

Figure 5.21 Marangoni number vs. dimensionless width of melt pool with plate thickness of: 1) left: 1.2 mm, and 2) right: 2.0 mm

Two different plates of thickness 1.2 and 2.0 mm were used to compare dimensionless numbers e.g., Re, Pe, and Ma, with a normalized pool width, w/L. The characteristic length L was introduced to replace the actual pool size with w/L. The two plates were examined with various welding velocities and laser intensities. The set of comparisons described that the change in dimensionless parameters had a close relation with w/L while generating a continuous correlation curvature path. Sampling velocity and laser intensity were selected depending on the shape of the melt pool. The laser intensity was chosen when the melt formed a well-balanced hourglass shaped pool as shown in Figure 5.4; the velocity was obtained at the top melt surface layer. In Figures 5.19 through 5.21, a plate thickness of 1.2 mm shows all the dimensionless numbers are well converged into a single curvature only with a slight deviation. In contrast, a thickness of 2.0 mm exhibits no such conversions. Data fitting however resulted in the relation between the dimensionless numbers and normalized width, and the changing tendency was predictable following the curvatures in all figures. We may assume the laser welding requires restrictions on the thickness of a plate to increase reliability when using dimensionless numbers.

Buoyancy was treated with no great circumspection in this research since gravitation was assumed to be a negligible effect on laser welding of thin metal sheets; however, Rayleigh number was computed to verify no significance of buoyancy driven flow. Material properties required for Rayleigh number was evaluated at the film temperature, which was the average temperature on the melt surface and ambient air temperatures.

$$Ra = \frac{g\beta}{\nu\alpha} \cdot (T_s - T_\infty) \cdot L^3 = \frac{g\rho^2 c_p \beta}{\mu k} \cdot (T_s - T_\infty) \cdot L^3 = 0.0954 \qquad (5.2)$$

Equation (5.2) is the result of Rayleigh analogy with a profile associated with Figure 5.4 where β is the coefficient of thermal linear expansion (α_L) and α is the thermal diffusivity. Ra is often a large number around 10^6 to 10^9 for most engineering purposes, heat energy transfer by natural convection mode seems less effective in this laser welding process.

5.9 Melt radiation and thermal conductivity

In an earlier chapter, thermal conductivity of pure iron was modified for the linearized radiation heat transfer at the liquid-gas boundary. If multiple internal reflections of radiation were expected during melt penetration, an increase in k_r which was proportional to the rate of radiation by the use of impinging jet convection, could be much higher than the estimates. Assuming that an arbitrary increase in the thermal conductivity was allowable to compensate the amount of energy gain by multiple reflections, the thermal conductivity over the boiling point could have a fictitious increment by several orders of magnitude as shown in Figure 5.22. The laser intensity of 3.58×10^{10} W/m^2 and the welding velocity of 100 mm/s^2 were selected for the comparison of the results between one using the predetermined thermal conductivity and the other with an arbitrary increase in the profile.

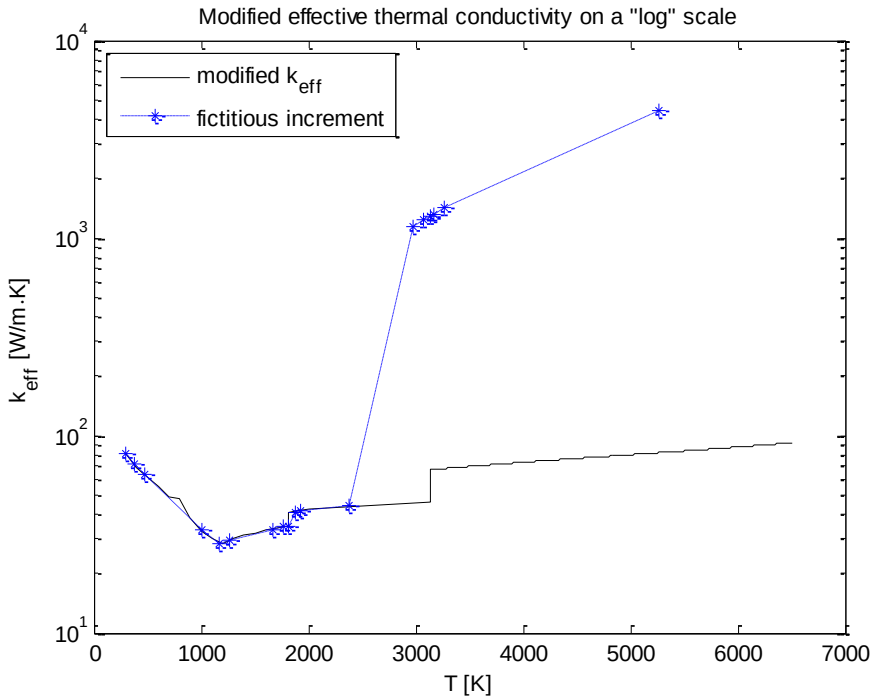

Figure 5.22 Fictitious increments in thermal conductivity as a function of temperature degrees in Kelvin

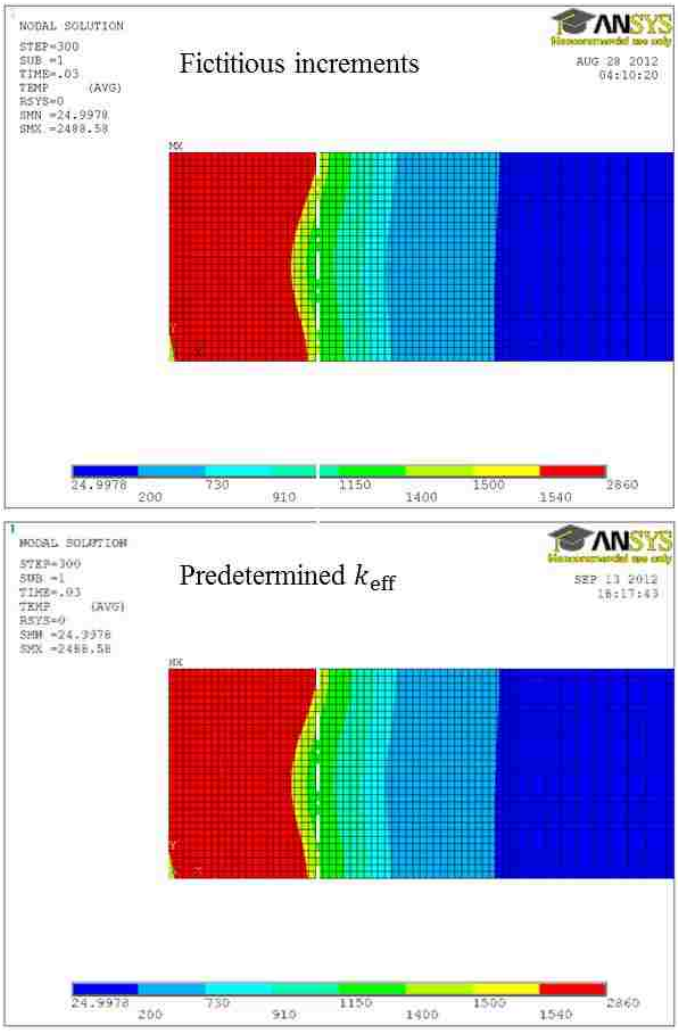

Figure 5.23 Temperature distribution comparisons between two different thermal conductivity sets: measured after melt penetration with intensity of 3.58×10^{10} W/m^2 and velocity of 100 mm/s

The fictitious case exhibits no significant changes when its temperature distributions are compared with the predetermined case as shown in Figure 5.23. The widths of melt pools which are measured after melt penetration are identical as displayed. The comparisons during the melt penetration also show similar graphical results, and the temperature distributions are provided in Appendix A, Figure A.7.

Figure 5.23 shows that the thermal conductivity associated with radiation above the boiling point does not have a great influence on the melt pool shape. Therefore, low carbon steel used in a laser welding study [4] was employed to verify how the change in thermal conductivity influences on the formation of the melt pool when it varies by the use of a different material. The thermal conductivity of low carbon steel has no modification for radiation internal reflections, and Figure 5.24 shows the thermal conductivities of the predetermined set and the low carbon steel. The difference between two sets of the thermal conductivities is clearly noticeable in their initial stages. Figure 5.25 is the corresponding results measured at 30 ms, the same time step used for a measure of Figure 5.23. The temperature contour shows how the initial difference of thermal conductivity influences the overall temperature distribution of the melt pool. The combination of the laser intensity and welding velocity used for low carbon steel results in a process of "laser cutting" than laser welding since the pool has full of evaporated vapors along the path of penetration by the relatively low initial thermal conductivity profiles. As a result of that, the thermal conductivity in a range close to room temperature is assumed to be highly responsible for the overall temperature distribution during melt penetration.

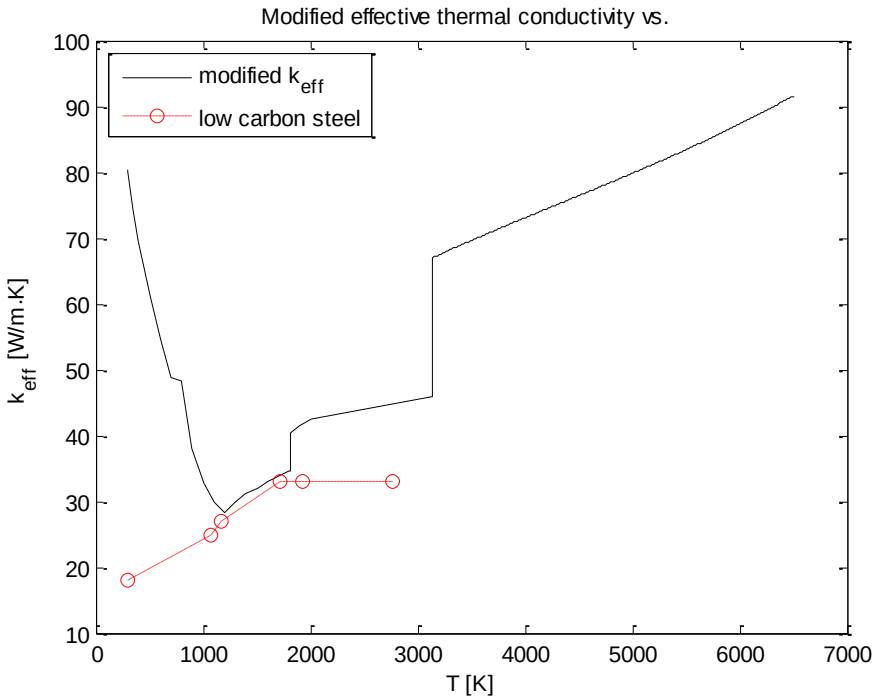

Figure 5.24 Thermal conductivity of low carbon steel as a function of temperature degrees in Kelvin

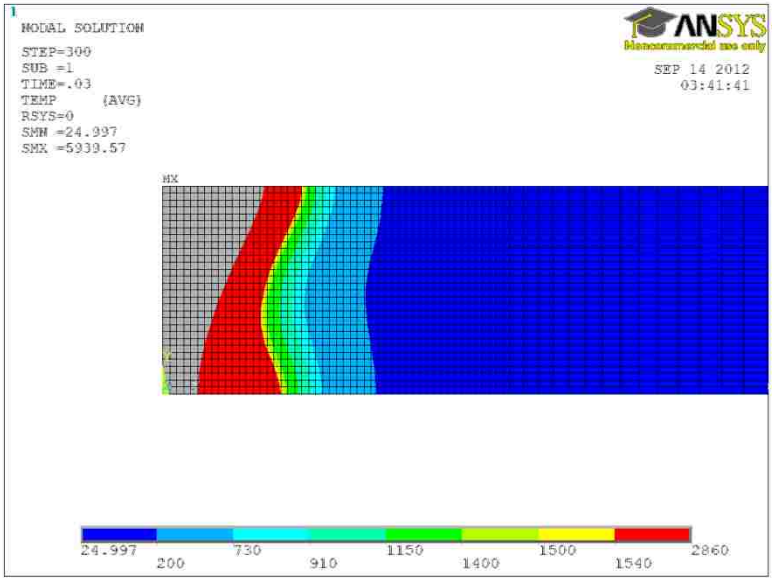

Figure 5.25 Thermal conductivity of low carbon steel with no modification for radiation internal reflections measured at 30 ms with intensity of 3.58×10^{10} W/m^2 and velocity of 100 mm/s

5.10 Elevation of residual stresses

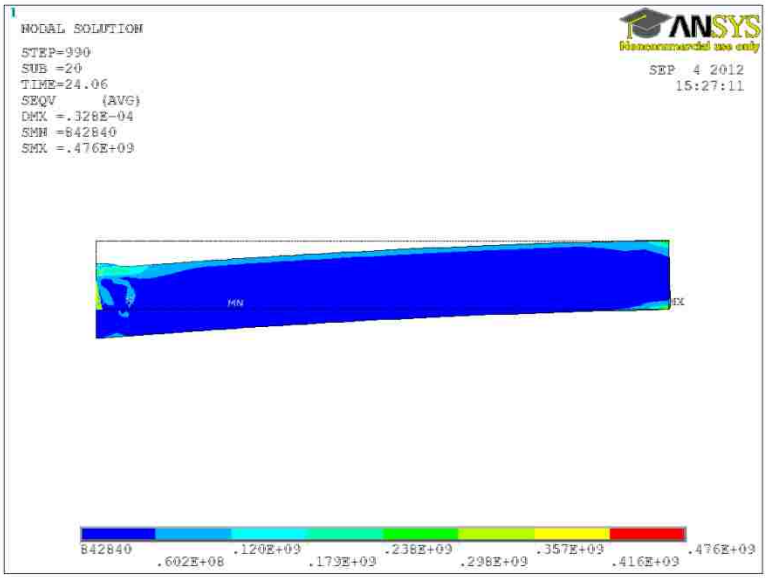

Figure 5.26 Stress elevations in cooling with welding velocity of 100 mm/s and laser intensity of 1.79×10^{10} W/m^2 on 1.2 mm thickness iron

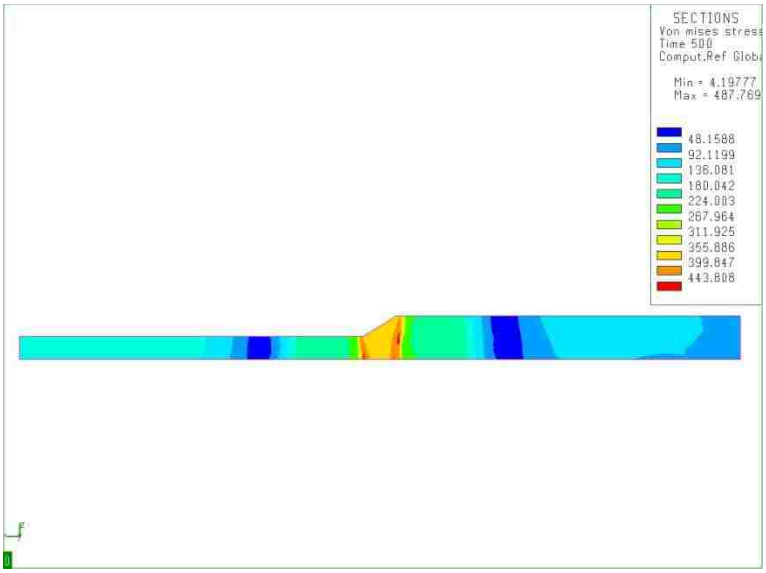

Figure 5.27 Stress elevations during solidification with welding velocity of 133mm/s and laser power of 2700 W on 0.64/1.2 mm thickness low carbon steel [4]

Thickness	Welding velocity	Laser intensity	Laser power	Code
1.2 mm	100 mm/s	1.19×10^{10} W/m^2	-	ANSYS
0.64/1.2 mm	133 mm/s	-	2700 W	SYSWELD

Table 5.3 Welding parameters used in commercial codes ANSYS and SYSWELD

Figures 5.26 and 5.27 describe the distributions of the residual stresses in solidification of pure iron and low carbon steel using commercial codes ANSYS and SYSWELD respectively. Residual stresses which were measured for a simulation in ANSYS were not obtained with sufficient solidification time to cool the weld down to room temperature, but another set measured in SYSWELD was based on relatively enough solidification time. As shown in Figure 5.27, the fusion joining of different plate thickness resulted in symmetric stress distribution.

All the stress results were a use of Von Mises criterion, and both cases collected similar stress elevation near the weld joint. ANSYS yielded a maximum residual stress of 370 MPa at the weld joint. SYSWELD computed the residual stresses, and the average was in the range of 355 to 399 MPa. We are not able to compare both two results precisely due to the difference in solidification time and welding parameters, but results show “similar tendency of residual stress elevation” where heat source is applied.

5.11 Final weld shape

The simulation results were compared with an experimental observation investigated on a piece of a low carbon steel sheet having similarities on the geometries and mechanical properties. Laser butt welding has made the weld joint between 1.2 mm and 0.64 mm low carbon steel sheets, and the observation of the microstructure showed that final weld formed an hourglass shape at the interface of two plates. [4] The final weld shape through the simulation of hourglass mode laser welding is graphical compared with the experiment in Figure 5.28. The results clearly exhibit the existence of pool widening and pool penetration relevant to surface tension and recoil pressure respectively although there is a slight width difference between the results. As in Figure 5.28, we may assume that the shape/size of melt pool is highly dependent on melt dynamics associated with surface tension over the melting point and recoil pressure over the boiling point.

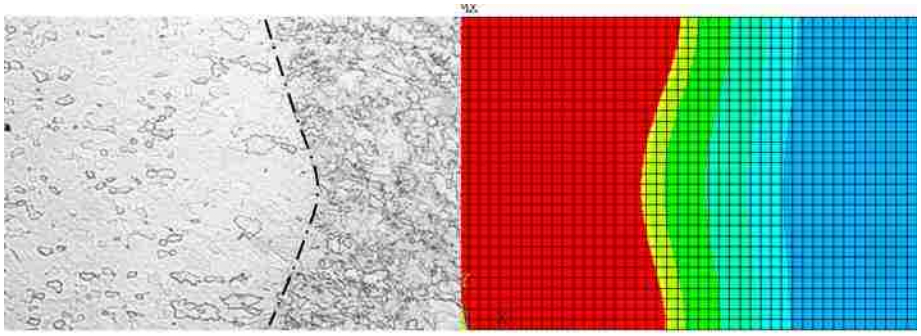

Figure 5.28 Results of numerical simulation compared with experiments [4]

Chapter 6 Conclusion

The early purpose of this study was to find an appropriate laser heat source model which was suitable for the hourglass melt penetration mode. The research focus was how to model the shape of heat source since the volumetric laser heat source, i.e. a conical heat source modeling with wide top and narrow bottom radii as shown in Figures 1.1 and 1.8, was not adequate to form an hourglass. During the literature surveys, however, it was clear that the old heat source models were no longer valid to explain laser induced melt penetration due to no consideration of melt flow and the modeling was apparently based on the experimental observations with no scientific evidence for welding mechanisms. Realizing insufficient theoretical approaches, a fundamental study on the thermo-fluid mechanisms was required to understand the formation of the melt pool. Therefore, the real purpose of this laser welding simulation has resulted in how the welding parameters were correlated with one another influencing the formation of the final weld shape.

Studying thermo-fluid dynamics was readily conducted to estimate a melt behavior in the molten pool. Navier-stokes equation was first employed to describe the melt flow assuming that melt was an incompressible viscous Newtonian fluid. As known that enormous heat energy was involved in laser welding, rapid solid to gas phase transformation was responsible for the melt drilling effect. Pressure was assumed to be one of the influences causing the melt to flow, thus the equilibrium in pressure required Clausius-Clapeyron equation to compute the rate of increase in melt evaporation. As a result, the rapid evaporation has led to a relation between the evaporation and the evaporation pressure, which was expected to be equivalent to the melt recoil pressure stimulating the melt to drill down further during laser welding. Recoil pressure was therefore of great interest to be associated with the vigorous melt penetration. As “hourglass” is a type of melt penetration named after its shape, surface tension was also equated to explain the melt widening

effect on its surface layer. A proper boundary condition was required to explain convection heat transfer on the melt surface. The existence of surface tension was the evidence that the surface tension could lower the thermal energy by convection heat transfer for its physical stability. A dimensionless parameter called the Marangoni number was employed to obtain the relation between the melt flow by surface tension and the consequent melt temperature gradient along the melt surface layer.

Non-dimensionalization is known as an effective way of expression to describe the overall influence of multiple variables when we cannot choose a specific variable. The physics of welding has included many uncertainties due to the fact that its phenomena were not that simple to be estimated by changing one single parameter. As well as the Marangoni number, Reynolds's and Péclet numbers were therefore adopted to predict better control of the laser welding process in terms of forming hourglass melt penetration. As mentioned in an earlier chapter, the application of melt dynamics was based on the assumption that the melt flow had a great effect on the final shape of the melt. This laser welding simulation study has been performed through many trials and errors; therefore, the dimensionless parameters were finally obtained as a function of dimensionless width of the melt pool.

All the dimensionless numbers were measured at the top melt surface when the melt flow was stable enough. The melt velocities tended to increase or decrease gradually with better stability at an average pool velocity of 0.064 m/s after melt penetration. Hence, the velocity was collected at the point where the maximum velocity occurred in the cooling cycle. The characteristic length was approximated following the relation of $L = r_0$ where r_0 is the radius of laser beam. Similar to the first thought referred to in a laser welding study [16], the predetermined characteristic length remained constant during the study. In general, a geometrically invariable length is very useful to have results dimensionless for any purposes.

The effect of change in welding parameters has also been investigated during the structure analysis. The study was coupled thermo-fluid-structure analysis; hence, the results from structure analysis could be responsive to the parameter changes. However, the structure analysis has not been fully performed with reliable accuracy due to the limited computation resources. Welding velocity was relatively high compared to the classical arc welding numerical techniques. High speed welding requires extremely fine mesh around the heat affected zone and infinitesimal overall time steps in order not to lose any information of the temperatures which were also used for the application of temperature-dependent loads. As a result of that, most of the time steps were spent to observe the evolution of the melt pool rather than solidification. However, stress variation was measurable from the begging of laser welding, and the distribution of residual stresses was valuable to verify the effect of the melt flow on the stress elevation.

Finally, this laser welding study indicated that the melt flow had a significant effect on the final melt pool shape. Melt pool geometry was moreover indirectly related to the initial heat source shape because there was no predetermined heat density distribution to the depth direction unlike most heat source modeling. The use of the F.E. based numerical techniques obviously could save time and efforts mostly required for experiments along with fundamental studies on the melt pool heat transfer mechanism to understand the laser welding process and explain all of the relevant welding phenomena. The advantages and dedication of this study are considered as: 1) melt behavior can be predictable using numerical computation techniques, 2) melt width can be predictable using melt surface velocity, and 3) couple thermo-fluid-structure can provide better understand of laser welding.

References

Chapter 1

[1] Deyev, G. F., and Deyev, D, G., 2006, *Surface Phenomena in Fusion Welding Processes*, CRC Press, Boca Raton, FL.

[2] Shanmugam, N. S., Buvanashekaran, G., Sankaranarayanasamy, K., and Kumar, S. R., 2010, "A transient finite element simulation of the temperature and bead profiles of t-joint laser welds," Materials & Design, **31**(9), pp. 4528-4542.

[3] Kannatey-Asibu, E., 2009, *Principles of Laser Materials Processing*, John Wiley & Sons, Inc., Hoboken, NJ.

[4] Pornsak, T., 2012, "A study on the welding characteristics of tailor welded blank metal sheets using laser and GTAW welding," Ph.D. dissertation, Lehigh University, Bethlehem, PA.

[5] Bozorgi, P., Burgner, C.B., Yie, Z., Ding, C., Turner, K. L., and MacDonald, N. C., "Application of Millisecond Pulsed Laser Welding in MEMS Packaging," University of California Santa Barbara, Santa Barbara, CA.

[6] Luo, C., and Lin, L., 2002, "The Application of Nanosecond-pulsed Laser Welding Technology in MEMS Packaging with a Shadow Mask," Sensors and Actuators A, **97-98**, pp. 398-404.

[7] Nawi, I. N., Saktioto, T., Fadhali M., Hussain M. S., Ali J., and Yupapin P. P., 2011, "A Reliable Nd:YAG Laser Welding Welded Stainless Steel 304 for Photonics Device Packaging Application," Procedia Engineering, **8**, pp. 380-385.

[8] Kuang, J., Sheen, M., Wang, S., Wang, G., and Cheng, W., 2001, "Post-weld-shift in Dual-in-line Laser Package," IEEE Transactions on Advanced Packaging, **24**, pp. 81-85.

[9] Lin, Y., Liu, W., and Shi, F. G., 2002, "Laser Welding Induced Alignment Distortion in Butterfly Laser Module Packages: Effect of Welding Sequence," IEEE Transactions on Advanced Packaging, **25**, pp. 73-78.

[10] Ion, J. C., 2005, *Laser Processing of Engineering Materials*, Elsevier Butterworth-Heinemann, Burlington, MA.

[11] Gao, Z., and Ojo, O. A., 2012, "Modeling analysis of hybrid laser-arc welding of single-crystal nickel-base superalloys," Acta Materialia, **60**, pp. 3153-3167.

[12] Chang, W. S., and Na, S. J., 2002, "A study on the prediction of the laser weld shape with varying heat source equations and the thermal distortion of a small structure in micro-joining," Journal of Materials Processing Technology, **120**, pp. 208-214.

[13] Gery, D., Long, H., and Maropoulos, P., 2005, "Effect of Welding Speed, Energy Input and Heat Source Distribution on Temperature Variations in Butt Joint Welding," Journal of Material Processing Technology, **167**, pp. 393-401.

[14] Semak, V. V., Hopkins, J. A., McCay, M. H., and McCay, T. D., 1995, "Melt Pool Dynamics during Laser Welding," J. Phys. D: Appl. Phys., **28**, pp. 2443-2450.

[15] Du, H., Hu, L., Liu, J., and Hu, X., 2004, "A Study on the Metal Flow in Full Penetration Laser Beam Welding for Titanium Alloy," Computational Materials Science, **29**, pp. 419-427.

[16] Ye, X., and Chen, X., 2002, "Three-dimensional Modeling of Heat Transfer and Fluid Flow in Laser Full-penetration Welding," J. Phys. D: Appl. Phys., **35**(10), pp. 1049-1056.

[17] Cho, W., Na, S., Thomy, C., and Vollertsen, F., 2012, "Numerical Simulation of Molten Pool Dynamics in High Power Disk Laser Welding," Journal of Materials Processing Technology, **212**(1), pp.262-275.

[18] Moraitis, G. A., and Labeas, G. N., 2008, "Residual stress and distortion calculation of laser beam welding for aluminum lap joints," Journal of Material Processing Technology, **198**, pp. 260-269.

[19] Wang, R., Lei, Y., and Shi, Y., 2011, "Numerical Simulation of Transient Temperature Field during Laser Keyhole Welding of 304 Stainless Steel Sheet," Optics & Laser Technology, **43**, pp.870-873.

[20] Postma, S., 2003," Weld pool control in Nd:YAG laser welding," Ph.D. thesis, University of Twente, Enschede, Netherlands.

[21] Rosenthal, D., 1946, "The Theory of Moving Sources of Heat and Its Application to Metal Treatments," Transaction of the American Society of Mechanical Engineers, **68**, pp. 849–866.

[22] Goldak, J., Chakravarti, A., and Bibby, M., 1984, "A New Finite Element Model for Welding Heat Sources," Metallurgical Transactions B, **15**(2), pp. 299-305.
[23] Goldak, J., Bibby, M., Moore, J., House, R., and Patel, B., 1986, "Computer Modeling of Heat Flow in Welds," Metallurgical Transactions B, **17**(3), pp. 587-600.

Chapter 2

[24] Tisza M., 2001, *Physical Metallurgy for Engineers*, ASM International, Material Park, OH.
[25] Kakani S.L., 2004, *Material Science*, New Age International (P) Ltd., New Delhi, India.
[26] Touloukian Y. S., and Ho, C. Y., 1981, *Properties of Selected Ferrous Alloying Elements*, McGraw-Hill, New York City, NY.
[27] Assael, M. J., Kakosimos, K., Banish, R. M., Brillo, J., Egry, I., Brooks, R., Quested, P. N., Mills, K. C., Nagashima, A., Sato, Y., and Wakeham, W. A., 2006, "Reference Data for the Density and Viscosity of Liquid Aluminum and Liquid Iron," J. Phys. Chem. Ref. Data, **35**(1), pp. 285-300.
[28] Beutl, M., Pottlacher, G., and Jäger, H., 1994, "Thermophysical Properties of Liquid Iron," International Journal of Thermophysics, 15(6), pp. 1323-1331.
[29] Hultgren, R. R., 1973, *Selected Values of the Thermodynamic Properties of the elements*, American Society for Metals, Metals Park, OH.
[30] Wilthan, B., Cagran, C., and Pottlacher, G., 2004, "Combined DSC and Pulse-Heating Measurements of Electrical Resistivity and Enthalpy of Platinum, Iron, and Nickel," International Journal of Thermodynamics, **25**(5).
[31] Hixson, R. S., Winkler, M. A., and Hodgdon, M. L., 1990, "Sound speed and thermophysical properties of liquid iron and nickel," Physical Review B, **42**(10), pp. 6485-6491.
[32] Kachhava, C. M., 2003, *Solid State Physics, Solid State Devices and Electronics*, New Age International (P) Ltd. Publishers, New Delhi, India.
[33] Baukal, C. E., Gershtein, V. Y. and Li, X., 2001, *Computational Fluid Dynamics in Industrial Combustion*, CRC Press, Boca Raton, FL.
[34] Tottle, C. R., 1984, *An Encyclopaedia of Metallurgy and Materials*, Macdonald & Evans Ltd, Plymouth, UK.
[35] Totten, G. E., 2007, *Steel Heat Treatment: Metallurgy and technologies*, CRC Press, Boca Raton, FL.
[36] Totten, G. E., and Howse, M. A. H., 1997, *Steel Heat Treatment Handbook*, CRC Press, Boca Raton, FL.
[37] Powell, R. W., Ho, C. Y., and Liley, P. E., 1974, "Thermal Conductivity of the Elements: A Comprehensive Review*,"* Journal of Physics and Chemical Reference Data, **3**(1) pp. 1-796.
[38] Peet, M. J., Hasan, H. S., and Bhadeshia, H. K. D. H., 2011, "Prediction of thermal conductivity of steel," International Journal of Heat and Mass Transfer, **54**(2011), pp. 2602-2608.
[39] Grey, D., Long, H., and Maropoulos, P., 2005, "Effects of welding speed, energy input and heat source distribution on temperature variations in butt joint welding," ," Journal of Materials Processing Technology, **167**(2-3), pp. 393-401.
[40] Cho, J., Farson, D. F., Milewski, J. O., Hollis, K. J., 2009, "Weld pool flows during initial stages of keyhole formation in laser welding," J. Phys. D: Appl. Phys. **42**, pp. 1-11.
[41] Hu, Y., He, X., Yu, G., Ge, Z., Zheng, C., and Ning, W., 2012, "Heat and mass transfer in laser dissimilar welding of stainless steel and nickel, Applied Surface Science, **258**, pp. 5914-5922.
[42] Zhao, Y. Z., Zhao, H. Y., Lei, Y. P., and Shi, Y. W., 2007, "Theoretical study of Marangoni convection and weld penetration under influence of high oxygen content in base metal." Science and Technology of Welding & Joining, **12(**5), pp. 410-417.
[43] Incropera, F. P., DeWitt, D. P., Bergman, T. L., and Lavine, A. S., 2011, *Fundamentals of Heat and Mass Transfer*, John Wiley & Sons, Hoboken, NJ.
[44] He, J., Norris, J. T., Fuerschbach, P. W., and DebRoy, T., 2006, "Liquid metal expulsion during laswer spot welding of 304 stainless steel," J. Phys. D: Appl. Phys., **39**(3), pp. 525-534.
[45] Kumar, N., Dash, S., Tyagi, A. K., and Raj, B., 2011, "Melt pool vorticity in deep penetration laser material welding," Indian Academy of Sciences, **36**(2), pp. 251-265.

[46] Bachmann, M., Avilov, V., Gumenyuk, A., and Rethmeier, M., 2012, "Numerical simulation of full-penetration laser beam welding of thick aluminum plates with inductive support," J. Phys. D: Appl. Phys. **45**(3), 035201.
[47] Sudnik, W., Radaj, D., and Erofeew, W., 1996, "Computerized simulation of laser beam welding, modelling and verification," J. Phys. D: Appl. Phys. **29**(11), pp. 2811-2817.
[48] Nix, F. C. and MacNair, D., 1941, "The Thermal Expansion of Pure Metals: Copper, Gold, Aluminum, Nickel, and Iron," Phys. Rev., **60**(8), pp. 597-605.
[49] Austin, J. B., and Pierce, R. H. H., 1933, "The Linear Thermal Expansion and Alpha-Gamma Transformation Temperature of Pure Iron," Physics, **4**(12), pp. 409-410.
[50] Hosford, W. F., 2005, *Mechanical Behavior of Materials*, Cambridge University Press, Cambridge, UK.
[51] Roy, A. K., 2005, "Finite element analysis and life estimation of a permanent cylindrical mold with ANSYS and Coffin-Manson approach," M.S. thesis, Auburn University, Auburn, AL.

Chapter 3

[52] Ribic, B., Rai, R., and DebRoy, T., 2008, "Numerical Simulation of Heat Transfer and Fluid Flow in GTA/Laser Hybrid Welding," Science and Technology of Welding Joining, **13**, pp. 683-693.
[53] Bisen, K. B., Arenas, M., El-Kaddah, N., and Acoff, V. L., 2003, "Computation and Validation of Weld Pool Dimensions and Temperture Profiles for Gamma TiAl," Metallurgical and Material Transactions A, **34**A, pp. 2273-2279.
[54] Goldak, J., and Akhlaghi, M., 2005, *Computational Welding Mechanics*, Springer, New York, NY.
[55] Schneider, G. E., Raithby, G. D., and Yovanovich, M. M., 1978, "Finite-element Solution Procedures for Solving the Incompressible, Navier-Stokes Equations Using Equal Order Variable Interpolation," Numerical Heat Transfer, **1**, pp. 433-451.
[56] Keene, B. J., 1993, "Review of Data for the Surface Tension of Pure Metals," International Materials Reviews, **38**(4), pp. 157-192.
[57] Graebel, W. P., 2001, *Engineering Fluid Mechanics*, Taylor & Francis, New York, NY.
[58] Bejan, A., 1995, *Convection Heat Transfer*, John Wiley & Sons, Inc., New York, NY.
[59] Brillo, J. and Egry, I., 2005, "Surface tension of nickel, copper, iron and their binary alloys," J. Mater. Sci., **40**, pp. 2213-2216.
[60] Rai R., Elmer J. W., Palmer T. A., and DebRoy T., 2007, "Heat Transfer and Fluid Flow during Keyhole Mode Laaser Welding of Tantalum, Ti-6Al-4V, 304L Stainless Steel and Vanadium," J. Phys. D: Appl. Phys., **40**, pp. 5753-5766.
[61] Pan Y. and Richardson I. M., 2011, "Keyhole Behavior during Laser Welding of Zinc-coated Steel," J. Phys. D: Appl. Phys., **44**, 045502.
[62] Ion, J. C., 2005, *Laser Processing of Engineering Materials*, Elsevier Butterworth-Heinemann, Burlington, MA.

Appendix A

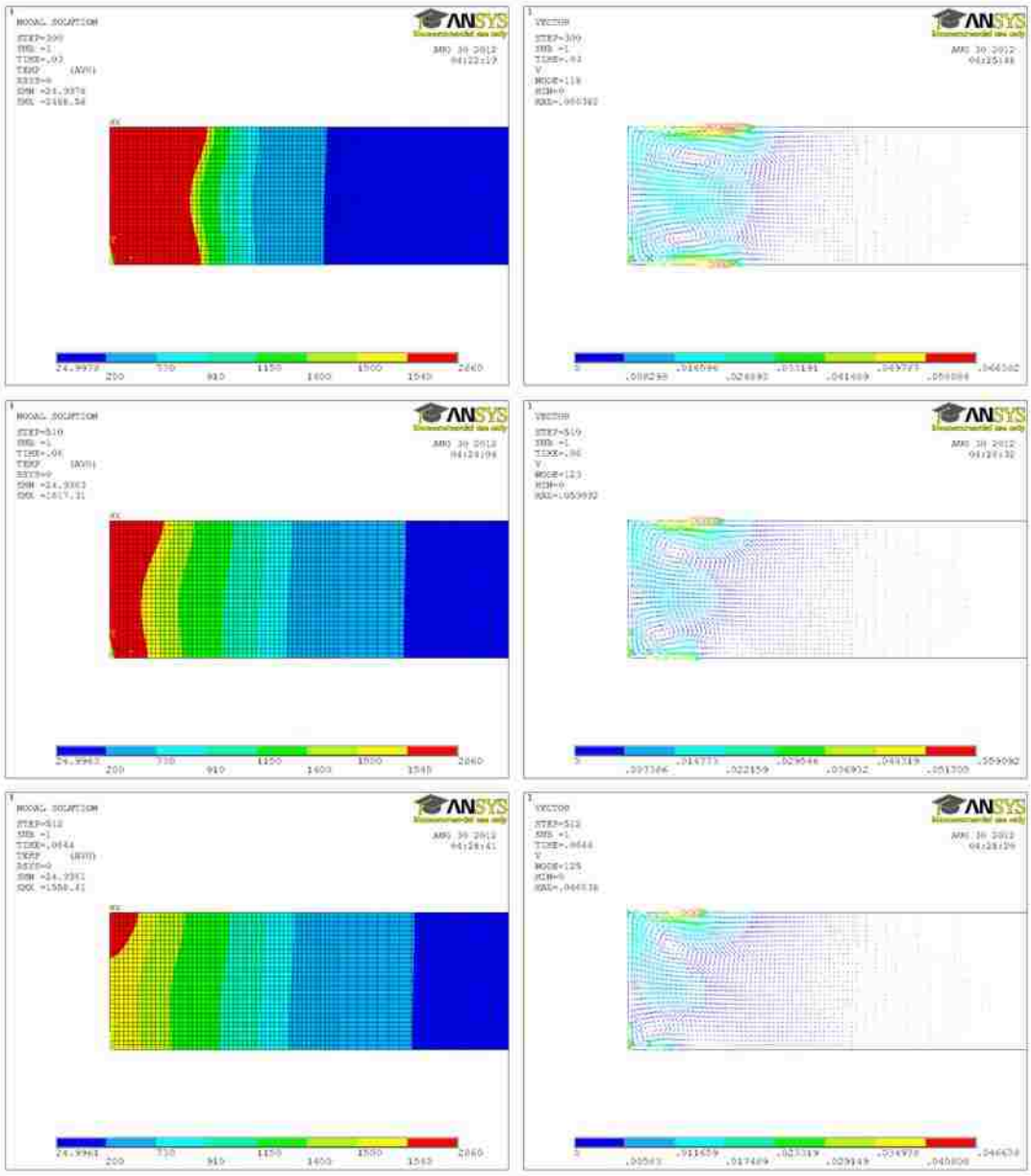

Figure A.1 Effect of heat dissipation on the melt dynamics with laser intensity of 3.58×10^{10} W/m^2 and welding velocity of 100 mm/s

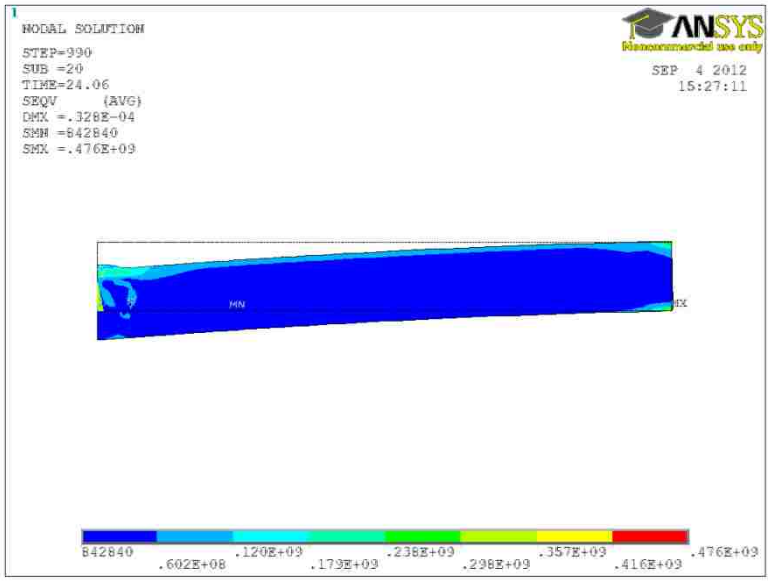

Figure A.2 Distribution of residual stresses on a plate thickness of 1.2 mm with laser intensity of 1.79×10^{10} W/m^2 and welding velocity of 100 mm/s

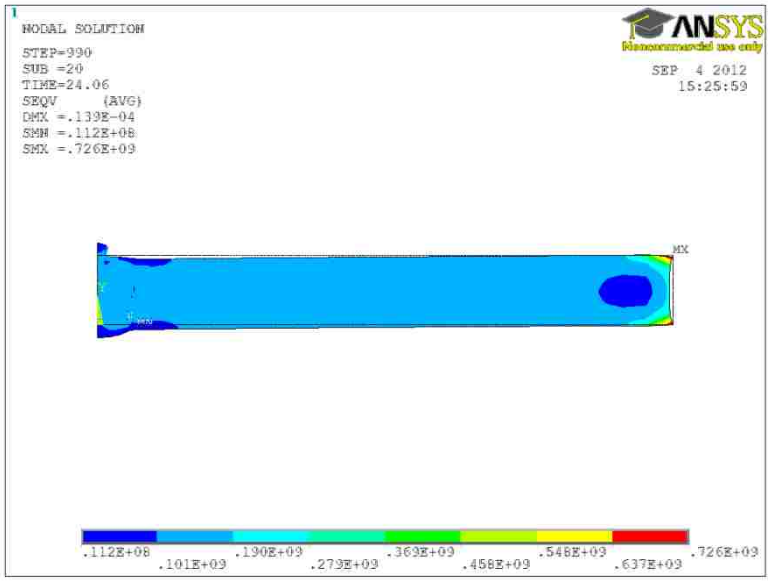

Figure A.3 Distribution of residual stresses on a plate thickness of 1.2 mm with laser intensity of 2.38×10^{10} W/m^2 and welding velocity of 100 mm/s

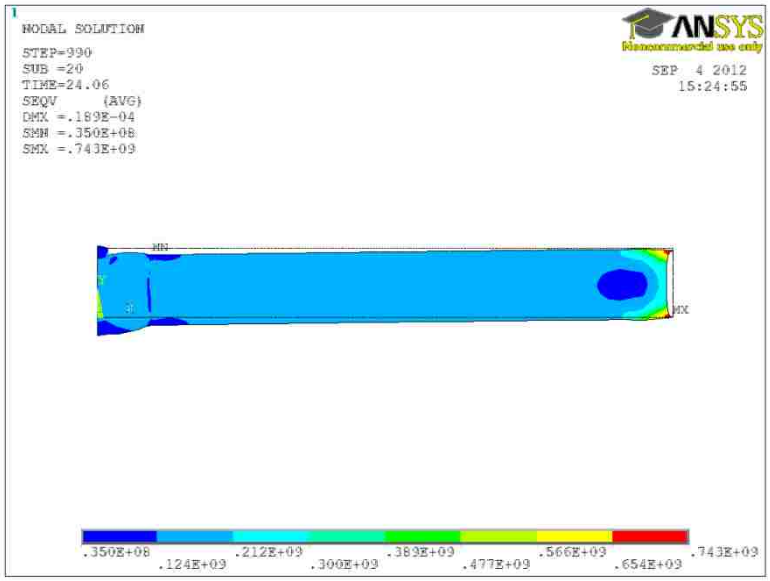

Figure A.4 Distribution of residual stresses on a plate thickness of 1.2 mm with laser intensity of 2.98×10^{10} W/m^2 and welding velocity of 100 mm/s

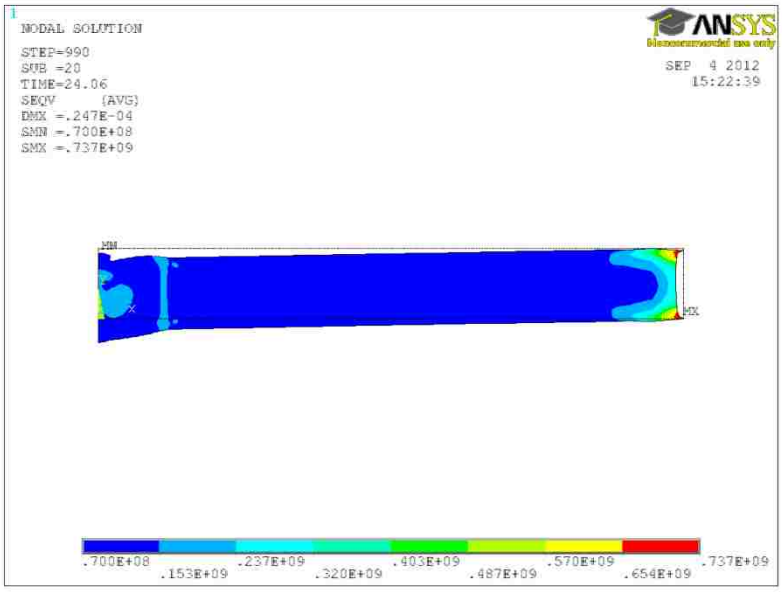

Figure A.5 Distribution of residual stresses on a plate thickness of 1.2 mm with laser intensity of 3.58×10^{10} W/m^2 and welding velocity of 100 mm/s

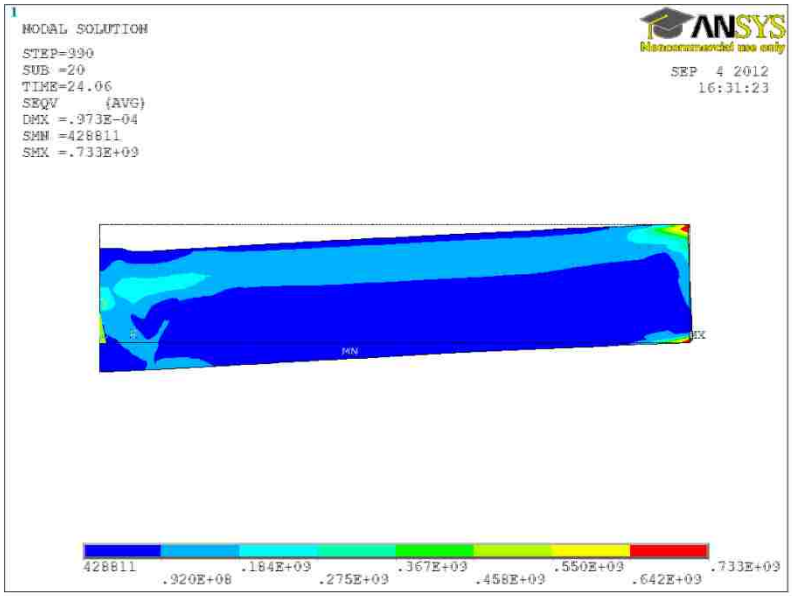

Figure A.6 Distribution of residual stresses on a plate thickness of 2.0 mm with laser intensity of 5.96×10^{10} W/m^2 and welding velocity of 100 mm/s

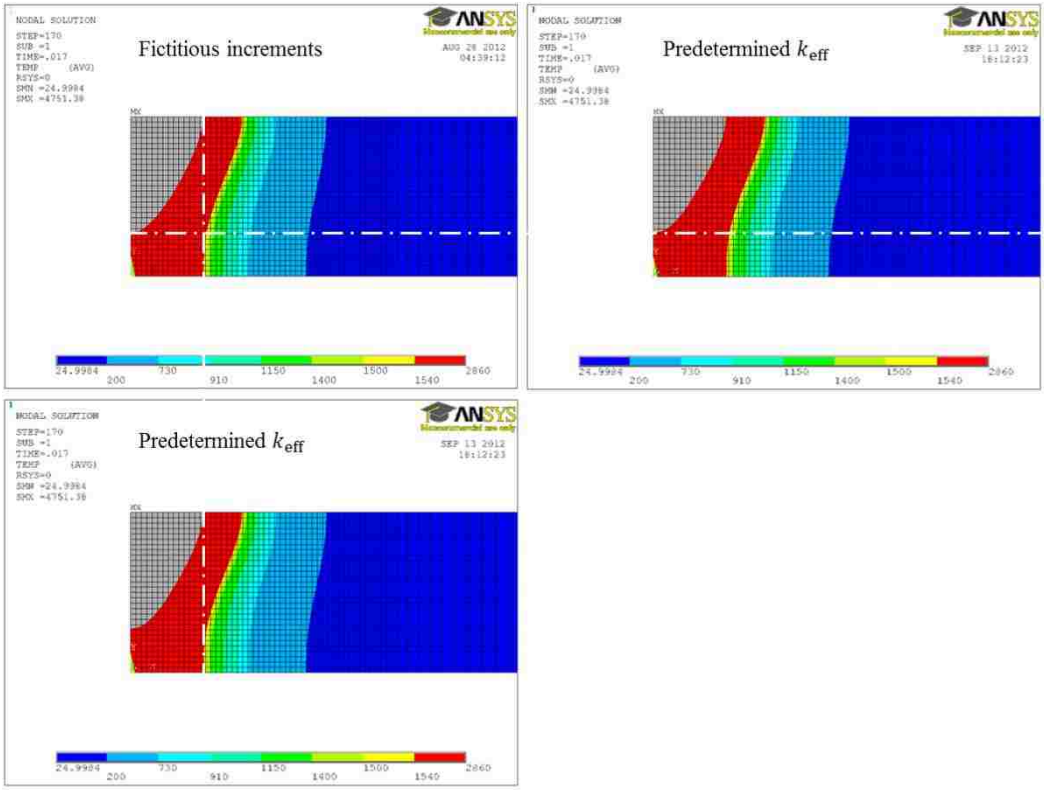

Figure A.7 Temperature distribution comparisons between two different thermal conductivity sets: measured during melt penetration with intensity of 3.58×10^{10} W/m^2 and velocity of 100 mm/s

Vita

Bon Seung Koo was born in Seoul, South Korea on April 25, 1976. He graduated from Sangmoon high school in 1995. He continued his undergraduate studies and then received a B.S. in Mechanical Engineering at Dankook University, Seoul in 2002. He started to work at Daewoo Heavy Industries and Machineries in Incheon, S. Korea for researching, developing, and manufacturing a large-scale construction vehicle since his graduation in 2002. He has been at Lehigh University studying a finite element based numerical computation of welding for a measure of welding deformation and the elevation of stresses since 2007.